UNIVERSITÀ DEGLI STUDI DI NAPOLI "FEDERICO II"

Department of Chemical, Materials and Industrial Production Engineering
(DICMAPI)

PhD in "Industrial Products and Process Engineering", XXXVI cycle.

"A MICROFLUIDIC DEVICE FOR SPERM SELECTION BASED ON DIFFERENT IN-FLOW MOTION DYNAMICS UNDER VARIABLE VISCOSITY CONDITIONS"

Coordinator
Ch.mo Prof. Andrea D'Anna

Scientific Committee
Ch.mo Prof. Filippo Causa
Maria Isabella Maremonti, Ph. D
David Dannhauser, Ph. D

Supervisor
Ch.mo Prof. Paolo Antonio Netti

Author
Luigi Fausto Canonico

November 2020 – January 2024

Index

Acknowledgment

I would like to express my deepest gratitude to my primary supervisor, *Prof. Paolo Antonio Netti*, for giving me the opportunity to join his research group. He offered me his invaluable guidance, unwavering support, and profound expertise throughout every stage of this work.

Special thanks are extended to *Prof. Filippo Causa* for his contributions and constructive criticism which have helped in enriching the depth and quality of this doctoral work.

I would like to thank *David Dannhauser* for the support he gave me during the realization of this work.

I am deeply thankful to *Maria Isabella Maremonti* for her support and enduring encouragement. Her invaluable guidance has been pivotal in my professional development, equipping me with the essential tools to navigate the intricacies of research. Her work has been essential in shaping the direction and scope of this thesis.

I would like to thank all my colleagues, and particularly *Claudia De Clemente*, for her support and for sharing all the various stages of this doctoral journey together.

My family has played a crucial role in standing by me, providing unwavering support, and believing in me throughout the completion of this work. Without their support, none of this would have been possible, and I am immensely grateful to them.

Finally, I would like to dedicate this work to *Riccardo*, who has been my anchor and constant source of support over the years.

Abstract

For decades, male fertility diagnosis has relied on conventional manual sperm analysis mainly based on count, motility, and morphology. Despite exhibiting 'normal' sperm features, a significant number of men experience infertility, emphasizing the limitations of current diagnostic methods and necessitating a transition to innovative approaches. In response to this, some laboratories have adopted computer-assisted sperm analysis (CASA) alongside manual techniques. CASA provides the evaluation of different sperm features, such as motility and morphology, overcoming the subjectivity associated with manual analysis, but still providing discrepancies among different systems. However, routine semen analysis often fails in accurately assessing the fertilizing potential of sperm. Indeed, such analysis approaches do not account for the complex environment of the female reproductive tract (FRT), where sperm encounter various morpho-physical barriers that they need to overcome to achieve the fertilization of the oocyte. Nowadays, the current gold standard in assisted reproductive technology (ART) includes intrauterine insemination, in vitro fertilization, and intracytoplasmic sperm injection. Despite their prevalence, these techniques yield only a modest 25-30% success rate. Indeed, they mainly rely on common sperm selection approaches comprising multiple centrifugation steps which poses damages on the cells and select them considering motility only. This gap highlights the need for the development of innovative methods.

Our study introduces a novel approach that replicates a female-like environment to analyze and select sperm based on different in-flow motion dynamics while varying the viscosity of the fluid. We started from static and then moved to dynamic conditions by utilizing glass microscope observation chambers with varying depths and a microfluidic device. Cryopreserved bovine sperm were employed as a model for this study. Our objective was to comprehensively assess sperm behavior by comparing static and dynamic measurements across different fluid viscosities, emphasizing the importance of considering both conditions for a detailed diagnosis of sperm health. Cervical mucus viscosities were mimicked using biocompatible polymer solutions, while an in-house fabricated microfluidic device allowed us to assess sperm response to fluid-flow and rheology, particularly focusing on their ability to re-orient counter-flow, i.e. rheotaxis. Given the complex roto-translational motion of sperm, which results in a 3D motility pattern, our study investigated their rolling behavior and how fluid-flow and viscosity influence it. We proposed a selection mechanism based on distinct motion patterns and fluid-flow achieving a clear separation of sperm in highly and low motile classes by means of a more physiological approach. This separation allowed the extraction of sperm with higher motility and progressivity, generally associated with a positive fertilization outcome. A notable increase of sperm velocity in deeper chambers was observed, underscoring the influence of geometric confinement, and viscosity emerged as a crucial factor, affecting sperm velocity and modifying 3D motion. It induces a planarization of sperm 3D motion patterns suggesting a distinction between normal and altered motile sperm which allows an improved selection mechanism in contrast to conventional techniques. In addition to these findings, we propose the identification of additional parameters that could potentially enhance diagnostic precision and improve diagnostic outcomes. This comprehensive research provides additional insights into the intricate dynamics

influencing sperm motility within the FRT, offering a versatile and cost-effective approach to enhance our understanding of male fertility. In summary, the suggested microfluidic selection mechanism is versatile, since within a single device, it enables the observation of various aspects of motility and their physiological interaction. This approach addresses key aspects of fertility diagnostics and treatment strategies for individuals experiencing reproductive challenges.

1. Introduction.

1.1. Male infertility rates.

Clinical infertility is defined as the inability of couples to reach pregnancy after 12 months of trying. It is increasingly becoming a prominent global health concern, impacting over 50 million couples across the globe [1,2]. The escalating rates of infertility emphasize the pressing need for more accessible and affordable diagnosis and treatment solutions. Notably, many regions, such as the USA, Canada, and the European Union, are experiencing total fertility rates below the 2.1 threshold necessary to maintain population stability. Statistics reveal that approximately 30% of infertility cases stem from male-related factors (Figure 1) [3]. Moreover, there is a concerning trend indicating a decline in semen quality among men. Male infertility can be caused by several issues associated to male reproductive system, such as testicular disfunction and anatomical defects, and external factors such as environment and lifestyle [4,5,6]. Other physical factors, including testicular torsion and infections of the genital tract, such as Gonorrhea and Chlamydia can also obstruct the epididymis, i.e. the duct designed for the storage, maturation and transport of sperm [7]. Determining precise infertility rates worldwide poses significant challenges. Firstly, many population surveys focus on couples or specifically women attempting conception, excluding men with potential infertility issues, and thereby introducing biases into the data. Secondly, the global disparity in how male and female infertility are reported is evident, often owing to cultural believes frequently attributing infertility to women. Further complicating matters is the lack of a universally accepted definition for male infertility, which is strongly influenced by the subjectivity of clinics and of the methods employed to diagnose it [3,8].

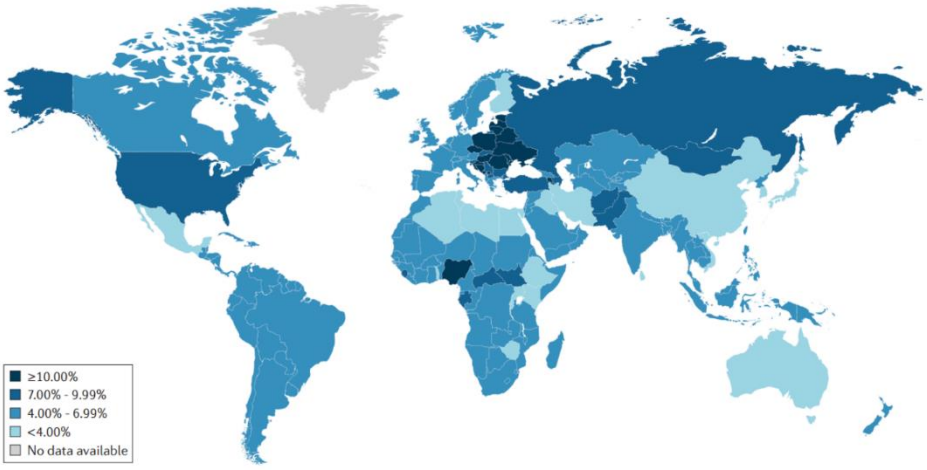

Figure 1. Male infertility rates worldwide. A global map illustrating the incidence of male factor infertility. This incidence is derived from the overall infertility rate multiplied by the proportion attributable specifically to male factors. The different colors employed indicate different percentages of male infertility in each country. Reproduced from [1].

1.2. Sperm structure and locomotion.

Given the diverse factors contributing to male infertility and its increasing global significance, there is a pressing need for politics, scientific community, and society to increase attention and enhance its diagnosis [1]. A foundational understanding of the intricate mechanics and motion patterns of sperm is crucial. Capturing their intricate movement and interactions within the female reproductive tract (FRT) not only emphasize the importance of accurate diagnosis but also ensures effective and targeted interventions for fertility challenges. The role of a sperm is to fertilize the oocyte and transfer its genetic material for the development of the embryo. Sperm is the most motile cell in the organism, and it must swim thousands of its body lengths and overcome several barriers and obstacles to achieve fertilization [9]. Prior to analyze the sperm motion, it is essential to understand how a sperm is composed from a structural point of view. In general, a mammalian sperm is constituted by a head, containing the nucleus, and a tail which instead contains all the structural components essential for motility. Sperm head function is to deliver the haploid, i.e. a single complete set of chromosomes, to the oocyte while the one of the flagellum (i.e. the tail) is to provide motility. Inside the head, we find the nucleus and, in the apical part, the so-called acrosome which is a cap like structure present in most mammalian species (Figure 2A). The acrosome, which comes from the Golgi apparatus, contains specific enzymes and membrane receptors crucial for traversing the cumulus cell barrier and disintegrating the surrounding zona pellucida of the oocyte. Sperm head shape changes among species. For example, a human sperm head shows an oval-like shape of 3 - 5μm in length and 1.5 – 3μm in width, while a bovine sperm head has a paddle-like shape of 9 – 10μm long, 4 – 5μm wide, and 1μm thick [10,11,12]. The flagellum, on the other hand, can be divided into four portions: the connecting piece, connecting the head with the tail, the mid piece, containing the mitochondria for energy production, the principal, and the end piece (Figure 2A). The principal piece of the flagellum is constituted by the axoneme surrounded by the fibrous sheath and containing the outer dense fibers (ODF) which ensure elasticity and structural integrity, suppressing buckling in high-viscosity fluids. The axoneme is composed by a central microtubules pair (CP) surrounded by nine microtubule doublets (MTDs) each one composed of an A and a B subunit (Figure 2B). The former is constituted by two dynein arms, the outer (ODA) and inner ones (IDA) which are ATPase complexes which translate chemical energy (ATP) into kinetic energy allowing adjacent microtubule doublets to slide relative to one another, leading to the axonemal bending. The flagellum of mammalian sperm has varying dimensions. In details, human flagella are about 50μm long, while bovines have a flagellum of about 60μm in length [10,13,14,15].

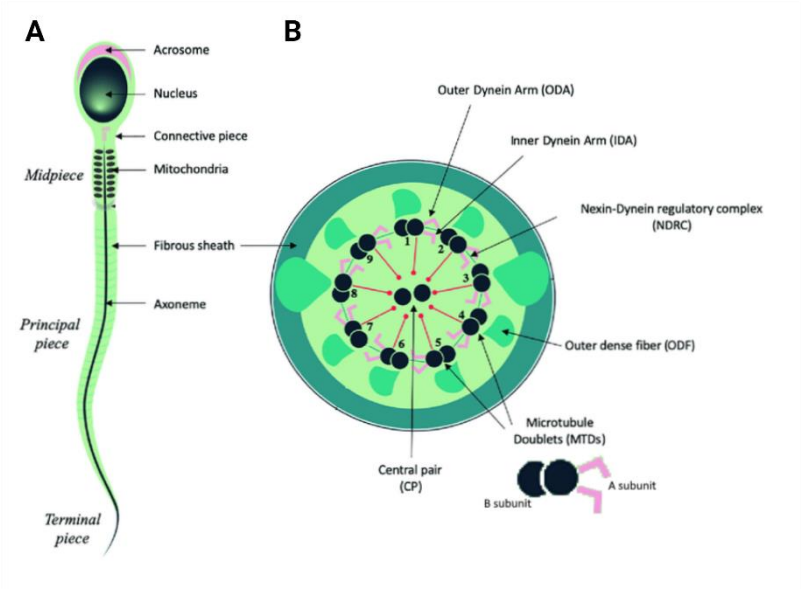

Figure 2. Mammalian sperm structure. A) Mammalian sperm head and tail structure, showing head components and flagellum sections. **B)** Structure of the internal part of the axoneme composing the whole length of the sperm flagellum. Reproduced from [11].

When placed inside a fluid, sperm can be seen as "pusher" micro-swimmers which push fluid away from the front and back and pull it from the sides. They can be considered as low inertia "machines", owing to their low dimensions, leading to a very small Reynolds's number, and force and torque free during their movement [16,17,18]. Thus, the swimming hydrodynamics of sperm can be studied by using the Stokes's equations (eqn.1 and 2).

$$-\nabla P + \eta \nabla^2 v = 0 \tag{1}$$

$$\nabla \cdot v = 0 \tag{2}$$

where P is the pressure, η is the dynamic viscosity of the fluid and v is the fluid velocity. Therefore, sperm, considered as slender and anisotropic bodies, exploit the drag induced by the fluid to move and propel themselves using the so-called "drag thrust" [1,18]. Each segment of a filament immersed in a viscous fluid can be considered as straight and moving with velocity u having an angle θ to the local tangent. This velocity can be decomposed in a tangent ($u_{\parallel}$) and a perpendicular component ($u_{\perp}$) both determining a viscous drag force ($f_{\parallel}$ and $f_{\perp}$ respectively), defined in the following equations.

$$f_{\parallel} = -\xi_{\parallel} \cdot u_{\parallel} = -\xi_{\parallel} \cdot u \cos\theta \tag{3}$$

$$f_{\perp} = -\xi_{\perp} \cdot u_{\perp} = -\xi_{\perp} \cdot u \sin\theta \tag{4}$$

where $\xi_{\parallel}$ and $\xi_{\perp}$ are the tangent and perpendicular drag coefficients (Figure 3A). As a matter of fact, the drag experienced by the segment in the perpendicular direction will be always higher than in the tangential one

($\xi_\perp > \xi_\parallel$) leading to an unbalance of drag forces which determines a net propulsive force *(f_{prop})* in the direction perpendicular to the velocity u, defined in equation (5) (Figure 3A).

$$f_{prop} = (\xi_\parallel - \xi_\perp) u \sin\theta \cos\theta \, e_x \tag{5}$$

It is important to note a fundamental principle here, known as the Scallop Theorem [19]. This theorem states that organisms with a periodic shape (like a scallop), when moving with a reciprocal motion, i.e. for every action in one direction, there is an equal and opposite reaction in the opposite direction, cannot generate a net forward motion in a purely non-viscous fluid, irrespective of how they deform their shape. This is because organisms with a periodic shape and reciprocal movement produce forces in two opposite directions within a single motion cycle. As a result, the organism does not make net progress in any direction; it essentially stays in place. Differently from symmetric organisms, sperm have a distinct shape that is not perfectly symmetrical. Their elongated, tapered form allows them to interact differently with the surrounding fluid as compared to a perfectly symmetrical object. This anisotropic shape creates asymmetries in the drag forces experienced by the sperm during its motion. Moreover, the flagellum of the sperm exhibits a complex, three-dimensional (3D) motion pattern rather than a simple reciprocal motion which interacts with the surrounding fluid in a manner that can produce a net forward force. More recent investigations allowed the reconstruction of several types of 3D motion of sperm by employing holographic imaging techniques, leading to the reconstruction of four main trajectories such as: typical, helical, hyper-activated and hyper-helical (Figure 3B) [20,21].

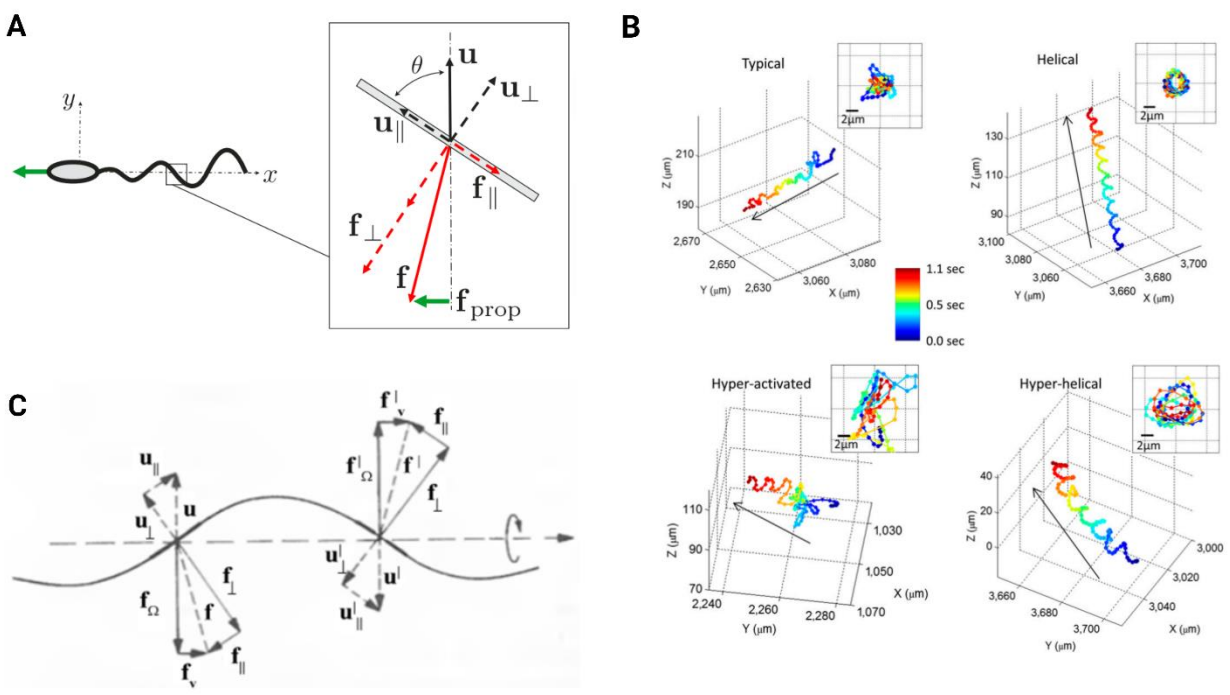

Figure 3. Sperm locomotion. A) Physics of drag-based thrust theory showing the generation of the propulsive force *(f_{prop})* for sperm locomotion. Reproduced from [1,22]. **B)** Main human swimming patterns: Typical Patter, Helical Pattern, Hyperactivated Pattern, Hyper-helical Pattern. The color of each point on the trajectory indicates its position in time, as shown in the accompanying color bar, while the inset shows a front view of the sperm trajectory. Arrows within each panel indicate the direction of the sperm forward motion. Reproduced from [20]. **C)** Physics of sperm body rotation

derived from local drag thrust theory showing the decomposition of the drag forces on the axis of rotation of the tail. Reproduced from [23].

The typical motion pattern is the most prevalent one and consists in progressive motion with small lateral displacement of the head. In the second set of observed sperm motion patterns, helical paths were identified. These paths depict the sperm head rotating steadily around its axis, creating a distinct helix. Moving into the third category, a minority of sperm, displayed hyperactivated 3D movements which are very different with respect to the first two patterns, showing faster instantaneous speeds, but reduced progressivity. Lastly hyper-helical motion pattern was found very rarely, and they are a combination of hyperactivation and regular helical motions. The flagellar motion of human sperm is notably intricate and non-planar, characterized by an approximately symmetrical projected shape that gives rise to curvilinear trajectories. It has been observed that this unique movement is not merely side-to-side and due to the pronounced asymmetrical dynamics of the beat, the entire sperm head undergoes a rolling motion. This rolling effect causes its plane to rotate continuously, resulting in a distinctive and visually captivating, twisted ribbon-like path [24]. Accordingly, in response to the helical transmission of the flagellar bending, sperm body undergoes a complete rotation. As a matter of fact, the helical rotation of the tail induces an otherwise unbalanced torque over the sperm body [22]. Indeed, being the sperm a force and torque free organism, it must respond to this flagellar rotation with an equal and opposite rotation of the whole body. To understand sperm rotation, we can consider two segments of the flagellum being half a turn out of phase, each one experiencing the tangential and perpendicular drag forces, previously described (Figure 3C). The first segment moves upwards while the second moves downwards. Both forces, can, in turn, be decomposed in two components on the horizontal axis of the rotating helix denoted as f_{v} and f_{Ω} for the first segment and $f_{\mathrm{v}}{}'$ and $f_{\Omega}{}'$ for the second segment. f_{v} and $f_{\mathrm{v}}{}'$ are parallel to the axis while f_{Ω} and $f_{\Omega}{}'$ are perpendicular. f_{v} and $f_{\mathrm{v}}{}'$ act in the same direction causing propulsion while f_{Ω} and $f_{\Omega}{}'$ act in opposite directions determining the torque which will be equal and opposite to the one of the tail [23]. The rotational motion of mammalian sperm in mammalian, crucial for progressive motility, has been observed to occur through a complete $360°$ revolution, as opposed to a simple flipping back and forth, for both human and bull. A recent study introduced an innovative methodology based on the application of optical tweezers to assess both the chirality and rotational frequency of sperm. By analyzing the rotational direction of the sperm head projection, they found that human sperm exhibit a right-hand longitudinal rolling pattern which translates in a counterclockwise (CCW) head rotation if observed head-on. These results are in good agreement with other literature findings showing that, for both human and bull sperm, the head rolling direction is CCW, if seen from head to tail [25,26,27,28,29].

1.3. Female reproductive tract (FRT) influence.

Knowing the physics behind sperm locomotion is essential to understand the interaction between this complex hydrodynamics with the micro-environment in which sperm come into contact during their journey. In fact, from the moment of deposition, in the vaginal tract, to the site of fertilization, sperm encounter a series of chemical and morpho-physical barriers which they must overcome to achieve fertilization of the oocyte (Figure 4). During its journey a sperm moves in a 3D complex environment and exploits different types of motion patterns adapting itself to the stimuli and obstacles offered by the FRT.

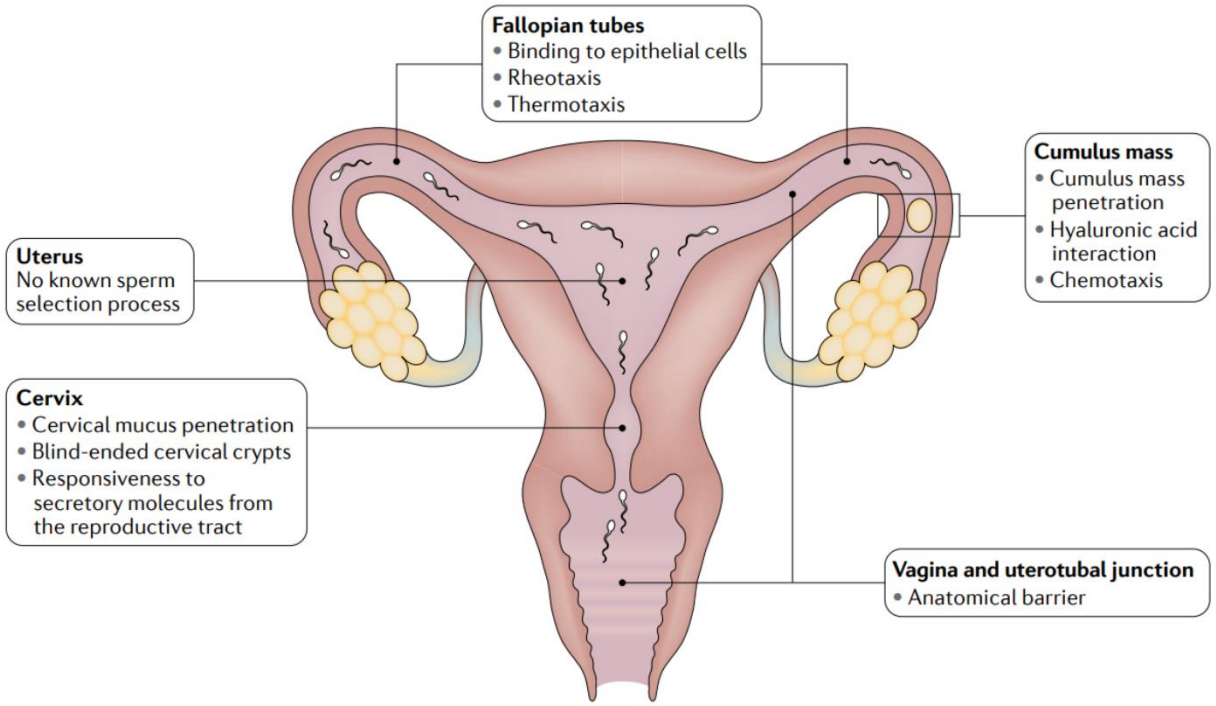

Figure 4. Female reproductive tract (FRT) influence on sperm in vivo. Sperm are deposited in the vagina during intercourse. It represents an anatomical barrier which firstly select sperm prior to their entry into the viscoelastic environment of the cervix. Then they pass through the uterus and the utero-tubal junction (UTj) to enter the fallopian tubes where they experience rheotaxis (fluid-flow), chemotaxis and thermotaxis. At the end they reach the cumulus mass and fertilize the oocyte. Reproduced from [30].

In humans and other mammals, such as bovine, sperm are deposited in the vagina which represent an anatomical barrier characterized by an acidic pH (Figure 4). Vaginal pH ranges from 4 to 4.9 in humans while it is less acidic for other mammals, such as cows, where it goes from 6 to 6.8, since it has been observed that more acidic pHs immobilize bull sperm. Upon contact with the vaginal micro-environment, semen quickly transforms into a loose gel post-coitus. This gel, primarily composed of proteins like semenogelin I and II, originates mainly from the alkaline seminal vesicle secretion (pH~8) and its role is to shield sperm from the acidic vaginal environment. Within about 30min from deposition, the coagulum is degraded by prostate-specific antigen (PSA) so that sperm are free to proceed their journey towards the cervical canal [31,32,33,34].

Here they encounter a micro-environment characterized by a viscoelastic mucus, having a neutral pH and mainly composed of glycoproteins, i.e. mucins, whose structure changes during the menstrual cycle leading to a variation of the rheological properties of the fluid. It has been found that sperm penetrability is maximum during the ovulatory phase when the mucus is more water-like to facilitate fecundation. On the other hand, the passage of sperm is strongly obstructed and/or limited during both the Follicular and Luteal phases, owing to the increased viscoelastic properties of the mucus. It has been measured that the cervical mucus viscosity varies from $0.1\ Pa \cdot s$ to $1\ Pa \cdot s$. The main role of cervical mucus is to block all the sperm having reduced motility and abnormal morphology. Moreover, the arrangement of the mucin composing the cervical mucus offers preferential pathways for the most progressive sperm, impeding the passage of the defective and low motile ones [35,36,37,38,39]. Viscous and viscoelastic solutions of polymers, such as long-chain polyacrylamide (LC-PAM), polyvinylpyrrolidone (PVP), hyaluronic acid (HA) and methylcellulose (MC), have been employed to replicate cervical mucus viscosities and observe their influence on both humans and bovine sperm motility [40,41,42,43]. They observed, for both species, that swimming velocity decreases as fluid viscosity rises, determining a reduction in sperm motility along with an increase in progressivity. Sperm can adapt their motion behavior to environmental conditions, displaying patterns suited to their surroundings. Recent observations reveal that the viscoelasticity of cervical mucus induces sperm association, facilitating collective swimming and that this interaction aids in swimming against viscoelastic fluid flows [41,44,45]. Within the cervix, sperm are also guided towards the uterus because of the interaction with the epithelial tissue lining it. Indeed, the mammalian cervical canal is composed by longitudinally lined microgrooves, which in cows have been measured to be 10 – 20μm wide, whose role is to offer preferential pathways for sperm. Indeed, it has been observed that, due to their low dimension, microgrooves force them to move in a specific direction improving their progressivity with respect to flat surfaces [46]. Once being selected within the cervix, sperm proceed into the uterus, which, given its small size (a few cm), could be crossed in less than 10min. The movement of sperm within the uterus is likely enhanced by rhythmic contractions of the myometrium near the ovaries. Within humans, these contractions might help pull the sperm along with the watery mucus at midcycle (ovulatory phase) from the cervix deeper into the uterus [47,48]. Sperm tend to accumulate near the boundaries of the uterus tissue following them and being guided towards the utero-tubal junction (UTj). This represent an anatomical barrier which could be overcome only by highly progressive sperm leaving behind those with abnormal morphology or altered motility patterns [49]. The oviduct, also known as Fallopian tubes, is a slender structure adjacent to the ovary and measures approximately 0.4 – 0.5mm in diameter and 18 - 30mm in length. Going from the uterus towards the ovary, the oviduct is lined with an intricate longitudinal folded epithelium whose structure gradually increases in complexity and decreases in features dimensions. In addition, the lumen within the fallopian tube exhibits varying curvatures, ranging from approximately 20μm to over 150μm [50,51]. The selection and guiding mechanisms found within this complex structured portion of the FRT can be classified in long-range and short-range mechanisms (Figure 4). Regarding the former, the most efficient one is positive rheotaxis (PR) which consists in the ability of sperm to reorient against a fluid-flow and swim counter it. Indeed, it has been observed that within the FRT, and more evidently inside the oviduct, there is a

gentle fluid-flow whose role is to guide the highly motile and progressive sperm towards the oocyte and to filter those which have, instead, impaired motility or abnormal morphology [52,53]. The latter, in fact, are not able to withstand the flow and they are washed away downstream, preventing less competent sperm from reaching the fertilization site. This observation has inspired various scientific studies, both experimental and modelling, to investigate the phenomenon of rheotaxis in mammals [54,55,56,57,58]. The short-range selection and guiding mechanisms of sperm are the so-called chemotaxis and thermotaxis which consists in the swimming against a chemical and a temperature gradient respectively [30]. In addition to these mechanisms, an important interaction which occurs in the oviduct is the adhesion of sperm to the epithelium creating the so-called sperm reservoirs. In these reservoirs sperm are preserved and sustained by the molecular interaction with the epithelial cells. When ovulation occurs, sperm capacitate and hyperactivate and are able to detach from the epithelium and continue their journey towards the oocyte. Capacitation and hyperactivation are phenomena which sperm undergo prior to fertilization to be fully competent to achieve pregnancy. Capacitation consists in a series of metabolic and physiological changes such as: increase in membrane fluidity, lateral movement of cholesterol to the apical region of the sperm head, and cholesterol efflux from the sperm plasma membrane to the extracellular environment, leading to the acrosomal reaction and change in the swimming pattern. Indeed, hyperactivated motion pattern is much different than the typical one, consisting in lower progressivity and increased lateral head displacement [20,59,60].

1.4. Altered sperm motility patterns.

In our earlier discussion about the influence of the FRT, we highlighted the intricate challenges sperm face due to the diverse rheological, flow, and morphological conditions they encounter. They primarily employ 3D motion patterns (Figure 3B), but, to overcome these morpho-physical obstacles, they adopt alterative motion patterns (Figure 5).

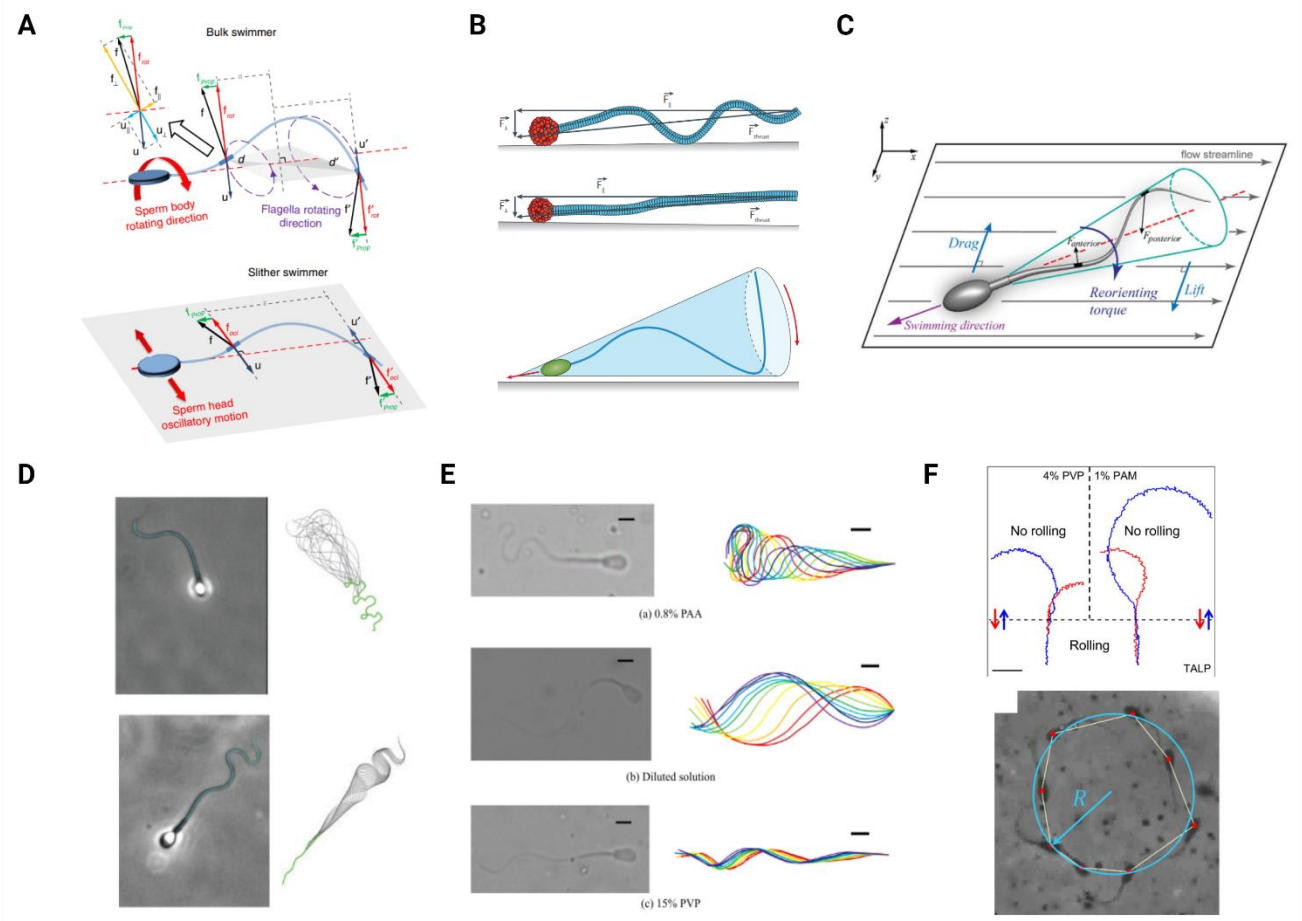

Figure 5. Alternative motion patterns of sperm due to FRT interaction. A) Dynamics of bulk and slither swimmers. (top) Bulk swimmer dynamics showing the force balance on the sperm flagellum describing the 3D motion composed by a translational *(f_{prop})* and rotational *(f_{rot})* components which translate in a complete rotation of the whole body in the opposite direction of the tail. (bottom) Slither swimmer dynamics showing the force balance on the sperm flagellum describing a 2D motion composed by a translational *(f_{prop})* and oscillating perpendicular *(f_{oci})* components leading to a surface aligned motion without head rotation. Reproduced from [9]. **B)** Mechanisms of sperm interaction with solid boundaries showing surface aligning motion leading to wall accumulation and boundary following behavior. The conical envelope od the flagellar wave is aligned with the surface orienting the time-averaged thrust vector towards it. Reproduced from [1]. **C)** Interaction of sperm conical envelope with fluid streamlines leading to sperm reorientation in the opposite direction. The lift and drag force produced give rise to a reorienting torque acting on the cell body. Reproduced from [61]. **D)** Influence of fluid viscosity on sperm head trajectory (highlighted in green) and flagellar beating. (top) Human sperm swimming in a low viscosity medium showing large head oscillation and very dynamic flagellar motion. (bottom) Human

sperm swimming in a high viscosity medium showing reduced lateral head oscillation and flagellum with sinusoidal shape. Reproduced from [40]. **E)** Influence of fluid viscosity/viscoelasticity on bovine sperm flagellar shape. (middle) Diluted solution. (top) Viscoelastic solutions. (bottom) Newtonian (high viscosity) solution. Reproduced from [45]. **F)** Influence of fluid viscosity on bovine sperm motion pattern. 3D progressive motion is observed in dilute solutions while planar circling motion is observed in viscos/viscoelastic solutions. Reproduced from [62].

Indeed, it has been found that both human and bull sperm, imaged in bulk liquid (away from the surface) and near the walls (within 1mm from the surface), showed two distinct motion patterns, respectively: bulk and slithering swimming (Figure 5A) [9]. Here they provided a schematic representation of the drag-based propulsion mechanism for sperm moving in bulk fluid compared to the one of the surface aligned ones. They found a distinct locomotion mechanism for "slither swimmers" (Figure 5A). In this scenario, the flagellar oscillation is constrained to two dimensions, specifically within the plane defined by the surface. Indeed, proximity to the surface intensifies both the tangent and normal drag coefficients, leading to an enhancement in propulsive forces and friction. Lateral drag forces intensify, simultaneously diminishing the sideways motion of the flagellar wave, leading to a change in sperm motion dynamics from 3D to a more surface aligned, 2D pattern. Being hindered by the presence of the wall, sperm exploit an oscillatory movement lacking the conventional 3D body rotation observed in bulk swimmers. This type of movement could explain the adaptation of sperm when they navigate the narrow spaces within the FRT, such as the microgrooves of the cervical canal and the folded epithelium of the oviduct [50,63]. Accumulation at the boundaries has been explained by some modelling and simulation studies in which it was observed that, near a boundary, the interaction between the conical shape of the flagellar envelope and the surface aligns the side of the tail cone with the surface owing to the inclination of the averaged thrust vector towards the wall (Figure 5B). This is due to the unbalance of hydrodynamic flow influenced by the wall creating a rotational torque which tends to align sperm in the direction parallel to the surface, leading to wall accumulation [22,64]. The interaction of the flagellum conical envelope can be observed also with fluid-flow, explaining the previously introduced PR (Figure 5C). The most common explanation for PR found nowadays is that it comes from a hydrodynamic, passive interaction between the rotating tail and the applied fluid-flow. In details, since tail beating can be approximated by a conical helix, when sperm encounter a fluid-flow, the posterior portion of the flagellum experiences a stronger drag force with respect to the anterior one resulting in a net lift force perpendicular to the flow direction. The latter is then counterbalanced by the viscous drag generating a torque which rotates the sperm body and reorients it against the flow (Figure 5C). Indeed, it has been found that no molecular mechanism is involved in this process and that it does not require transmembrane Ca^{2+} signaling. Moreover, it has been demonstrated that it exists a range of flow velocities useful to achieve PR in vitro which, for human sperm, ranges from 22μm/s to 102μm/s, while for bovines, it ranges from 27μm/s to 110μm/s. Below these ranges sperm are not able to exploit their natural rheotactic behavior because the propulsive force produced by the sperm flagellum is strong enough to overcome the flow-induced drag for upstream migration. Therefore, there is no generation of a reorienting torque over the sperm body to align it counter-flow [46,55,61,65,66].

Another mechanism of sperm motility adaptation relates to the influence they experience due to the viscoelastic environment within the FRT. The two main effects that increased viscosity has on sperm movement relate to the flattening of their trajectory in terms of lateral head displacement and a modification in their motion pattern (Figure 5D and E). This means that these environmental fluids can alter the way sperm move, affecting their ability to reach and fertilize the oocyte. The viscosity of the surrounding fluid creates a drag essential for their propulsion. When this viscosity is heightened, it amplifies the resistance they encounter and consequently, sperm navigate in a context where their movement faces increased fluid friction, leading to an alteration in their natural 3D motion patterns. In addition, it induced also a reduction of velocity and increase in progressivity (Figure 5D bottom) with respect to a watery medium (Figure 5D top). In addition, viscosity emerges as a fundamental factor shaping the dynamics of flagellar movement. When immersed in a low-viscosity medium, sperm exhibit a more dynamic flagellar motion, characterized by faster wave speeds. However, as the surrounding fluid viscosity intensifies, the fluid resistance impedes the flagellum flexibility and the average progression per beat decreases. Similar results were found also for bovine when comparing sperm motility in Newtonian fluids to shear-thinning viscoelastic ones [40,45]. The change in the motility pattern and in flagellar beating observed here is also related to a change in the rotational component of sperm movement. Indeed, the increased viscosity/viscoelasticity of the medium seems to strongly affect sperm head rolling. In conditions of low fluid viscosity, where fluid drag is low, sperm were found to roll around their longitudinal axis in a CCW direction showing a rolling frequency of $\sim 10 \pm 4 Hz$ and $\sim 9 \pm 5 Hz$ for bovine and human, respectively [25]. More recent works focused on the effect of increased viscosity on sperm rolling percentage and rolling frequency. It has been observed that the percentage of rolling sperm strongly reduces as the viscosity increases and that, among those that continue to roll, their rolling frequency becomes notably reduced. They also observed that the fraction of sperm which do not perform rolling motion is not able to describe a complete 3D motion and indeed they move oscillating in 2D as the slither swimming mode. This 2D motion results in the description of circular trajectories lacking progressivity in a specific direction (Figure 5F). As fluid viscosity rises, the resistance on the sperm body is higher than the force generated by the flagellum 3D structure. Consequently, it is believed that certain less motile or defective sperm are unable to overcome the increased fluid resistance and rotate properly, leading to a rise in the proportion of not progressive sperm. It is important to note that no rolling sperm may be defective [42,62,67,68]. When placed in the cervical mucus of the FRT, they could get trapped in its matrix and filtered out, unlike their highly motile and progressive counterparts.

1.5. Sperm Analysis.

1.5.1. Manual Analysis.

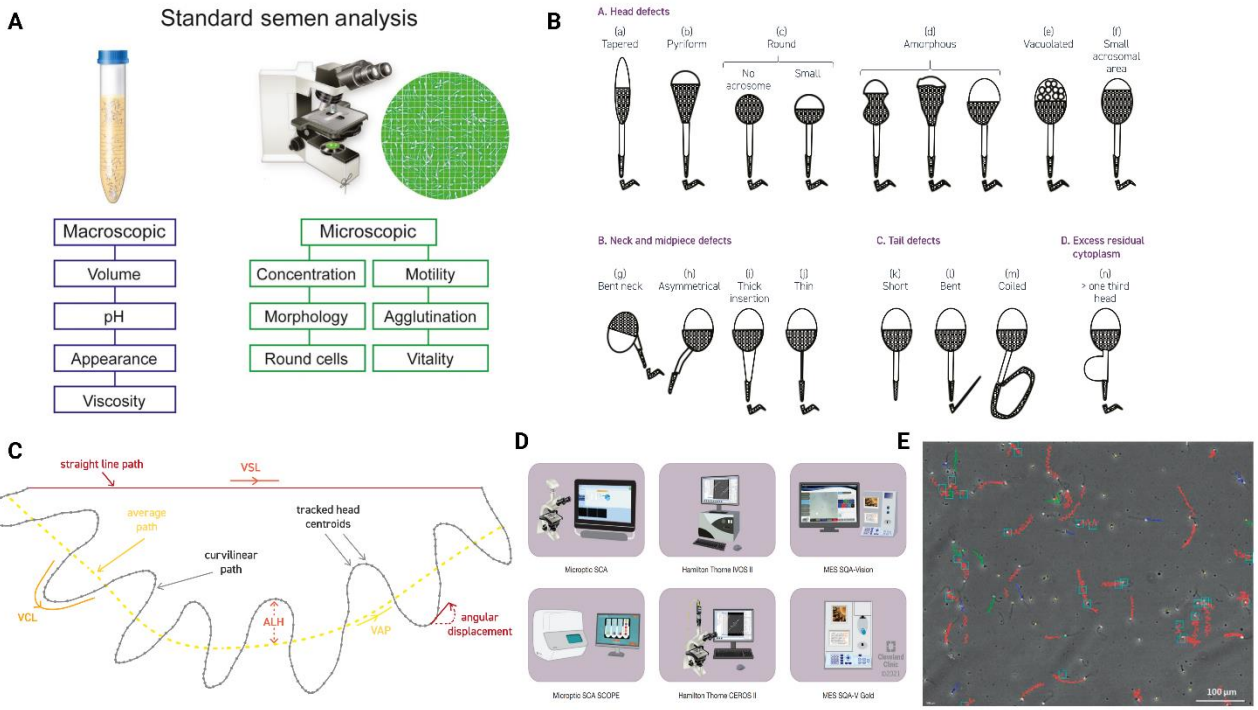

Figure 6. Conventional sperm analysis. A) Standard semen analysis: Macroscopic and Microscopic evaluation. Reproduced from [69]. **B)** WHO standard for semen evaluation: classification of head and tail morphological defects. Reproduced from [70]. **C)** Schamatic of a sperm trajexctory with the main motility parameters. Reproduced from [70]. **D)** Different types of commercially avalable CASA systems. Reproduced from [71]. **E)** Typical output of motility analysis of a CASA system showing the recontructed trajectories on top of a real image. The trajectories are color coded based on their motility sub-classes. Reproduced from [72].

Clinical diagnosis of male infertility is carried out, nowadays, by considering three major aspect which are, sperm count, morphology and motility. The assessment of semen analysis relies on reference values provided by the World Health Organization (WHO) available in the laboratory manual for the examination and processing of human semen. The analysis consists in the evaluation of both macroscopic and microscopic semen features such as volume, pH and viscosity form one side and concentration, morphology, vitality and motility from the other, respectively (Figure 6A). Viscosity is determined by aspirating the sample into a pipette and allowing it to drop by gravity. A normal semen sample forms small discrete drops, while formation of thread > 2cm is indicative of hyper-viscosity which is generally associated with accessory glands disfunction or inflammation [73,74]. The volume of seminal fluid serves as a vital indicator of the overall functionality of the accessory sex glands and a sample is considered normal if the ejaculate volume falls within the range of 1.5 to 6.0ml. The pH measurement of seminal fluid provides valuable insights into the balance between the acidic secretions from the prostate and the alkaline secretions from the seminal vesicles. As per the WHO

recommendations, a pH below 7.2 is considered abnormal. Microscopic analysis is often carried on after the macroscopic one. Concentration measures the number of sperm per semen volume, reflecting reproductive organ functionality [69,70]. Azoospermia is defined as the total absence of sperm in an ejaculate, while total sperm count is employed to categorize patients into various subgroups. Specifically, cryptozoospermia is referred to cases where the sperm count is less than 1 million per ejaculate. Severe oligozoospermia indicates a sperm count ranging from 1 to less than 10 million per ejaculate, while moderate oligozoospermia describes counts between 10 and less than 39 million per ejaculate. On the other hand, normozoospermia was characterized by a sperm count of at least 39 million per ejaculate, along with normal percentages of progressively motile and morphologically normal sperm [75]. For sperm concentration assessment, it is strongly recommended to use a hemocytometer chamber, counting a minimum of 200 cells under a microscope in phase contrast with a magnification of, preferably, 200x. The employment of alternative counting chambers should be validated by comparing their outcomes with the standards set by the improved Neubauer hemocytometer technique and ensuring their effectiveness [76]. The improved Neubauer hemocytometer is a specialized device with two distinct counting chambers, each featuring a microscopic grid of 3 x 3mm lines on its glass surface. It is equipped with a specific thick coverslip, thickness of 0.44mm, which rests atop the grids, supported by slender glass pillars 0.1mm in height.

Sperm morphology is another fundamental aspect to consider in the diagnosis of male infertility. Assessing sperm morphology presents notable challenges due to the pronounced variations in sperm shape both within an individual ejaculate and across different ejaculations. The standard procedure involves placing a well-mixed sperm sample onto a slide, followed by drying, fixing, staining, and subsequent microscopic observation. Abnormalities in morphology often stem from irregular spermatogenesis or maturation. Specific morphological abnormalities are generally classified in head, nek, midpiece and tail defect (Figure 6B) [70]. While the primary classification categorizes sperm as either "ideal" or "abnormal," recognizing abnormalities across all parts of the sperm is fundamental. Therefore, when evaluating a sperm morphology, all its components—the head, midpiece, tail, and any cytoplasmic residues—must be analyzed.

Regarding motility, the degree of forward movement, termed progressive motility, correlates with pregnancy rates [77,78]. The motility of sperm is influenced by temperature, emphasizing the need for standardized conditions, preferably mirroring body temperature, requiring a microscope with a temperature-controlled stage, prewarmed slides, and a sample warmed to 37°C. For consistent assessment, using an eyepiece reticule grid aids in defining the assessment areas, especially in dense sperm samples. Conventional motility analysis categorizes human sperm on the base of their velocity in four main classes: rapidly progressive, which are sperm moving actively, either linearly or in a large circle, covering a distance of at least 25µm (or 1/2 tail length) in one second, slowly progressive, which are sperm moving actively, either linearly or in a large circle, covering a distance, of 5 to < 25µm in one second, non-progressive, which accounts for all other patterns of active tail movements with an absence of progression and immotile which are those with no active tail movements [70]. Based on this manual analysis conducted by an expert operator, a diagnosis can be made.

Specifically, the WHO has established minimum standards that must be met for a sample to be considered healthy. In detail, these minimum values are derived from samples taken from men who naturally achieved oocyte fecundation when attempting unprotected intercourse within 12 months of initiating efforts (Table 1) [79].

Table 1. WHO minimum standards of semen parameters from men in couples starting a pregnancy within one year of unprotected sexual intercourse leading to a natural conception [79]**.**

	Reference value
Semen volume [ml]	1.4 (1.3-1.5)
Total sperm number (10^6 per ejaculate)	38 (35-40)
Total motility [%]	42 (40-43)
Progressive motility [%]	30 (29-31)
Non-Progressive motility [%]	1 (1-1)
Immotile sperm [%]	20 (19-20)
Vitality [%]	54 (50-56)
Normal forms [%]	4 (3.9-4)

These values are established using clinical standards for quantitative lab outcomes and they help differentiate between normal and abnormal semen parameters, but, alone, they do not indicate fertility potential [2]. Indeed, conventional semen analysis does not consider some of the processes which sperm undergo physiologically inside the FRT such as capacitation, acrosome reaction and hyperactivation. Moreover, manual analysis suffers from subjectivity of the operator performing the tests and differences among laboratories which, even respecting the WHO standards, showed substantial differences in their outcome [80,81,82]. This fact clearly indicates the need to develop new male infertility tests to accurately diagnose sperm samples and overcome the limitation associated with their intrinsic subjectivity.

1.5.2. Computer assisted sperm analysis (CASA).

Some laboratories started to use the computer assisted sperm analysis (CASA) based on different algorithms for the analysis of images or recordings to determine both morphological and kinematic sperm features, respectively. These systems are based on the recording of the continuous images, digital processing, and information analysis with the aids of video camera, video capture and computer. CASA systems were firstly introduced in the 1980s and initially they were primarily utilized in research laboratories. Their potential adoption in clinical settings has been considered due to reported benefits such as minimizing subjectivity, reducing human errors, and standardizing the semen evaluation process. Additionally, these systems enable the analysis of a greater volume of samples in a shorter duration, thus enhancing overall efficiency. Consequently, there is a potential shift in laboratories towards automated semen analysis, replacing traditional manual methods for both humans and other mammalian sperm [83]. CASA offers a more detailed evaluation of individual sperm characteristics, providing deeper biological insights, potentially linked to sperm quality and

fertility. Furthermore, advanced CASA systems now incorporate features to assess parameters like vitality, DNA integrity, and acrosome condition, clarifying potential sperm-related issues [72]. Various CASA systems are currently accessible in the market. For instance, the Sperm Class Analyzer (SCA®) by Microptics SL evaluates semen concentration and movement by analyzing images captured through phase-contrast microscopy. The SQA-V GOLD®, developed by Medical Electronic Systems, employs electro-optics to monitor sperm concentration and movement. Meanwhile, the IVOS® and CEROS by Hamilton-Thorne function as image processing tools combined with a microscope and camera (Figure 6D) [71,84]. In a comparative study between manual and automated sperm analysis methods, both techniques yielded consistent results across multiple parameters including concentration, motility, vitality, and morphology. Automated analysis, performed with SCA, demonstrated improved repeatability with lower coefficients of variation than manual methods[85].

Some guidelines for the employment of CASA systems should be respected. When employing CASA, it is essential to ensure that the instrument magnification is correctly calibrated. It is crucial that the magnification allows for the tracking of sperm for at least 0.5s before they exit the visual field. For human specimens, this translates to a minimum field of view of 200 x 200µm, ensuring optimal tracking even for sperm moving at velocities of up to 100µm/s. Form human sperm, an objective with a magnification of maximum 10x should be used to ensure an adequate depth of focus, thereby preserving the integrity of the observed data. However, magnification and objective specifications alone do not guarantee accuracy. Indeed, the temporal dimension is equally crucial: a frequency of at least 50Hz is necessary for reliable analysis. Dilution of high-concentration ($40 - 50 \cdot 10^6$ sperm/ml) samples is preferable with autologous seminal plasma and conducting analyses at 37°C ensure a more physiological condition during the analysis. Regarding the acquisition chambers, it is recommended to employ a depth of 10 – 20µm which is considered optimal [86,87,88]. As for motility evaluation, sperm head centroids are detected and located in multiple microscopic fields and algorithms build the trajectories to monitor sperm movement by evaluating a set of kinematic parameters. The most used ones are the Straight-line velocity (VSL), Curvilinear velocity (VCL) and Average-path velocity (VAP), their combination such as Linearity (LIN), Wobble (WOB) and Straightness (STR) and trajectory related parameters such as mean and maximum amplitude of lateral head displacement (ALH_{mean} and ALH_{max}), Dance (DNC), Beat cross-frequency (BCF) and Mean angular displacement (MAD) (Figure 6C) (Table 2) [70,89].

Table 2. CASA parameters of sperm with the relative definitions.

Parameter	**Definition** [89]
Straight-Line Velocity (VSL) [$\mu m/s$]	Straight-line distance between first and last points of trajectory, corrected for time.
Curvilinear Velocity (VCL) [$\mu m/s$]	Distance travelled by the sperm along its curvilinear path, corrected for time.
Average Path Velocity (VAP) [$\mu m/s$]	Length of the average path, corrected for time.

Linearity (LIN) [%]	Ratio of the straight-line and curvilinear velocity. Expresses the relationship between 3D path and net space gain of cell.
Wobble (WOB) [%]	Ratio between average and curvilinear velocity.
Straightness (STR) [%]	Ratio of straight-line and average velocity. Gives an indication of the relationship between net space gain and cell general trajectory.
Mean amplitude of lateral head displacement (ALH mean) [μm]	Approximation of flagellar beat envelope.
Maximum amplitude of lateral head displacement (ALH max) [μm]	Maximum ALH found along the trajectory.
Dance (DNC) [$\mu m^2/s$]	Measure of the pattern of sperm motion.
Beat Cross Frequency (BCF) [Hz]	Number of times sperm head crosses the direction of movement.
Mean angular displacement (MAD) [°]	Measure of the trajectory curvature.

Among all the kinematic parameters, VSL is the velocity calculated by considering the distance from the initial to the final point of the trajectory, independently of how curved the trajectory is and dividing it by time. VCL, instead, is calculated as the sum of all the segments composing the trajectory from the initial to the final point and dividing by time. Therefore, VSL is an evaluation of the net space gain of the sperm in each acquisition, while VCL evaluate how vigorous is the tracked sperm because it considers how much it deviates from a straight-line path. Thus, by comparing the two velocities, i.e. calculating the LIN, it is possible to characterize a sperm in terms of progressiveness. For example, a circling trajectory would have low linearity, because the curvilinear path would be much higher than the net space gain. A high linearity trajectory is one where the curvilinear path has a relatively low amplitude of oscillation, and the general direction of movement is the same as that of the straight-line path [89]. As the progressivity of sperm is correlated with positive fertilization outcomes, as seen before, the WHO offers a criterion based on the VSL for humans. However, the criterion changes according to the species [70,90,83]. After being tracked and categorized based on their motility, sperm paths are superimposed onto the actual acquisition images by the system. These paths are then color-coded according to their respective categories for easy differentiation. Figure 6E serves as a typical example illustrating the output of the sperm motility analysis [72]. While commercial CASA tools offer certain advantages, they come with drawbacks such as high costs and rigid functionalities, which limit the adoption of these systems in standard clinical procedures. These systems typically do not give access to their algorithms

and original microscope imagery to the users. In addition, it has been found that sperm motion trajectory varies with the frame rate (FR) of acquisition [91,92,93,94]. It has been observed that it exists a relationship between VCL, the most effected kinematic parameter, and the FR of acquisition. The increase of VCL with FR follows an exponential law, whose coefficients change according to the examined species, until a threshold beyond which the VCL reaches a plateau [95]. This obviously led to inconsistent results among systems operating at different FR. Another limitation of CASA system is associated to the low depth capacity of the acquisition chambers employed for the analysis. Indeed, especially for motility, the employment of chambers of 10 – 20µm in depth could limit the observation of the native 3D motility of sperm, confining their motion vertically, given that sperm head is 4 – 5µm wide and the flagellum is 50 – 60µm long. Therefore, since sperm generally describe several types of complex 3D motility patterns, more unconfined geometries with higher depth could give precise information about their behavior [10,21,96]. Additionally, these solutions are not always able to meet research needs and, in response to these challenges, a growing number of researchers have recently developed new open-access and easy to use software (Figure 7) [97,98,99].

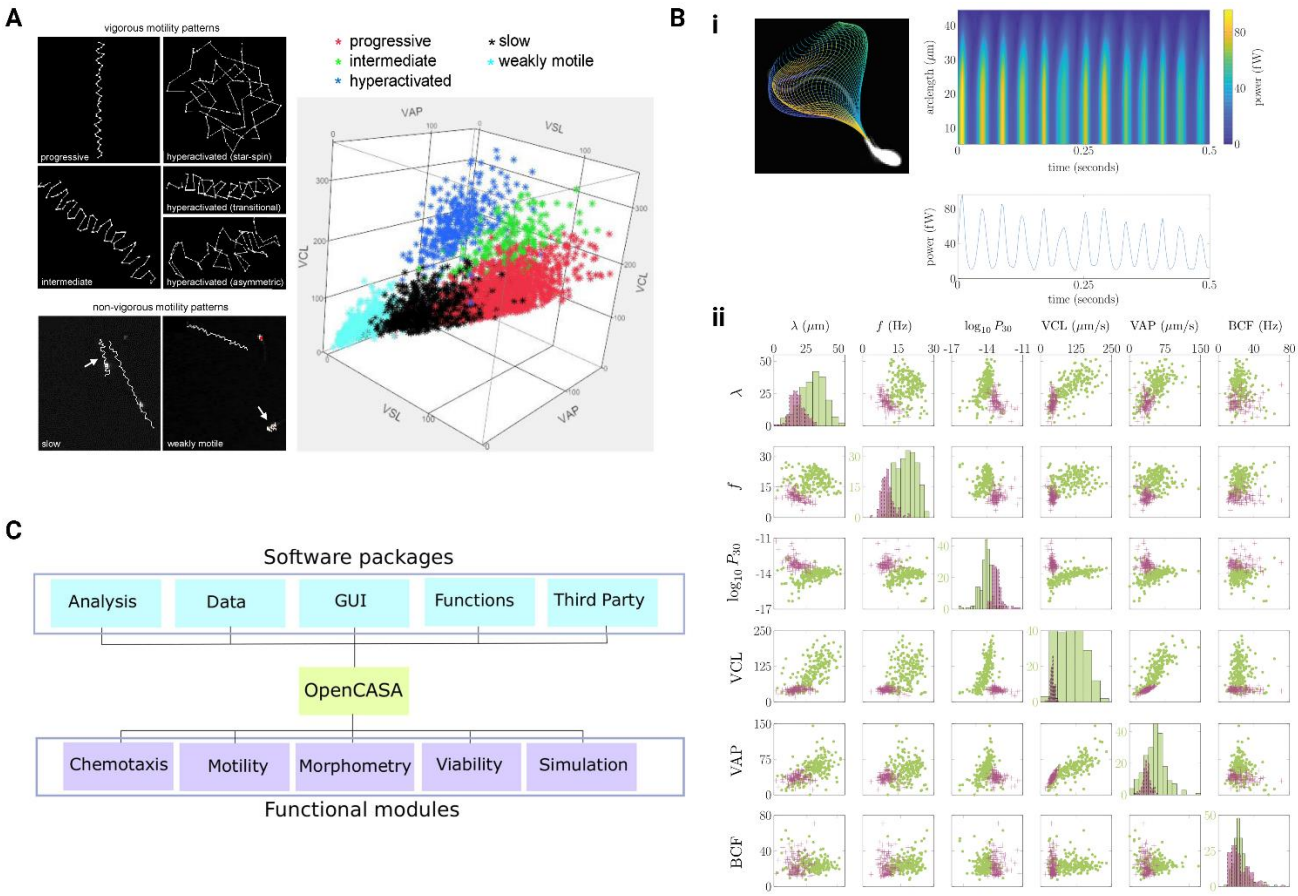

Figure 7. Additional optimized software for sperm analysis. A) (left) Typical human sperm trajectories detected by CASAnova system: progressive, intermediate, hyper-activated, slow and weakly motile. (right) classification of trajectories showed on the left on the base of their velocity values by means of a support vector machine (SVM) equation system. Reproduced from [100]. **B)** (i) Beating pattern of a sperm flagellum reconstructed by Flagellar Analysis and

Sperm Tracking (FAST) with the associated power dissipation. (ii) Scatter plots showing the relationship between tail and head parameters of sperm in low (green) and high (magenta) viscosity conditions. Reproduced from [101]. **C)** OpenCASA software architecture organized into distinct packages based on their specific functionalities. Through these packages, users can conduct distinct sperm analyses using the respective modules: Chemotaxis, Motility, Morphometry, and Viability. Reproduced from [98].

Despite the ability of CASA systems to categorize sperm into sub-classes based on VSL or VCL ranges, they are not able to fully distinguish among sperm trajectories. Specifically, they struggle to identify distinct motion patterns like hyperactivated movements observed in physiological contexts. Therefore, researchers developed an automated method, using a support vector machine (SVM) equation, to classify various patterns exhibited by human sperm. These patterns include vigorous motility types such as progressive, intermediate, hyperactivated, and non-vigorous types like slow and weakly motile. The system achieved approximately 90% accuracy in classifying sperm movements based on five kinematic parameters (Figure 7A). They also created user-friendly software called CASAnova, available online for research purposes, which automatically classifies human sperm movement patterns [100]. Conventional CASA systems allow a precise tracking of mammalian sperm head centroid to calculate their trajectory and evaluate their motility parameters, but it does not give any information about the flagellum beat pattern. Indeed, the movement of the tail could give additional insight into the sperm health. Therefore, Researchers developed a sophisticated automated tracking and analysis method called Flagellar Analysis and Sperm Tracking (FAST) to examine flagellar movement across a large cell population (Figure 7Bi). FAST was evaluated under varying viscosity settings, providing insights into sperm motility in physiological environments, which conventional CASA systems often lack. The system precisely tracked sperm flagella and introduced new parameters such as flagellar curvature, beat frequency, arc-wavespeed, wavelength, and evaluated energy and power dissipation (Figure 7Bi). Relationships between flagellum parameters and conventional CASA parameters were explored, revealing clearer distinctions in sperm swimming behavior across different viscosity levels (Figure 7Bii) [101]. To address the limitation posed by conventional CASA systems, which often restrict access to raw data and underlying algorithms essential for sperm tracking and velocity calculations, some researchers have innovated by introducing an open-source solution. This development, termed OpenCASA, not only provides the software but also offers access to its code, making it compatible with widely used image processing platforms like ImageJ [98]. The code was divided into distinct packages, each designed to a specific set of operations or analyses such as chemotaxis, motility, morphometry, and viability assessments (Figure 7C).

1.6. Microfluidics for sperm selection.

In the context of male fertility, besides the ability to diagnose a sample automatically and/or manually based on its morphology and motility, it is crucial to enhance techniques for selecting optimal sperm for artificial insemination. Many infertile couples rely on assisted reproductive techniques (ART) methods to conceive because either the male or female partner faces total or partial infertility issues. Over the past decades, various insemination techniques have been developed, enabling couples who cannot conceive naturally to achieve pregnancy. The most prevalent ART technique is In Vitro Fertilization (IVF). The procedure involves ovarian stimulation, oocyte retrieval via ultrasound, fertilization outside the body, culturing embryos, and transferring them back to the recipient. A notable advancement in ART is Intracytoplasmic Sperm Injection (ICSI), where a single sperm is directly injected into a mature oocyte. In addition, for individuals experiencing mild male infertility, even after medical or surgical interventions, intrauterine insemination (IUI) might be recommended. The latter consists in a procedure in which laboratory processed sperm are placed in the uterus to attempt a pregnancy [102,103]. Since the inception of the first child born via in vitro fertilization (IVF) in 1978, significant progress has been made in the realm of fertility treatments. However, some reports showed that the success rate of ART remains relatively stagnant at approximately 33% per cycle. This means that many couples often need to undergo several fertilizations attempts before achieving pregnancy [1]. Sperm involved in these ART techniques must be selected from the overall pool contained in the semen sample to choose only the optimal ones. Common approaches for sperm selection mostly rely on swim-up and density gradient centrifugation, picking-up the most motile sperm [104]. The swim-up method is a widely employed technique for sperm preparation, usable with either a cell pellet or a semen sample that has been liquefied. In the traditional approach, a sperm pellet is obtained through centrifugation and is, in turn, gently overlayed with a culture medium in a conical tube. The sample is then incubated at a 45° angle for 1h in a 37°C incubator. The sperm that move farthest from the pellet are collected, as they are more likely to exhibit both high motility and normal morphology. Density gradient centrifugation, instead, separates sperm based on their individual densities, ensuring that each sperm settles at a gradient level corresponding to its density. Morphologically normal and abnormal sperm possess distinct densities: typically, a mature, normal sperm registers a density of at least 1.10g/ml, while an immature or morphologically irregular one ranges between 1.06 and 1.09-g/ml [105]. The more motile, structurally normal, and viable sperm are collected at the tube base. Despite being largely used in the clinic, the traditional sperm selection techniques are unable to select sperm fractions with optimal DNA integrity and functional characteristics [106]. Indeed, the various steps of centrifugation required in these approaches lead to possible damages on cells and DNA, due to the generation of reactive oxygen species (ROS). They can emerge from two primary sources: intracellularly, originating within the gametes, or extracellularly due to external environmental factors. Indeed, DNA damage in sperm has been linked to decreased in vitro fertilization success rates, hindered embryo development prior to implantation, elevated early pregnancy miscarriage rates, and diminished fertility in both natural and assisted conception scenarios [107].

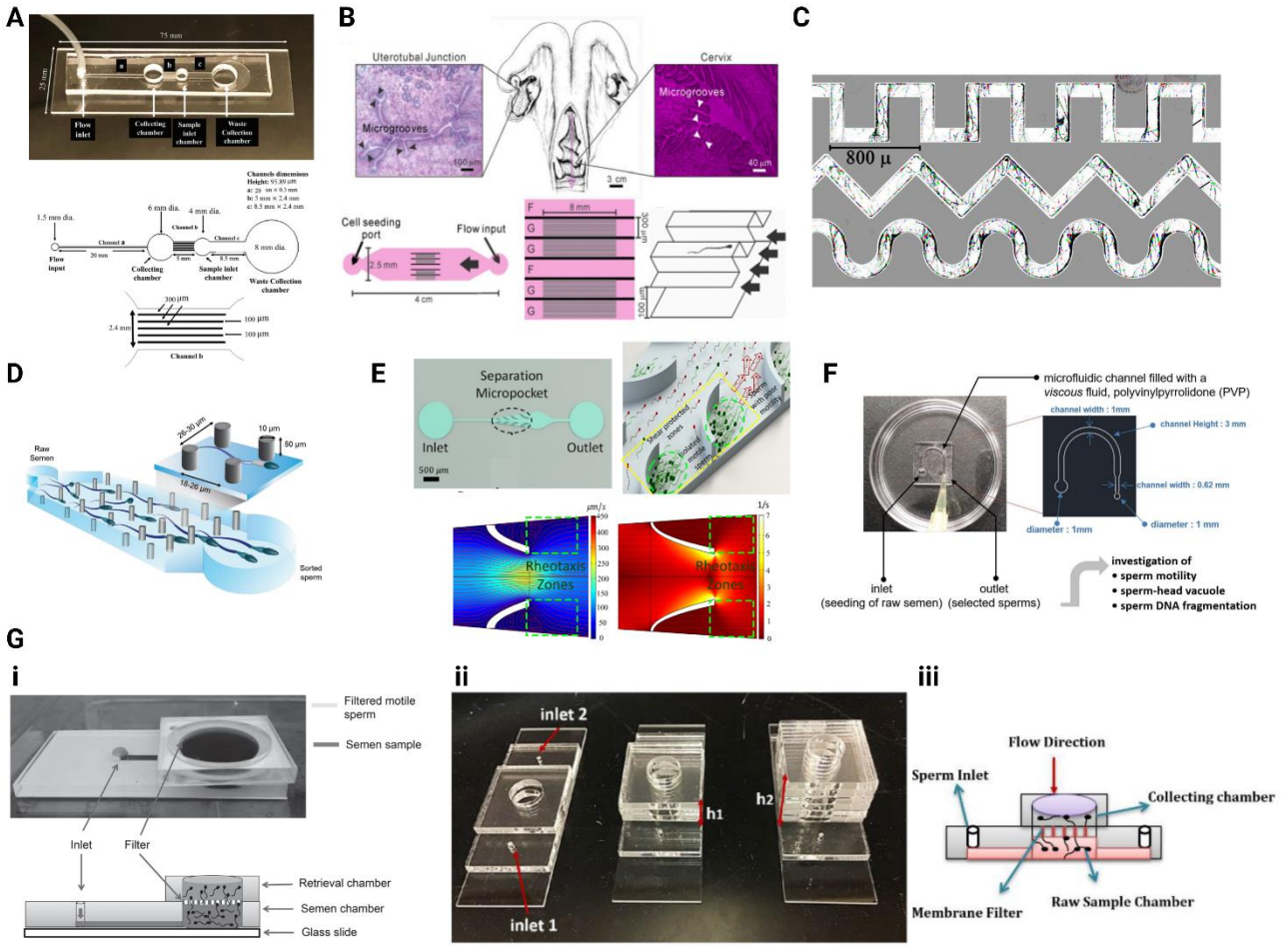

Figure 8. Microfluidic devices for sperm selection. A) PDMS microfluidic device employed for the separation of healthy sperm via rheotaxis from low motile and defective ones. Reproduced from [108]. **B)** PDMS microfluidic device employed to observe sperm motion in fluid-flow and within microgrooves resembling the FRT morphology. Reproduced from [46]. **C)** PDMS Microfluidic device employed to observe sperm boundary following behavior in curved microchannels. Reproduced from [63]. **D)** PDMS microfluidic devices composed of micropillar employed to mimic the filtering activity of the FRT. Defective sperm are filtered from the sample. Reproduced from [109]. **E)** Biomimicry microfluidic device composed by side micro-pockets employed to entrap highly motile and rheotactic sperm. Reproduced from [65]. **F)** PDMS microfluidic device filled with highly viscous fluids mimicking the mucus within the FRT. Reproduced from [110]. **G)** (i) FDA-approved microfluidic device (Zymōt®) employed for the selection of healthy sperm for ART applications. (i) static version [111]. (ii) Dynamic version with the application of fluid-flow. (iii) schematic representation of the device in (ii) [112].

The limitations associated with the selection techniques employed for ART applications highlight the need for the improvement of selection methods capable of handling a large number of sperm, in a way that does not influence them negatively and that it does not bypass the natural barriers that they must overcome within the FRT. In this regard, microfluidics offers many possibilities to manipulate sperm samples and select them by means of two main approaches: passive and active methods. Active methods utilize external triggers, like temperature variations or chemical gradients, to facilitate sorting, whereas passive methods depend on the

natural behavior and movement of sperm without external influences [52,113]. Several researchers focused their attention on the combination of morpho-physical interaction which sperm have within the FRT such as fluid-flow and morphology of the surrounding environment (Figure 8). As a first example is the employment of the natural rheotaxis behavior of sperm which led to the development of a polydimethylsiloxane (PDMS) microfluidic chip that isolate healthy sperm (Figure 8A) [108]. The microchannels here are lined up with microgrooves resembling those present in the FRT which act as preferential pathways, guiding sperm exhibiting positive rheotaxis to move in a specific direction due to the narrowed dimensions of the grooves (Figure 8B) [46,114]. It has been found that bovine sperm swimming within 20 x 20μm microgrooves, against an applied flow, exhibited greater persistence in that direction compared to those swimming on a flat surface. Additionally, they observed that, besides being more directed within the microgrooves rather than on a flat surface, sperm also exhibited greater resistance to the flow. Sperm selected in this way were then analyzed using a CASA system to assess their quality compared to a control sample. They observed that the rheotaxis-separated sperm displayed a higher percentage of motility, a greater degree of normal morphology, higher values for VSL, VCL, and VAP, and notably, a significantly lower DNA fragmentation level compared to the starting sample. This demonstrated the capability of microfluidics to obtain, from an heterogenous sample, sperm with good DNA quality and optimal motility and/or morphology. Moreover, in microfluidic PDMS channels, human sperm were observed to predominantly follow the channel boundaries rather than navigating the bulk. They tended to stick to the channel walls, particularly where the channel curves were sharper, exiting the wall when the curvature was less than approximately 150μm (Figure 8C). Interestingly, the concentration of sperm swimming around these corners could be up to 200 times greater than those swimming freely in the bulk of the channel. Such findings shed light on how sperm might navigate within intricate parts of the FRT, particularly in areas like the fallopian tubes with their complex folds and narrow passages [63]. A micro-pillar PDMS chip was then produced, drawing inspiration from the filtration mechanisms observed in vivo, aiming for the non-invasive extraction of high-quality sperm (Figure 8D). This technique notably improved the quality of the separated human sperm in terms of morphology, nuclear maturity, and DNA preservation [109]. Through this method, 99% of the actively motile sperm were effectively isolated within 10min, modulating the directional persistence of sperm and increasing the spatial separation between progressive and nonprogressive. Notably, they found a pronounced prevalence of sperm with standard morphology, approximately 52%, when employing their method to select them. This contrasts with 24% with the swim-up method, and merely 13% from untreated semen. Still from a morphological point of view several studies observed a good retention of positive rheotactic sperm in microfluidic devices having micro-pocket geometries that recall the oval-shaped microstructures of the female fallopian tube to create shear protected zones for sperm separation (Figure 8E) [65]. Clinical tests with human samples indicate that the device can isolate viable and highly motile sperm based on their rheotaxis responses, resulting in a separation efficiency of 100% [55,115,116]. The latter is a very clear demonstration of the ability of microfluidic systems to select healthy sperm by employing geometry design and fluid-flow properties. The physiologically-like context has been reproduced also in terms of rheological properties of the surrounding medium by means of microfluidics. It has been explored the natural

filtration process sperm undergoes as it traverses from the vagina to the uterus, where cervical mucus typically screens out sperm with low motility and abnormal morphology. To emulate this physiological process, a polymethylmethacrylate (PMMA) microfluidic chip has been developed and filled with a viscous solution of PVP, mirroring the properties of the human cervical mucus in static conditions. The device is thought to simulate the passage that human sperm must travel from the vagina to the fallopian tubes, with the restriction in width at the end representing the UTj (Figure 8F) [110]. Within a span of 40min, this chip managed to completely filter out undesired components such as debris, immotile sperm, white blood cells (WBCs), and red blood cells (RBCs) from the semen. The PVP-loaded chip performed better than control-filled device in sperm isolation; indeed, the control medium (low viscosity) displayed a mix of motile sperm and debris at the outlet. This demonstrates the filtering ability of the cervical mucus within the FRT. These microfluidic devices were developed to demonstrate the ability to go beyond the limitation of conventional selection techniques, but they were never employed in clinical practice. However, there is a particular type of PMMA microfluidic device which was approved by the Food and Drug Administration (FDA) to be used in the selection process of sperm for ART applications. The Zymōt® (DxNow, Inc. Gaithersburg, MD USA) chip is designed to extract motile sperm from semen for procedures like IUI, IVF and ICSI offering enhanced efficiency compared to conventional sperm preparation methods (Figure 8G). It is user-friendly, avoiding the need for specialized media, thereby reducing training and it operates on the principle of motility-based separation. It allows to work with a wide range of semen types, including those with low counts, reduced motility, high viscosity, minimal volume, or even frozen samples and it comes in three main versions: Zymōt Multi (850 µl), Zymōt Multi (3 ml) and Zymōt ICSI (www.zymotfertility.com). This microfluidic device has been shown in two main operational settings, i.e. with flow and without flow [111,112,117]. In both cases it is composed by two main PMMA components: an upper chamber and a lower chamber between which a track-etched polycarbonate membrane filter is placed. The bottom chamber is connected to an inlet by means of a channel though which the sample is loaded. The polycarbonate membrane is characterized by micropores with variable dimensions (3, 5 and 8µm) allowing only the passage of the most motile and functional sperm against gravity, leaving behind dead and less motile ones (Figure 8G i). The so-selected sperm are, in turn, collected in the upper chamber. For the with flow device, additional layers of PMMA were added to the top chamber in order to create varying hydrostatic pressures (h_1 and h_2 in Figure 8G ii and Figure 8G iii). This microfluidic device showed optimal results in terms of separation efficiency by selecting sperm with higher motility, higher degree of normal morphology and a strong reduction in DNA fragmentation when compared with swim-up method.

1.7. Proposed approach.

After exploring the global landscape of fertility trends, the intricate structure of mammalian sperm, and their complex locomotion within 3D environments, it becomes imperative to explore how they adapt and interact within the FRT. Indeed, conventional semen analysis and selection does not consider the intricate interaction which sperm undergo during their journey. Traditional semen analysis methodologies have rendered precious insights over the years; however, the progress of modern technology cannot be overlooked. The CASA systems, for instance, have revolutionized the detailed assessment of sperm characteristics and offered precision and efficiency, but still show some limitations. Concurrently, microfluidics has emerged as a groundbreaking technology, enabling sophisticated sperm selection and analysis techniques that were once beyond imagination. Recognizing the potential of these advancements, this research aims to bridge the gap between conventional techniques and cutting-edge methodologies. As a contribution to reproductive biology, this study aims to bring advancements that could expand the knowledge of existing literature and to help improve the research in the field as an additional tool to existing technologies. To do so, bovine cells were employed as a representative model for mammalian sperm. We experimentally observed the influence of both geometrical constraint and viscosity on sperm motility and motion behavior. Here, we investigated the effect of fluid rheology within the FRT, observing how sperm adjust their movement to this specific microenvironment. We evaluated sperm motility parameters by reconstructing their trajectories frame by frame. Utilizing established literature, we categorized sperm into distinct motility sub-classes based on their VCL [70,83]. Additionally, we focused to the impact of fluid dynamics on sperm motility. We analyzed sperm rheotactic response in varying viscosity conditions, aiming to isolate and select cells based on their progressive motility. This was performed by means of an in-house produced microfluidic device whose design has already been published elsewhere [108]. This device not only facilitated precise fluid-flow control but also enabled the separation of rheotactic sperm from less motile counterparts within a heterogeneous sample. Our subsequent analysis quantified the proportion of motile versus immotile cells within the selected group and compared it with the discarded ones. Furthermore, we explored the intricate rolling component of bovine sperm motion, assessing its frequency and discerning how 3D movement patterns are modulated by fluid-flow and viscosity. Moreover, we also quantified the amount of rolling and no rolling sperm in the different rheological conditions and proposed a selection mechanism which exploits a combination of motion pattern and fluid-flow. In this way we were able to characterize bovine sperm motility in a physiological-like context which resembles the conditions in which they are found to navigate to reach the oocyte. Lastly, as a proof of concept, we implemented the same experimental conditions also to human sperm. This research could offer additional insight into the analysis and selection of sperm for ART applications and expand the knowledge about sperm locomotion and its modulation by morpho-physical factors.

2. Bovine sperm swimming in static conditions.

Sperm exhibit a 3D motion comprising translational and rotational components, often described as a conical helix during their movement. However, conventional analysis methodologies, both manual and automated, tend to restrict the observation of this complex 3D motion. This limitation arises from the use of small observation chambers typically ranging from 10 to 20μm in depth. Given that sperm have a head width of 4–5μm and a flagellum length of 50–60μm, these chambers confine their motion vertically. Therefore, the use of confined geometries with shallow depths may restrict the ability to accurately capture their behavior. Employing unconfined geometries with greater depth could provide more precise insights into sperm behavior, especially concerning motility analysis. In addition, conventional analysis typically involves assessing sperm motility in contexts that do not accurately replicate physiological conditions, such as cervical mucus characterized by increased viscosity. Analyzing this aspect under conditions of variable viscosity provides information that closely replicates what occurs in vivo and thus offers greater reliability [9,20,70,86].
Here we experimentally investigated the effects of both fluid rheology and geometrical confinement on frozen-thawed bovine sperm motility in static conditions. We acquired free swimming sperm in different viscosity media by means of both brightfield and phase contrast modalities and analyzed them by means of a self-written MATLAB® routine, developed by the group (see Appendix A for details). We extracted sperm trajectories and calculated the motility parameters mainly associated with progressivity, i.e. VSL, VCL and LIN. In addition, by means of manual analysis of head trajectories, we evaluated some parameters related with sperm rolling such as rolling frequency, angular rolling velocity and quantified the amount of rolling and no rolling cells in the different rheological conditions. In addition, for no rolling sperm we evaluated their circular trajectories along with the radius of curvature.

2.1. Material and Methods.

2.1.1. Reagent and Media.

Cryopreserved bovine sperm were prepared by using pre-warmed Sydney IVF Gamete Buffer (Cook medical) (details in 2.1.2). Their motility was evaluated in three solutions having different viscosities: a low viscosity, consisting in the same buffer used for the preparation of the sample, and two polymeric solutions of PVP (360kDa – Merck KGaA, Darmstadt, Germany). The polymeric solutions were obtained by dissolving the polymer powder in Phosphate Buffered Saline (PBS) solution at a concentration of 2wt% and 5wt%, having increased viscosity and employed as a cervical mucus analogue.

We assessed the viscosity of the three solutions used in our experiments using a stress-controlled rheometer (MCR 302, ANTON PAAR) with a cone-plate geometry (1deg - 50mm). Specifically, we examined: a diluted solution containing the gamete buffer as a control (referred to be the CTRL condition) with low viscosity, and two concentrations of PVP (360kDa) at 2wt% and 5wt%, representing intermediate and high viscosities, respectively. The zero shear viscosities of these solutions were measured to be $0.001\ Pa \cdot s$, $0.01\ Pa \cdot s$, and

0.1 $Pa \cdot s$, covering three orders of magnitude. The three solutions were tested across a broad range of shear rates, encompassing three orders of magnitude from 1 $s^{-1}$to 10^3 s^{-1}. The resulting flow curves indicated a Newtonian behavior for both PVP concentrations, exhibiting nearly constant viscosity throughout the explored shear rate range (Figure 9). These values closely mirror the viscosity levels observed in cervical mucus during ovulation. Indeed, it is worth noting that human cervical mucus at midcycle typically registers a viscosity of 0.2 $Pa \cdot s$ [36]. Moreover, various studies employed polymeric solutions with viscosities ranging from 0.04 to 0.4 $Pa \cdot s$ during the estrous (ovulatory) phase of the menstrual cycle, specifically for bovine sperm [41,45]. From now on we will refer to these three conditions as CTRL, intermediate viscosity, and high viscosity, respectively.

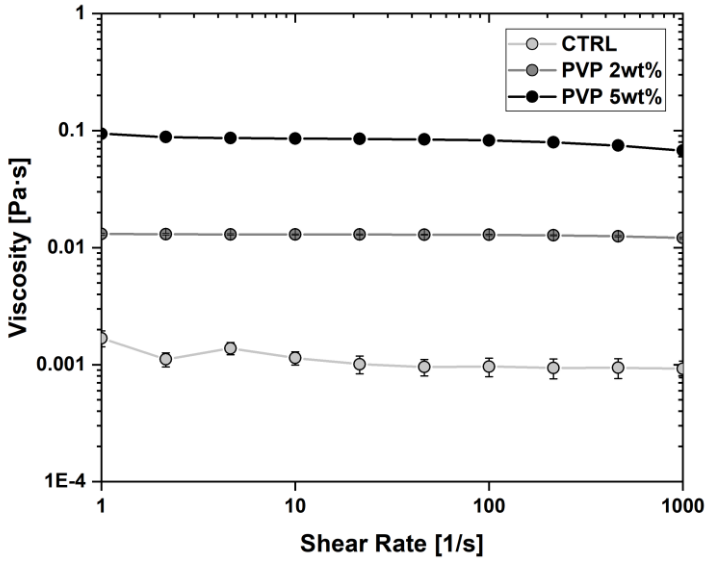

Figure 9. Viscosity measurements of PVP solutions. The viscosity ($Pa \cdot s$) is plotted against the shear rate (s^{-1}) for three conditions: CTRL (Gamete Buffer – light grey), which has water viscosity, PVP 2wt% (intermediate viscosity – dark grey) and PVP 5wt% (high viscosity - black). The curves show a Newtonian behavior, being the viscosity constant with shear rate. The three curves represent the average value obtained from three measurements and the relative standard deviation.

2.1.2. Sample Preparation.

Cryopreserved bovine sperm were purchased in frozen straws from ABC Love Genetix (CONSWORK srl, Lodi, Italy) and stored in liquid nitrogen until the experiment. The straws contain 500µl of semen at a concentration of $15 \cdot 10^6$ sperm/ml. For each experiment, a straw was retrieved from the liquid nitrogen container and left in an oven at 37°C in a water bath for 1min to unfreeze. Afterwards, sperm were washed 2 times using pre-warmed Gamete Buffer and isolated from cryoprotectant by centrifugation (200x g for 5min

at 25°C) [41]. In details, Gamete Buffer was firstly layered on top of the sperm sample with a ratio 5:1 (2.5ml of buffer on 500µl of sample) and centrifugated. At the end of the first centrifuge, the supernatant was removed, and the procedure was repeated equally. The so obtained procedure led to the production of a sperm pellet on the base of the centrifuge tube which was in turn re-suspended in Gamete Buffer to a final sample volume of 500µl. The sample was then diluted into the three solutions having different viscosities (Figure 10A). The washing of samples through centrifugation was necessary as we observed that, when diluting the samples in PVP solutions without first eliminating cryoprotectants and substances present in the cryopreservation fluid, resulted in the production of debris. These substances, likely insoluble in the used solutions, generated particles that adhered to the sperm heads. This led to difficulties in microscopic visualization, hindering clean acquisition, and interfered with sperm motion, causing stress to the cells.

2.1.3. Acquisitions.

The optical set-up employed for the acquisitions was constituted by an inverted microscope (Olympus, IX81) equipped with a CMOS camera (ORCA FLASH 4.0, Hamamatsu Photonics K.K.) to acquire brightfield and phase contrast recordings (Figure 10B). Brightfield acquisitions of 1s were employed for sperm tracking, trajectory reconstruction and motility parameters estimation, while phase contrast acquisitions of 5s were employed for the evaluation of sperm rolling component and the related parameters. The use of phase contrast allowed us to better appreciate sperm head rolling due to the higher contrast produced into the image. Acquisitions were performed with an objective magnification of 20x, a frame rate of about 45 frames per second (fps). The experimental set-up was constituted by two observation supports having different depth to evaluate the influence of both viscosity and geometrical confinement on sperm motility. The supports used included standard counting chambers commonly employed by CASA systems for analyzing mammalian sperm, as well as rectangular glass capillaries. The counting chambers were purchased from MICROPTIC (MICROPTIC S.L., A Hamilton Thorn Company, Barcelona, Spain) and are specifically designed for sperm motility analysis. They feature a depth of 20µm and are equipped with six separate chambers, allowing for simultaneous analysis under multiple conditions. In contrast, the glass capillaries were purchased from CM Scientific (CM Scientific Ryefield (EU) Ltd.) have a rectangular cross-section measuring 200 x 2000µm, therefore providing a 10-fold increase in depth (Figure 10C). The same sample was employed for the analysis of sperm motility in both supports and in all the rheological conditions. For the 20µm counting chamber, a sperm concentration of $3 \cdot 10^6$ sperm/ml was used, with 4µl of the sample loaded by means of a pipette. In contrast, for the 200µm deep glass capillaries, the concentration was adjusted to $3 \cdot 10^5$ sperm/ml. This capillary was immersed in the sample vial, allowing for filling via capillarity.

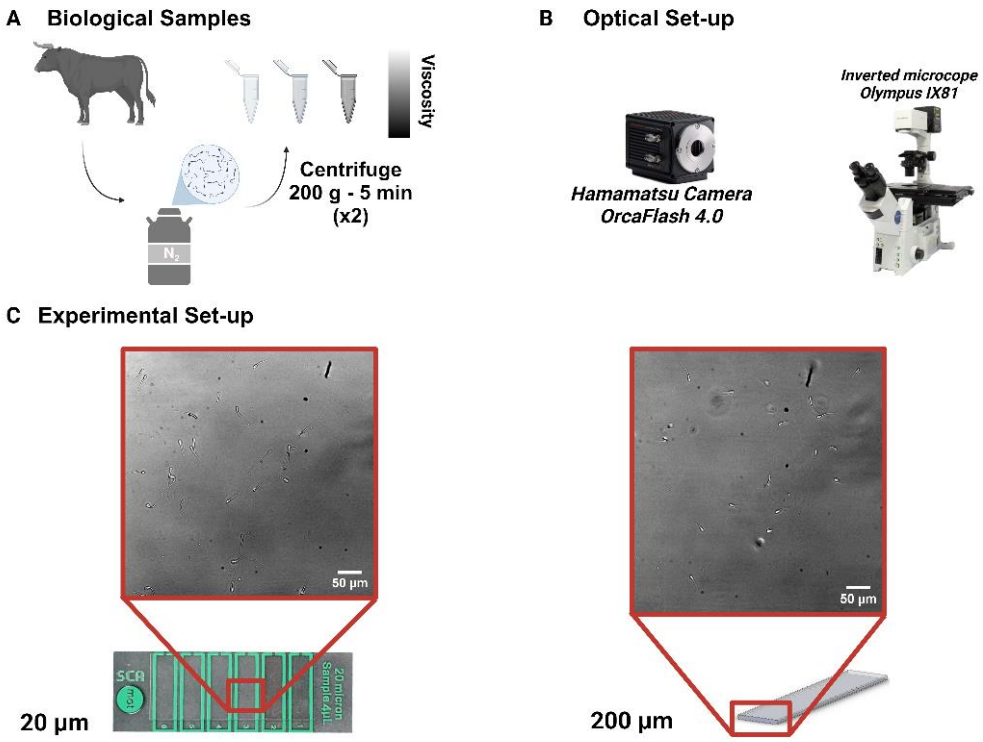

Figure 10. Bovine sperm analysis in static conditions. A) Cryopreserved bovine sperm were employed in the analysis and washed two times by centrifuge, before being diluted at the desired concentration in the three viscosity solutions. **B)** Optical set-up employed in the analysis. An inverted microscope and a rapid CMOS camera were employed for both brightfield and phase contrast acquisitions at 45fps. **C)** Experimental set-up. Two different supports with different depth have been employed for the analysis: SCA® motility chamber of 20µm in depth, referred to as "confined condition" and a rectangular glass capillary of 200µm, referred to as "unconfined condition". Real images of bovine sperm swimming in both supports are shown in the image as a representative example of our brightfield acquisitions.

2.1.4. Data Analysis.

Single sperm heads were tracked with a self-written MATLAB® routine (version 2022b - The MathWorks Inc.) which was able to detects the apparent head centroid (AC) coordinates, being the brightest point in the sperm head area. The routine then links all the points detected to reconstruct the sperm trajectory over the 1s brightfield recordings. Once the tracks were evaluated, we computed VSL, VCL, LIN according to the definitions of CASA terminology [89] (Table 2) (see Appendix A for details about motility parameters computation). We, then classified cells in motility sub-classes according to the criterion used in SCA® instruments, specific for bovine sperm and based on VCL (Table 3) [83].

Table 3. Motility sub-classes definitions according to literature [83]**.**

Class	VCL $[\mu m/s]$
Not Progressive	$VCL < 25$
Slow progressive	$25 < VCL < 80$

Medium progressive	$80 < VCL < 150$
Rapid progressive	$VCL > 150$

Additionally, we also performed a manual analysis on the 5s phase contrast recordings. Each sperm was tracked for 1s by manually tracing an oval selection around the head and following it frame by frame, by means of ImageJ. The manual analysis allowed us to evaluate the rolling component of bovine sperm motility and the related parameters, such as, the rolling frequency (s^{-1}) and the angular rolling velocity (rad/s). For the no rolling sperm, which swim in circles, we also evaluated the radius of curvature (R) of the described trajectory along the 5s recording by means of circle fitting. The 5s duration was necessary to plot a sufficiently long trajectory for a good circular reconstruction. We additionally conducted manual analyses to assess various morphological parameters of the sperm head, including its area, length, width, and thickness. Additionally, using 100x magnification in brightfield, we measured the length of the bovine sperm flagellum. This higher magnification was necessary due to the slender nature of the flagellum compared to the head, ensuring clearer visualization. Measurements of the flagellum length were taken when it was as straight as possible.

2.1.5. Statistical Analysis.

Statistical analysis was performed with the MATLAB® function '*kruskalwallis*'. The comparison was performed for a specific parameter among different conditions. A p-value lower of 0.05 was considered statistically significant and we implemented the following notation to define the degree of significance: NS for p-value > 0.05, * for p-value < 0.05, ** for p-value < 0.01 and *** for p-value < 0.001.

2.2. Results and Discussion.

2.2.1. Morphological analysis of bovine sperm head and tail.

We performed head morphological analysis by manual tracking bovine sperm head in 20x phase contrast acquisitions and distinguished between two main configuration which they assume while swimming (Figure 11).

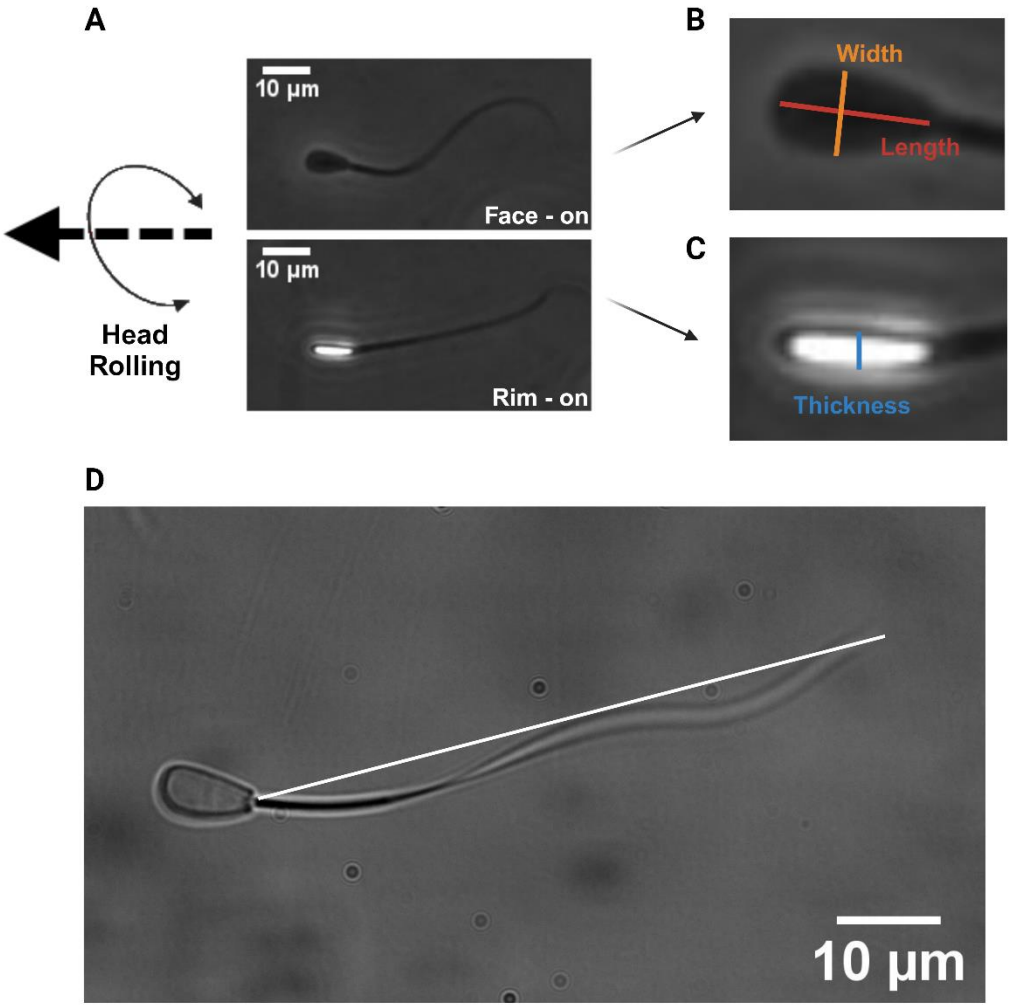

Figure 11. Representation of bovine sperm morphological analysis. A) Real images of a bovine sperm in free swimming exhibiting head rolling around its propulsion axis (represented by the black arrow on the left) (20x magnification – Phase contrast). The two configurations assumed by the sperm are clearly shown and named "Facen-on" and "Rim-on". **B)** Zoom-in of the sperm head in the Face-on configuration showing its two main dimensions: the width (in orange) and the length (in red). **C)** Zoom-in of the sperm head in the Rim-on configuration showing its thickness (in blue). **D)** Real image of a bovine sperm in a 100x – brightfield acquisition. The tail length measured is shown in white, superimposed on the real image. It was determined when sperm tail was as straight as possible.

The intricate 3D movements executed by sperm, exploiting both translational and rotational motion, are clearly captured in phase-contrast images focused on their heads. Owing to the distinctive paddle-shaped structure of their heads -where the length and width are significantly larger than the thickness- certain periodic characteristics become apparent during rotations along their swimming axis. Specifically, within the plane of acquisition, two predominant features emerge, which we have termed the 'Face-on' and 'Rim-on' configurations (Figure 11A). In 'Face-on', the sperm head presents its broad length and width to the observer. Conversely, in 'Rim-on', it exposes the thickness (Figure 11B and C). By surrounding the head with an ellipse in the two configurations, we were able to retrieve the morphological metrics. These included the head area in each configuration, as well as the measurements of length, width, and thickness (Table 4).

Table 4. Measured morphological parameters of bovine sperm head and tail. For the head and tail, N=174 and N=74 cells were analyzed, respectively.

Dimension	
Head Area (Face-on) [μm^2]	38.16 ± 4.49
Head Area (Rim-on) [μm^2]	14.92 ± 2.72
Head Length [μm]	9.00 ± 0.61
Head Width (Face-on) [μm]	5.22 ± 0.43
Head Thickness (Rim-on) [μm]	2.15 ± 0.34
Tail Length [μm]	57.26 ± 2.83

The measured head parameters are in good agreement with existing literature about morphometrical evaluation of bovine sperm head [10,41]. Morphological analysis was performed also regarding the tail length. In this case, 100x brightfield acquisitions were performed since the features of sperm flagellum are much smaller than its head. We evaluated the tail length by measuring it in the straightest configuration it assumed in the recording (Figure 11D) (Table 4). The collected data aligned well with findings from literature [10].

2.2.2. Geometrical influence on bovine sperm motility parameters.

For the CTRL condition, we tested two different geometries to explore how chamber dimensions can affect sperm motility. Specifically, we refer to the 20µm chamber as the "confined condition" due to its depth being comparable to the typical dimensions of bovine sperm. In contrast, the 200µm capillary is referred to be an "unconfined condition" since its dimensions are higher than typical sperm size. The results show that both VSL and VCL for sperm swimming in the 200µm capillary are higher than those in the 20µm counting chamber (Figure 12A and B). Specifically, the VSL is roughly 3% greater in the 200µm capillary compared to the 20µm chamber, while, the VCL shows a more pronounced increase, exceeding 14% in the larger capillary, as already demonstrated in literature [114]. This significant rise in VCL suggests that the geometry has a more substantial impact on the curvilinear component of sperm movement, influencing its vertical motion rather than merely reducing the overall distance traveled by the sperm. Regarding the LIN parameter, there is no difference

between the two depths, eliciting no relevant alteration in progressive motility (Figure 12C). This observation is further supported by the fact that the VSL, although to a lesser extent, is also higher in the 200µm capillary compared to the 20µm one, compensating the higher VCL and then returning not altered LIN values.

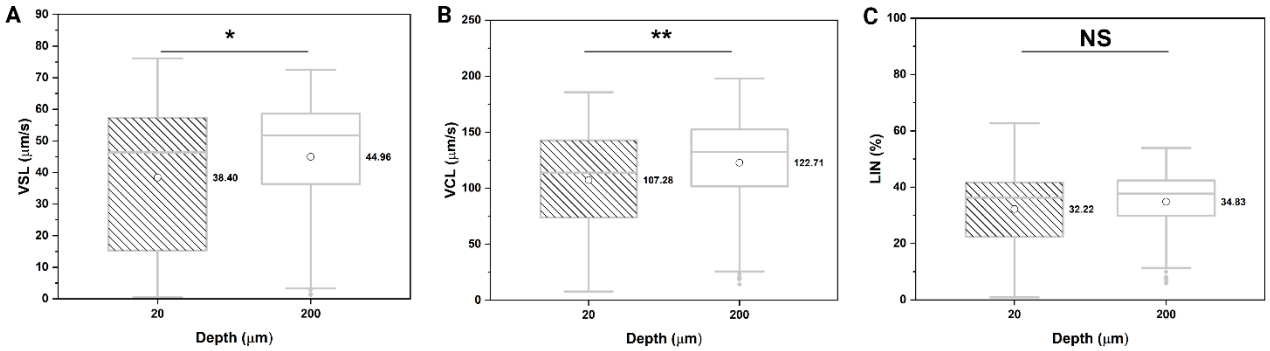

Figure 12. Influence of geometric confinement on bovine sperm motility. A) VSL. **B)** VCL. **C)** LIN. The values are shown as box charts displaying standard deviations, average values indicated by the white dots and specified by the number in bold, and median values represented by the horizontal lines inside the box. The patterned box charts indicate the confined condition (20µm in depth), while the un-patterned ones indicate the unconfined conditions (200µm in depth). $N_{20\mu m} = 140$, $N_{200\mu m} = 169$. VSL and VCL are statistically significant, while LIN is not (p-value < 0.05, p-value < 0.01 and p-value > 0.05, respectively).

2.2.3. Fluid viscosity influence on bovine sperm motility parameters.

Sperm samples were mixed with varying viscosity solutions: CTRL, intermediate and high. It can be appreciated a strong influence of viscosity on bovine sperm velocity. Indeed, in the 20µm chamber, both VSL and VCL gradually decreases as viscosity increases (Figure 13A and B). Notably, VSL decreases by 41.6% and 68.2% with increasing viscosity, while VCL exhibits higher reduction, with declines of 51.4% and 75.5% over the respective viscosity levels (Figure 13A and B), leading to a decrease of sperm curvilinear oscillation and to a more periodic and ordered trajectory. This is further confirmed by looking at LIN (Figure 13C) which instead has an opposite trend to the one of the velocities. As a matter of fact, it follows an increasing trend as the viscosity of the solution increases, suggesting an enhancement in progressivity. The highest variations are observable between CTRL and intermediate viscosity, as well as between CTRL and high viscosity, in good agreement with literature findings [45]. On the other hand, there is no significant variation of LIN between the intermediate and high viscosity solutions. This is clearly explained considering that, being the VCL the more attenuated parameter, this leads to a higher LIN which is related to higher progressivity and a planarized movement.

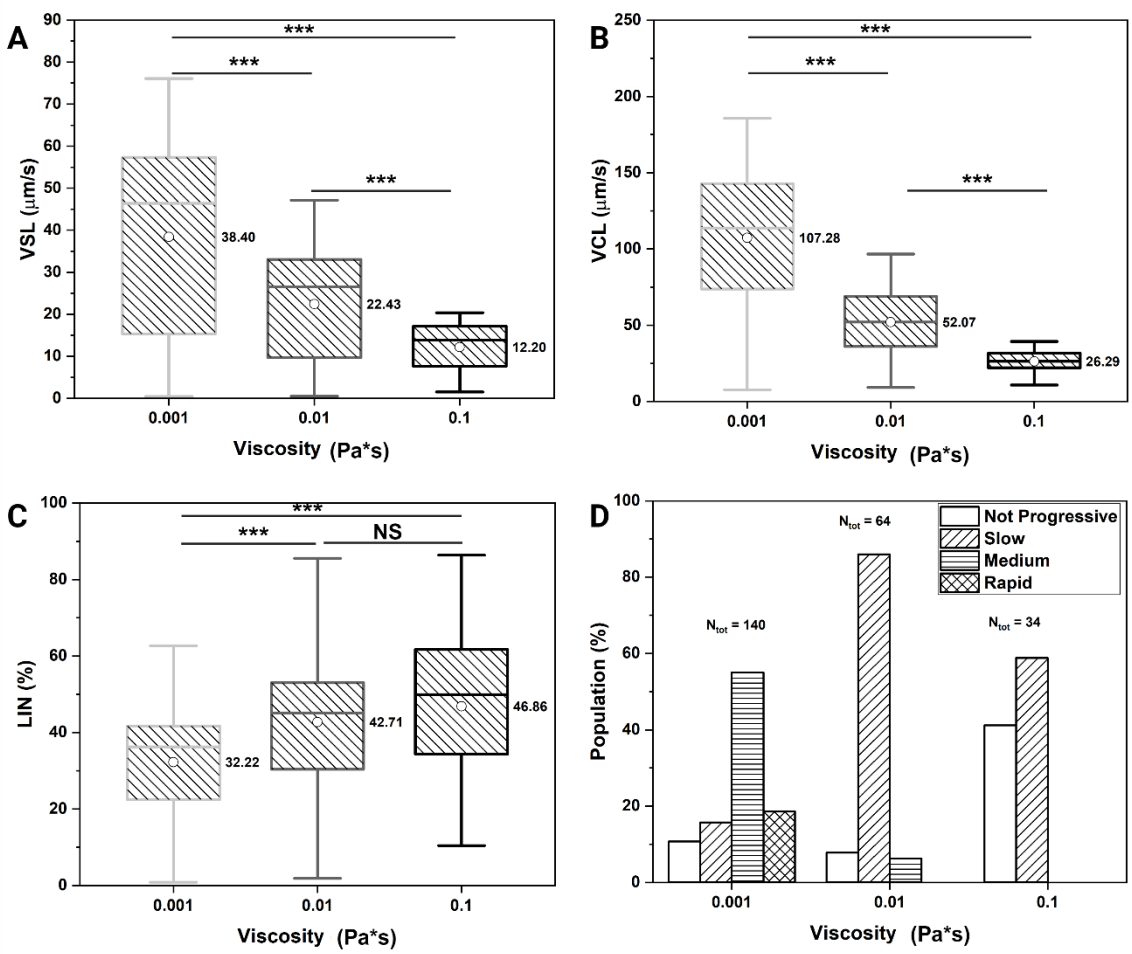

Figure 13. Influence of viscosity on bovine sperm motility in confined conditions (20µm). A) VSL. **B)** VCL. **C)** LIN. The values are shown as box charts displaying standard deviations, average values indicated by the white dots and specified by the number in bold, and median values represented by the horizontal lines inside the box. $N_{0.001} = 140$, $N_{0.01} = 64$ and $N_{0.01} = 34$. p-value < 0.001 for almost all the conditions compared among them. The exception is LIN between 0.01 $Pa \cdot s$ and 0.1 $Pa \cdot s$ where p-value > 0.05, indicating not statistically significant (NS). **D)** Classification of motile bovine sperm based on VCL in: Not Progressive, Slow, Medium and Rapid according to the ranges in Table 3. The amount of sperm classified is the same of the other plots and are reported on top of the bar plots. The amount of sperm falling in each sub-class is represented here as percentages.

VCL values were used to classify bovine sperm into motility sub-classes by employing the ranges used by SCA® systems, namely Not Progressive, Slow, Medium, and Rapid (Table 3 and Figure 13D). In details, at CTRL, the majority of sperm are Medium (~55%) with a substantial amount of Rapid (~20%) since their motion is not hindered by fluid drag (i.e. their propulsive force is strong enough to overcome the resistance of the fluid). On the other hand, at intermediate viscosity, we can note a completely absent Rapid class, and a large increase of the Slow class (~ 87%). Moreover, at high viscosity the total of the detected sperm falls in the Not Progressive and Slow classes. This dominance implies that the increased viscosity may exert a strong drag force on the sperm, causing them to become entrapped and decelerate. The observed transition of sperm

from Medium to Slow at intermediate viscosity, and further from Medium to Slow and Not Progressive at high viscosity, it is closely bound to the diminishing VCL values (Figure 13B). It is noteworthy that the number of motile sperm detected tend to decrease as the viscosity increases (Figure 13D) indicating that not only sperm decelerate, but also that they might be entrapped by the high-viscosity solution, which effectively stops them.

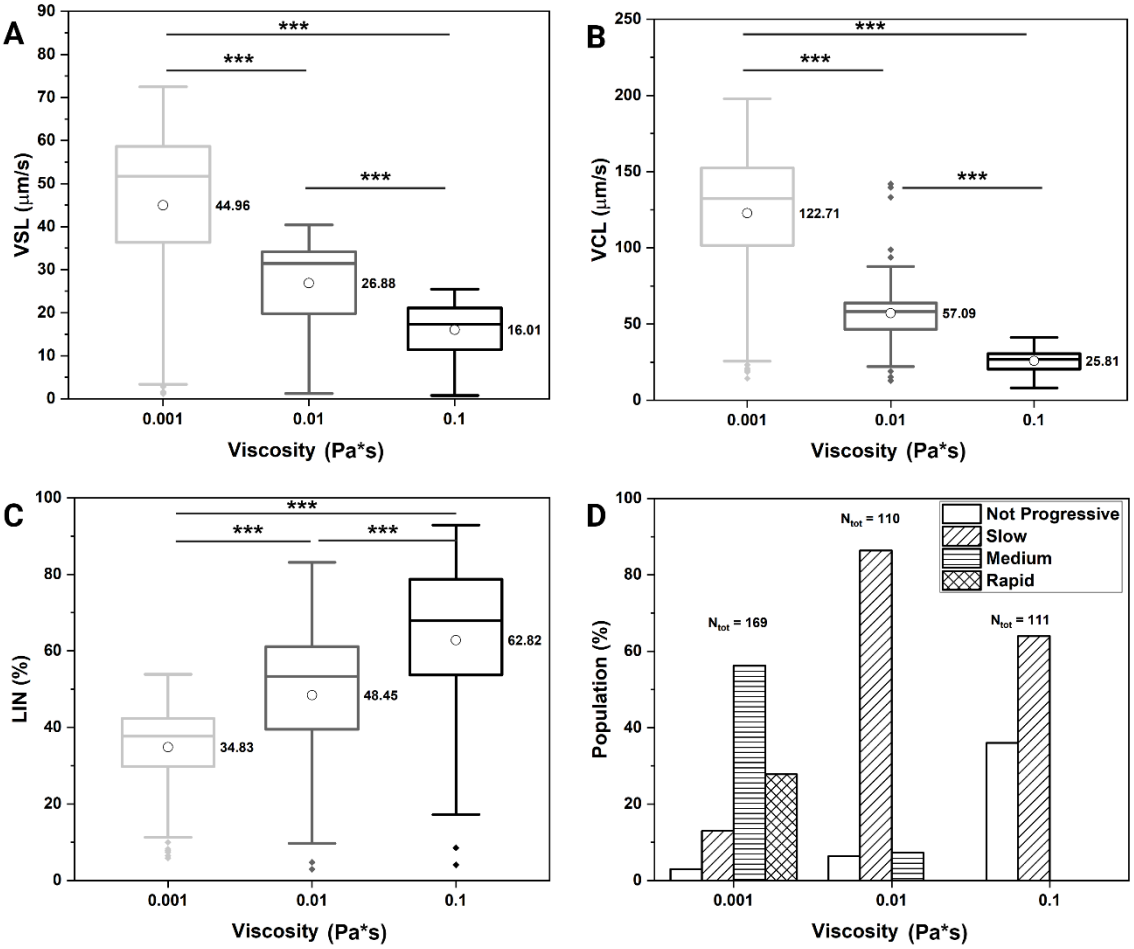

Figure 14. Influence of viscosity on bovine sperm motility in unconfined conditions (200µm). A) VSL. **B)** VCL. **C)** LIN. The values are shown as box charts displaying standard deviations, average values indicated by the white dots and specified by the number in bold, and median values represented by the horizontal lines inside the box. $N_{0.001} = 169$, $N_{0.01} = 110$, $N_{0.1} = 111$. p-value < 0.001 for all the conditions compared among them. **D)** Classification of motile bovine sperm based on VCL in: Not Progressive, Slow, Medium and Rapid according to the ranges in Table 3. The amount of sperm classified is the same of the other plots and are reported on top of the bar plots. The amount of sperm falling in each sub-class is represented here as percentages.

The same trend, in terms of VSL and VCL, was observed also for the sperm loaded in the 200µm glass capillary for the three tested conditions (Figure 14A and B). The only difference is in the average values which for the unconfined conditions are higher than those assumed by sperm in confined conditions. This is true for the three

rheological conditions. The percentages of decrease of both VSL and VCL between viscosities resemble the one observed for the confined geometry leading to the same consideration about the influence of fluid viscosity on bovine sperm motility parameters. Regarding LIN, it is possible to observe an increasing trend with viscosity rise caused by a larger impact of viscosity on VCL rather than VSL (Figure 14C). Therefore, improved progressivity is achieved also in unconfined conditions.

However, a distinction is noteworthy. In unconfined conditions, we observe a decrease in VSL of 40.2% at $0.01\ Pa \cdot s$ and 64.4% at $0.1\ Pa \cdot s$ (Figure 14A), while the VCL reduced of 53.5% and 79% at the same intermediate and high viscosities (Figure 14B).

In both geometries, LIN increases, but VSL declines more significantly in confined conditions, while VCL more in unconfined conditions. This could be explained by considering that the presence of walls in confined conditions can significantly impact the motility of sperm. As they swim forward, there is a greater likelihood of them colliding with the boundaries, resulting in reduced LIN. The VCL-based classification was performed also for unconfined sperm and the trend observed before are very similar (Figure 14D).

In conclusion, the rise in viscosity significantly impacts sperm velocities more strongly than simple geometric confinement does. This effect might be referred to the potentially increased resistance offered by the fluid, while geometric confinement only confines them within a restricted space. However, both influence sperm curvilinear motion, potentially altering their native 3D pattern.

2.2.4. Evaluation and investigation of sperm rolling component and its modulation by viscosity.

During their swimming, sperm were observed to rotate around their motion axis describing a complete 360° revolution [27,28]. We observed and quantified this rotational component by means of phase contrast acquisitions, focusing on the head. As discussed in 2.2.1, during sperm swimming, certain periodic characteristics become evident during rotations along their swimming axis. Specifically, within the plane of acquisition, two predominant features emerge, which we termed the 'Face-on' and 'Rim-on' configurations (Figure 15A). We established a laboratory-fixed coordinate system (x-y-z) as our frame of reference for acquisitions. In Figure 15A, the depicted sperm moves and rotates predominantly in the x-direction within the x-y plane. In its 'Face-on' configuration, the cell appears black; conversely, in the 'Rim-on' configuration, it appears bright. By counting the occurrences of the brighter head in phase contrast recordings, we were able to evaluate the rolling frequency (s^{-1}) across varied conditions [62]. For clarity, we set a standard: when a sperm transits from 'Face-on' to 'Rim-on', it describes a 90° rotation. Accordingly, we attribute a 90° angle to the 'Face-on' and 0° to the 'Rim-on' configurations. These angles are defined relative to the body-fixed frame (x'-y'-z'), centered at the sperm head (Figure 15B). Given that sperm rotate around their progression axis and can be approximated by an ellipsoid shape, we employed the ellipsoidal model to analyze the rolling motion of the sperm head [118]. Within this body-fixed frame, we defined three primary dimensions: ${\delta_{xy}}^{x}$, ${\delta_{xy}}^{y}$, and ${\delta_{xz}}^{z}$. Here, the pedicles denote the plane within the x'-y'-z' system where a specific dimension is observable, while the apices represent the axis along which that dimension aligns (Figure 15B). Importantly, these dimensions -

corresponding to head length, width, and thickness- were extracted from the morphological analysis, as detailed in section 2.2.1.

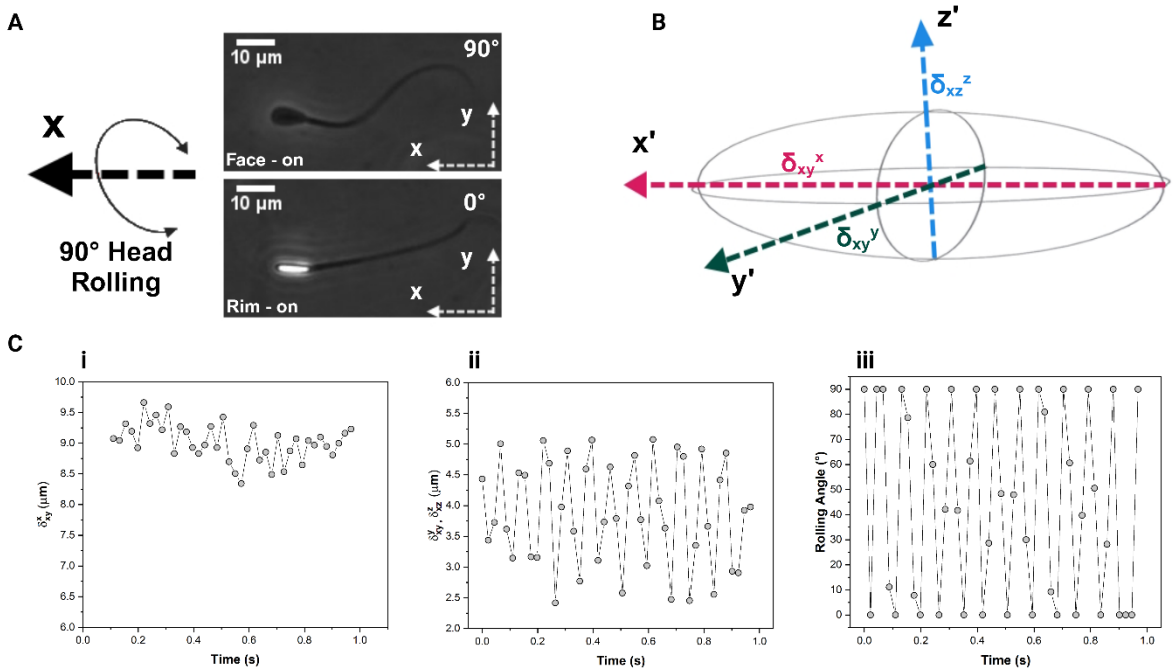

Figure 15. Bovine sperm rolling motion. A) Real images of a bovine sperm captured in the two configurations it assumes in a 20x – phase contrast acquisition: Face-on and Rim-on. The rolling motion occurs around the propulsion axis (represented by the black arrow on the left). The transition between Face-on and Rim-on is linked to a 90° rotation of the head, where angles of 90° and 0° correspond to the two respective configurations. The white arrows in both images indicate the laboratory-fixed coordinate system corresponding with the plane of acquisition. **B)** Ellipsoidal head model indicating the main dimension of a bovine sperm head ($\delta_{xy}{}^{x}$, $\delta_{xy}{}^{y}$, $\delta_{xz}{}^{z}$). The three axes indicate the three planes of the body-fixed coordinate system (x'-y'-z'). The pedicles indicate the plane where a specific dimension is observable, while the apices represent the axis along which that dimension aligns. **C)** Example of the manual tracking of a single bovine sperm head in a 1s phase contrast acquisition at CTRL in confined condition. (i) indicates the $\delta_{xy}{}^{x}$ which corresponds to the sperm head length, (ii) indicates $\delta_{xy}{}^{y}$ and $\delta_{xz}{}^{z}$ which correspond to the sperm head width and thickness, respectively and (iii) indicates the rolling angle oscillation along time obtained by cubic spline interpolation. This cell is used here as an example of the procedure.

By manually tracking the head for 1s, frame by frame we evaluated the three dimensions and how they change along time (Figure 15C). The time elapsed between two consecutive frames is of about 0.02s owing to the employed FR of 45 fps. The results show that $\delta_{xy}{}^{x}$, is quite constant during time since it is exposed by sperm in both Face-on and Rim-on configuration (Figure 15C i). On the other hand, instead $\delta_{xy}{}^{y}$, and $\delta_{xz}{}^{z}$ oscillate during time between a maximum, (representing the width of the sperm head) and a minimum (indicative of the head thickness) (see 2.2.1). This oscillation is a clear observation of the rolling motion of sperm showing the alternation of Face-on configuration ($\delta_{xy}{}^{y}$ lies in the plane of acquisitions) and Rim-on configuration ($\delta_{xz}{}^{z}$

lies in the plane of acquisition) (Figure 15C ii). The data reported here refer to a single swimming in the 20 µm chamber at CTRL and it was taken as an example. Starting from this oscillation we assigned to the local maxima and minima of $\delta_{xy}{}^{y}$, and $\delta_{xz}{}^{z}$ an angle of 90° and 0°, respectively. Since sperm head has been tracked frame by frame, there are some intermediate points in which sperm does not perform a complete 90° rotation, but an intermediate rotation of an angle comprised between 0° and 90°. To evaluate the rotation angle at these specific points, we performed a cubic spline interpolation over the rolling angle and obtained the missing points (Figure 15C iii) [118]. The complete rolling angle variation is then used to determine the angular rolling velocity (rad/s). Regarding the rolling sperm we were able to also measure a rolling frequency (s^{-1}) by counting the occurrence of the bright light intensity of the sperm heads in phase contrast microscope acquisitions (Figure 15A).

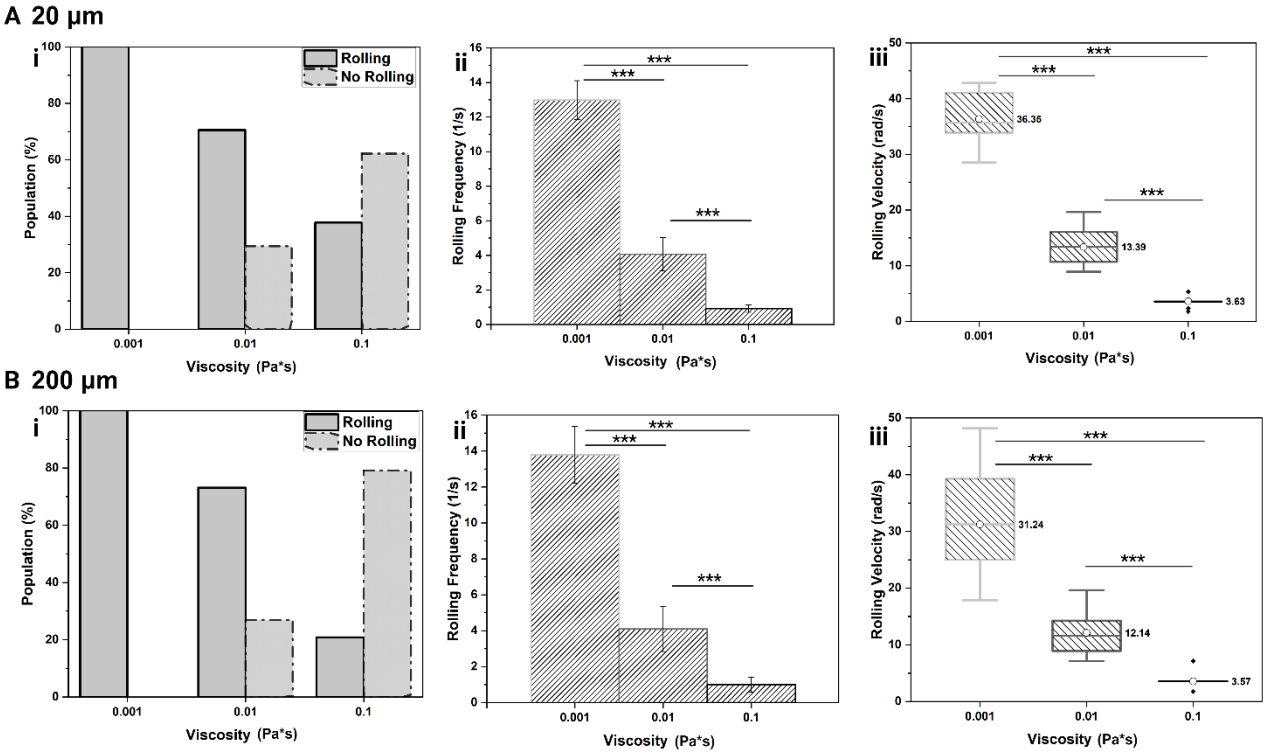

Figure 16. Influence of viscosity and geometric confinement on bovine sperm rolling motion. A) Confined condition (20µm). **B)** Unconfined condition (200µm). (i) Percentage of rolling and no rolling sperm at varying viscosity expressed as percentages. $N_{0.001}^{20\mu m} = 65$, $N_{0.01}^{20\mu m} = 51$, $N_{0.01}^{20\mu m} = 45$. $N_{0.001}^{200\mu m} = 70$, $N_{0.01}^{200\mu m} = 93$, $N_{0.1}^{200\mu m} = 192$. (ii) Rolling frequency (s^{-1}) of manually tracked rolling sperm at varying viscosity. Data are shown as bar plot indicating the average value and the relative standard deviation. For each condition of viscosity and for both geometries the total number of tracked cells were 10. The differences are statistically significant among all the analyzed conditions (p-value < 0.001). (iii) Angular rolling velocity (rad/s) of manually tracked rolling sperm at varying viscosity. The values are shown as box charts displaying standard deviations, average values indicated by the white dots and specified by the number in bold, and median values represented by the horizontal lines inside the box. For each condition of viscosity and for both

geometries the total number of tracked cells is 10. The differences are statistically significant among all the analyzed conditions (p-value < 0.001).

We evaluated the amount of rolling and no rolling sperm in our experiments when they were placed in different rheological conditions to understand how viscosity influences the motion pattern of sperm, rather than simply their velocity. Indeed, we manually counted in the 5s phase contrast acquisitions the number of rolling sperm, which describes linear, progressive trajectories and the no rolling ones which, instead, describe circular, not progressive trajectories. The results show that, in both geometries (Figure 16A i and Figure 16B i), a gradual decrease of the percentage of rolling sperm occurs along with an increase of the percentage of no rolling ones. The percentages exhibit a gradual shift as viscosity changes. At CTRL, all counted cells exhibit a rolling motion, representing 100%. However, this percentage decreases to approximately 70% at intermediate viscosities for both chambers. In high-viscosity settings, the percentages further drop to about 40% for confined conditions and 20% for unconfined ones. Conversely, the proportion of cells not exhibiting rolling motion rises from 0% at CTRL to roughly 30% at intermediate viscosity. In high-viscosity scenarios, this no rolling percentage climbs notably, reaching about 60% for confined conditions and approximately 80% for unconfined ones. It is evident a gradual decrease (increase) of the rolling (no rolling) sperm at intermediate viscosity which instead peaks at higher viscosity. The change in the motion behavior could be associated to the higher resistance offered by fluid viscosity. Highly motile sperm probably manage to navigate through the fluid drag, maintaining their rolling motion. However, potentially less motile or defective sperm fail to overcome this increased resistance. Consequently, their movement becomes planar, lacking any rolling component.

The frequencies follow the same trend observed for both VSL and VCL (Figure 13 and Figure 14 A and B). Indeed, they are strongly affected by fluid viscosity as they gradually decrease at intermediate and high viscous fluid with respect to CTRL (Figure 16 A ii and Figure 16B ii). It is worth noting that the rolling frequencies in both geometries are identical for a fixed viscosity. Additionally, we also noted that rolling occurs rapidly, but discontinuously such that the time between two consecutive rolling is not always constant, as already observed in literature [27], [62]. Therefore, rolling frequency of sperm heads could serve as an additional parameter for fertility diagnostics. Of note, among the 10 manually tracked rolling sperm at CTRL in confined conditions, 8 cells are classified as Medium, while the remaining 2 as Rapid. In particular, the Rapid sperm demonstrate a higher average rolling frequency, approximately $14\ s^{-1}$, compared to the medium ones, which exhibit an average frequency of around $13\ s^{-1}$. This observation aligns with existing literature, suggesting a proportional correlation between rolling frequency and sperm velocity [119]. Furthermore, we assessed an introduced an innovative parameter: the angular rolling velocity. It was assessed after determining the rolling angle frame-by-frame through interpolation. We computed the angular variation ($\Delta\theta$) (eqn. 7) and divided it by the corresponding time interval (Δt) (eqn. 8). By averaging this computed rolling velocity across all sperm under a given condition, we derived the average angular rolling velocity (eqn. 9).

$$\Delta\theta = \theta(frame_{i+1}) - \theta(frame_i) \quad (7)$$

$$\Delta t = t(frame_{i+1}) - t(frame_i) = 20\ msec \tag{8}$$

$$\hat{\Omega}_{rolling} = \left\langle \frac{\Delta\theta}{\Delta t} \right\rangle \tag{9}$$

where $frame_{i+1}$ and $frame_i$ indicate consecutive frames of the acquisitions. The findings show a significant influence of fluid viscosity on the angular rolling velocity. Specifically, as viscosity increases, the angular rolling velocity decreases progressively in both geometric confinements. This implies that sperm in environments with intermediate and high viscosity not only exhibit less frequent rolling but also roll at a reduced speed compared to CTRL, i.e. the time taken for a sperm to describe a complete 90° rotation is much longer. This clearly reflects on the shape of the rolling angle curves: at CTRL, the curves exhibit rapid fluctuations with a saw-tooth pattern (Figure 17A), whereas at intermediate and high viscosities, the curves adopt a more sinusoidal form, marked by slower oscillations (Figure 17B and C respectively). At CTRL, we observe abrupt changes in the angle, suggesting frequent and rapid rolling. However, at intermediate and high viscosities, these angular shifts become more gradual, indicative of reduced frequency and slower rolling. To better clarify, when consecutive points display no change in angle, it indicates that the sperm remains stationary during that instant of time, seemingly hindered by the elevated viscosity of its surroundings. It is worth noting that the curves presented in Figure 17 represent the behavior of a single cell under each condition as illustrative examples.

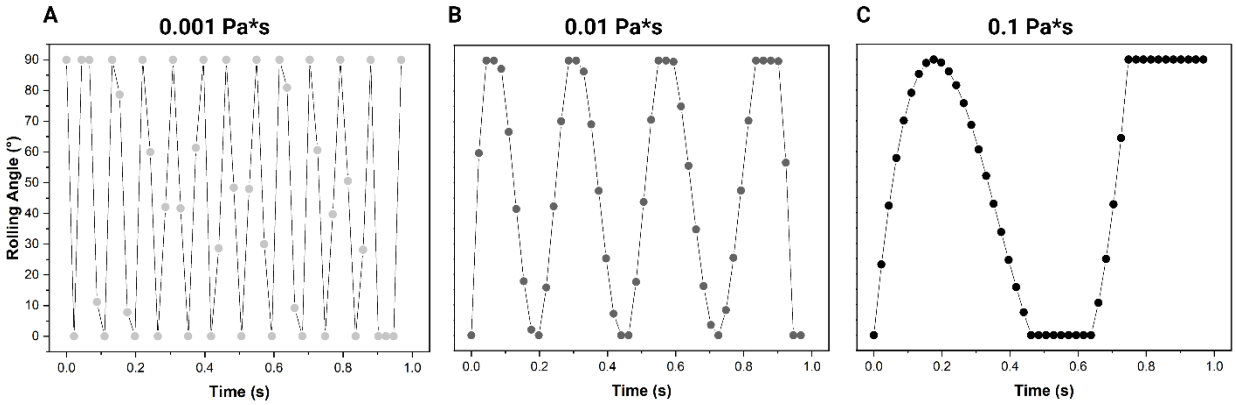

Figure 17. Representative examples of rolling angle oscillations in time for the three viscosities. A) CTRL ($0.001\ Pa \cdot s$ - light grey). **B)** Intermediate viscosity ($0.01\ Pa \cdot s$ – dark grey). **C)** High viscosity ($0.1\ Pa \cdot s$ – black). The tracking was performed on phase contrast acquisitions for 1s. The oscillation at CTRL is faster than at intermediate and high viscosities indicating the slower sperm rolling as viscosity increases.

Integrating angular rolling velocity as an additional parameter alongside existing ones could enhance the investigation of sperm motility, particularly in terms of their 3D motion pattern, a dimension often overlooked in conventional semen analysis. Moreover, considering this parameter and its sensitivity to the viscous environment could provide a more comprehensive analysis of sperm motility.

We have discussed sperm exhibiting rolling motion and progressive linear movement. However, as mentioned earlier, the increase in viscosity leads to a planarization of sperm motion in both analyzed geometries, owing to the increased fluid resistance. We observed that some sperm are incapable of exploiting a rotational-translational motion but instead display an oscillatory movement lacking rolling and occurring in a single plane. This planarization of motion results in a loss of progressiveness for these cells, manifesting in circular trajectories (Figure 18D and E). Consequently, these sperm do not move in a straight line but rather remain in place, rotating around a center of revolution. We have thus evaluated these trajectories and their velocities based on phase-contrast recordings (Figure 18A and B).

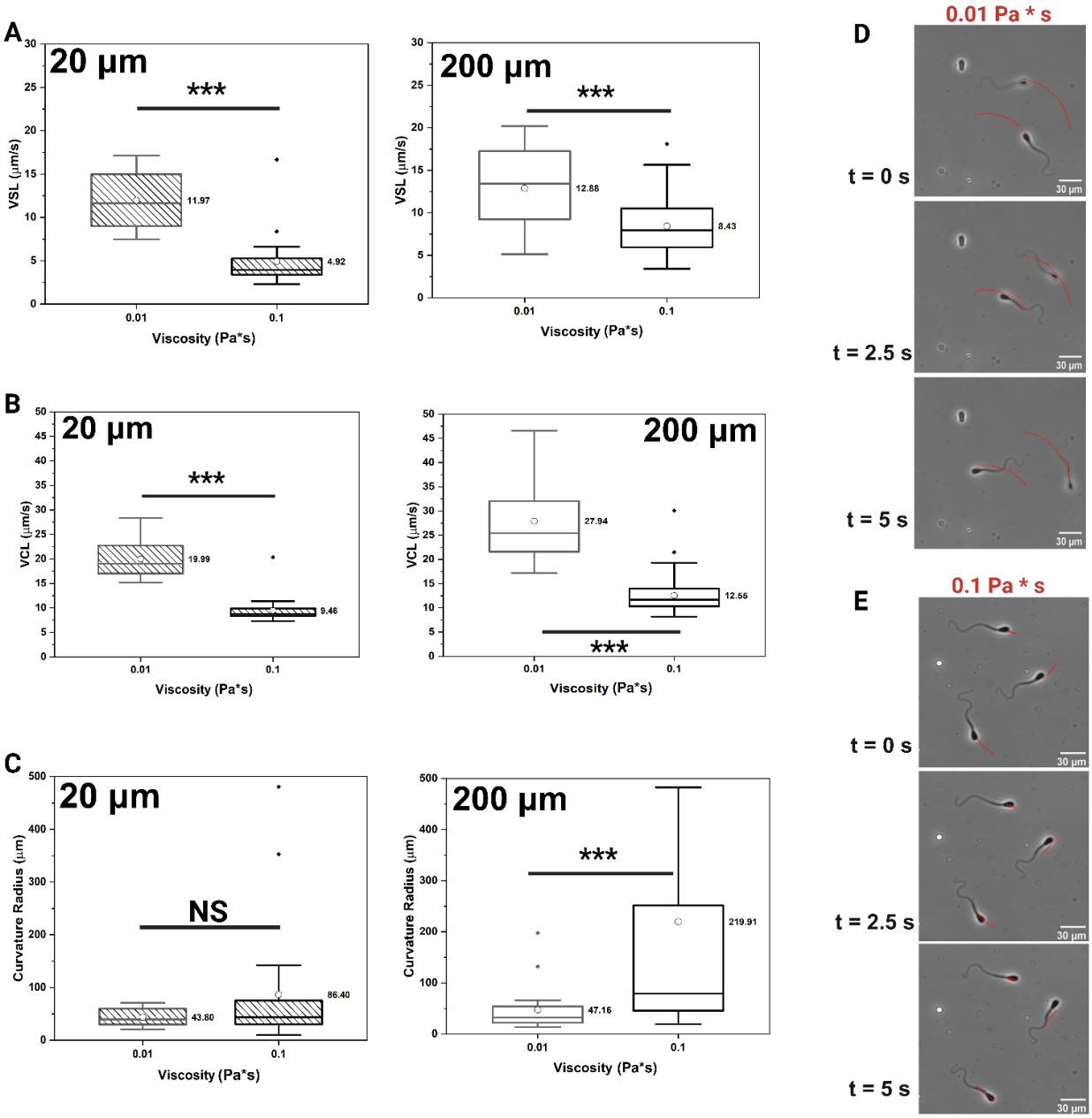

Figure 18. Assessment of no rolling (circular) bovine sperm. A) VSL, **B)** VCL and **C)** Curvature radius. The parameters shown here are those of the no rolling sperm, in both confined (20µm – left) and unconfined (200µm – right) conditions

at varying viscosity. The values are shown as box charts displaying standard deviations, average values indicated by the white dots and specified by the number in bold, and median values represented by the horizontal lines inside the box. $N_{0.01}^{20\mu m} = 13$, $N_{0.1}^{20\mu m} = 21$, $N_{0.01}^{200\mu m} = 21$, $N_{0.1}^{200\mu m} = 77$. The values of almost all parameters in the different conditions are statistically significant (p-value < 0.001). The only exception is the radius of curvature in confined conditions, that when comparing its value at intermediate viscosity with that at high viscosity gives not statistically significant results (p-value > 0.05). **D)** Actual images of no rolling bovine sperm were captured at intermediate viscosity ($0.01\ Pa \cdot s$), using 5s phase-contrast acquisitions. Sperm trajectories are curved (superimposed in red). **E)** Actual images of no rolling bovine sperm were captured at intermediate viscosity ($0.1\ Pa \cdot s$). Here the acquisition time is insufficient to reconstruct a curved trajectory, resulting in the evaluation of straighter and shorter paths (superimposed in red).

Here, we do not present data of no rolling sperm at CTRL because they were completely absent. Like the velocities calculated from 1s brightfield recordings for all analyzed trajectories, we observed a decrease in both VSL and VCL in circular trajectories as well, calculated from the 5s phase contrast recordings, when transitioning from intermediate to high viscosity (Figure 18A and B). Notably, in unconfined conditions, the reduction in VCL is more pronounced when compared to confined conditions, while VSL do the opposite. The duration of 5s seems suitable for the intermediate viscosity condition but not for high viscosity. In the latter, where cells move much slower, a longer observation time is needed to clearly discern a well-defined circular pattern and calculate a reliable curvature radius. This is reflected in the curvature radius values, which increase (Figure 18C) at higher viscosity where sperm are slower and then they are unable to complete a full circle within the acquisition time. Consequently, the trajectory reconstruction is less accurate, resulting in a higher curvature radius, as the path becomes more linear than distinctly curved (Figure 18E).

3. Bovine Sperm swimming in flow conditions.

The integration of microfluidics represents a promising approach for the selection of healthy sperm, overcoming the limitations of conventional methods that often bypass natural barriers within the FRT [52,113,120]. Within this framework, the mechanism of positive rheotaxis (PR) is explicated both as a guiding and selection principle. Indeed, only highly motile and progressive sperm can withstand this flow, while defective and low motile ones are washed away and filtered out. PR allows sperm to reorient against fluid-flow, a phenomenon which has been reproduced in microfluidic devices [53,61,65,121]. By manipulating both viscosity and fluid-flow, microfluidic platforms recreate physiological filtering mechanisms such as the ones of the FRT [110]. This innovative microfluidic approach not only preserves sperm quality but also addresses limitations associated with traditional techniques, providing a more physiologically relevant and effective means for optimal sperm selection in ART.

In this study, we proposed an exploration of the interplay between flow and fluid viscosity on the motility of frozen-thawed bovine sperm. The flow conditions were determined using an in-house fabricated microfluidic device, whose design has been published elsewhere [108]. This device facilitates the observation of PR and the separation of sperm into two distinct chambers – one for collecting rheotactic responsive sperm and another for discarding defective, low-motility, or dead ones. Swimming sperm were captured under various flow conditions with varying volumetric flow rates, and the optimal one for subsequent experiments was determined and employed for experiments at varying viscosities. Like the static conditions, we manually tracked head trajectories in flow to assess parameters related to sperm rolling, including rolling frequency and angular rolling velocity. The quantity of rolling and no rolling cells in various rheological conditions within our microfluidic device was also quantified. We examined how these no rolling, circling sperm responded to the flow, presenting an alternative selection approach based on different in-flow motion dynamics.

3.1. Materials and Methods.

The reagents and media employed in the microfluidics experiments were consistent with those used in static conditions. Specifically, we employed Sydney Gamete buffer for sample preparation following the protocol described in 2.1.2 (Figure 19B). Two solutions of PVP (360kDa) at concentrations of 2wt% and 5wt% (intermediate and high viscosity, respectively) were prepared, with their viscosity measurements depicted in Figure 9. Additionally, PBS was used as the low viscosity medium in the microfluidic device. After sample preparation, bovine sperm were diluted to a concentration of $3 \cdot 10^6$ sperm/ml in gamete buffer. For each experiment, 4µl of this solution was loaded into the microfluidic device. Before each microfluidic experiment, we performed a control condition in Gamete buffer which will be referred to as CTRL. Acquisitions were conducted within the microfluidic device (Figure 19C) using our optical setup (Figure 19B) in both brightfield and phase contrast at 20x magnification and 45fps. The data were analyzed using our MATLAB routine to determine trajectories and calculate motility parameters (VSL, VCL, and LIN) (see Appendix A for details about motility parameters computation). In addition to the classical motility parameters, we also evaluated

sperm angular displacement (AD) which is calculated as the inclination of the whole trajectory with the horizontal direction. This parameter was employed to have additional insight into the directionality of sperm in flow conditions. The video duration in this case was set to 3 or 5s, for both brightfield and phase contrast acquisitions since 1s duration proved insufficient for observing the directionality of sperm in flow while studying their rheotactic behavior. Once again, VCL was used to classify flowing sperm into sub-classes based on the ranges reported in Table 3 (Not Progressive, Slow Medium, and Rapid). Manual analysis, as described in 2.1.4, was carried out for phase-contrast video analysis to determine the rolling parameters under the different examined viscosities. Statistical analysis was performed using the Kruskal-Wallis test, following the criteria outlined in 2.1.5.

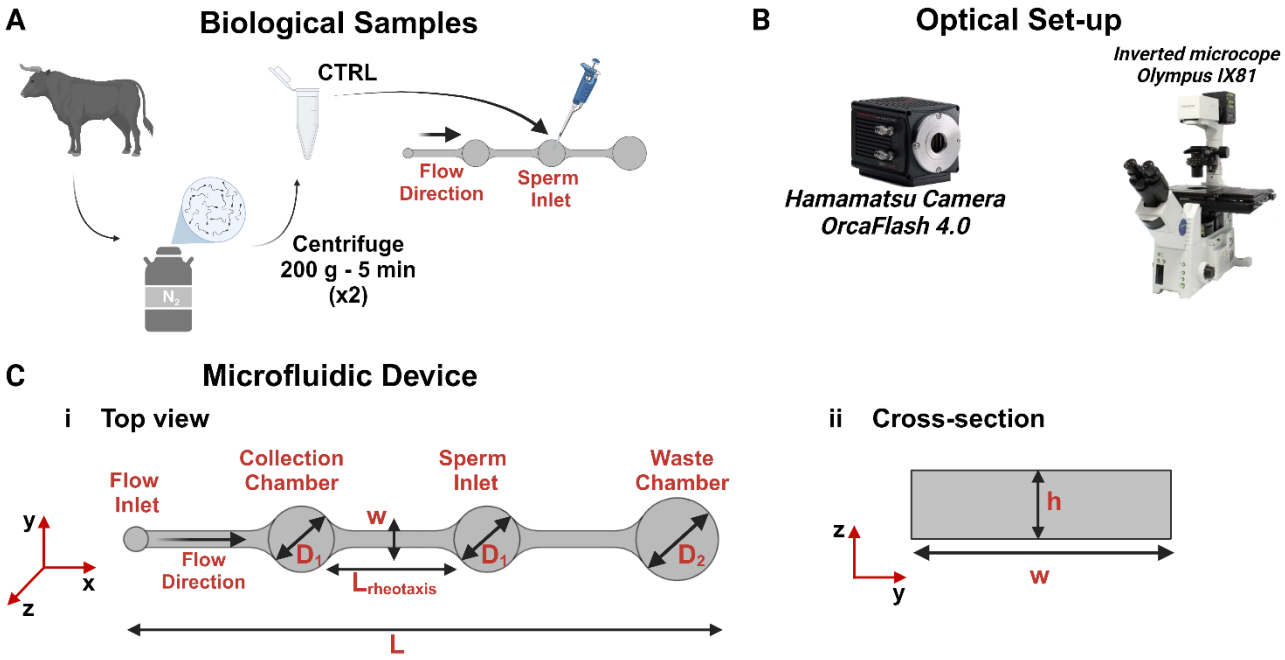

Figure 19. Bovine sperm analysis in flow conditions. A) Cryopreserved bovine sperm were employed in the analysis and washed two times by centrifuge, before being diluted at the desired concentration at CTRL. 4µl of sperm sample ($3 \cdot 10^6$ sperm/ml) was then loaded in the microfluidic device. **B)** Optical set-up employed in the analysis. An inverted microscope and a rapid CMOS camera were employed for both brightfield and phase contrast acquisitions at 45 fps. **C)** In-house produced microfluidic device, whose design had been earlier proposed [108]. i) Schematic representation of the top view of the microfluidic device (as seen from the microscope acquisitions) showing flow inlet, sperm inlet chamber for sperm loading, collection chamber for rheotactic sperm retrieval and waste chamber for the collection of dead, defective and low motile sperm. ii) Microfluidic device rectangular cross-section indicating a large aspect ratio. The image shows the relative dimensions which are summarized in Table 5.

3.1.1. Microfluidic Device.

The microfluidic device design incorporates three primary chambers interconnected by microfluidic channels. Positioned at the center is the sperm inlet chamber, facilitating the loading of sperm into the device. On the

right, there is a waste chamber designed to the collection of defective and low motile sperm that were unable to counteract the applied flow and undergo PR. Conversely, on the left, a collection chamber serves to accumulate motile sperm that, guided by rheotaxis, traverse from the sperm inlet to the collection chamber (Figure 19C). The basic idea was to apply a fluid-flow, in the direction indicated by the black arrow, load an heterogenous sperm sample inside the sperm inlet chamber and separate sperm, based on their motility. Indeed, sperm capable of exhibit PR move in the opposite direction of the flow, towards the collection chamber, while the others are instead washed away by the applied flow, moving in the flow direction towards the waste chamber. A schematic representation of the device top-view, as seen during the experiments, is shown in Figure 19Ci. The main dimensions of the device are its total length L = 3.6cm, its width w = 1mm, the diameter D_1 = 4mm of both the collection and sperm inlet chambers, the diameter D_2 = 5mm of the waste chamber and the length of the microfluidic channel in which PR occurs, named $L_{rheotaxis}$ = 5mm. The cross-section of the device, instead, shows the overall depth of the channels h = 0.1mm offering a very high aspect ratio, meaning the ratio of channel width and depth, AR = 10 (Figure 19Cii). This provides the capability to generate a fluid-flow with a constant velocity profile along the y-direction, resembling plug flow. Simultaneously, in the z-direction, the flow exhibits a parabolic Poiseuille profile, with the walls exerting a more pronounced influence on the flow dynamics (see CFD simulations for details 3.2.1). The device geometric dimensions are summarized in Table 5.

Table 5. Characteristic dimensions of the microfluidic device geometry.

Dimension	
Length (L)	3.6 cm
Width (w)	1 mm
Inlet/Collection chamber diameter (D_1)	4 mm
Waste chamber diameter (D_2)	5 mm
Rheotaxis length ($L_{rheotaxis}$)	5 mm
Depth (h)	0.1 mm

3.1.2. Microfluidic device fabrication.

For the device fabrication, PDMS was employed owing to the simplicity of molding it in various shapes along with its inherent properties (transparency and biocompatibility) which led to the spreading of its employment in microfluidics applications in diverse and important biological fields and clinical studies [122]. PDMS (SYLGARD™ 184 Silicone Elastomer, Dow), starts as a liquid and can be solidified with the addition of a cross-linking agent giving the possibility to reproduce any type of design. The technique employed for the fabrication of the microfluidic device is the so-called replica molding which consists in the production of a 3D master onto which a layer of liquid PDMS is poured and cured by temperature. The cured PDMS is then peeled off the master and a replica of the pattern present onto the mold is produced. The master was fabricated using

micro-milling. This technique is a subtractive manufacturing process which consists in the removal of the material from a sheet of PMMA. This material is a transparent and very rigid polymer which can be carved by means of the micro-milling machine (Minitech Machinery Corp.) (Figure 20A). Therefore, first, we proceeded with the design of the desired microfluidic structure which was created in the CAD software Fusion 360® (Autodesk, Inc.), and an .dxf file was created. Then we implemented on DESKAM (Carken Co.), a .cnc file developer, the files for the machine, to give it the right processing steps. These steps were optimized during the fabrication to obtain the most precise product possible. By doing so a good mold was obtained in more or less than 1h and a half. Therefore, we created a negative of the microfluidic channel onto the PMMA sheet protruding upwards of 100µm. At this point, after a careful cleaning process with deionized water and by brushing the mold to remove excess of plastic from the fabrication, we proceeded with the replica molding process. A 10:1 solution of PDMS and cross-linking agent was prepared by vigorous mixing to achieve a homogenous distribution of cross-linker and then degassed for 1h to remove all the air bubbles. Degassing the PDMS solution is very important to avoid the formation of air bubbles inside the final microfluidic device during curing. A layer of 3mm of PDMS was then poured onto the mold and put in the oven at a temperature of 80°C for 2h for the curing process (Figure 20B). The solidified PDMS layer was peeled off, cleaned, and observed at the microscope for quality checking (Figure 20C). The so obtained PDMS was then punched with biopsy punches to create the holes, for the fluidic connection (1.5mm ∅) and the chambers (Figure 20D). The so obtained replica was then bonded to a glass slide to obtain the final microfluidic device. The bonding was performed by means of oxygen plasma treatment, which consists in the exposure of both the PDMS and the glass slide to oxygen (O_2) plasma at a power of 50W for 60s (CESAR® RF power generator, Advanced Energy Industries, Inc.). The PDMS was then, gently pressed onto the glass slide to complete the bonding process (Figure 20E). Immediately after bonding, while the plasma treatment was still active, we internally treated the microfluidic device with a polymeric solution of Poly(L-lysine)-grafted-Poly(ethylene glycol) (PLL-g-PEG) (SuSoS, Dübendorf, Switzerland) to minimize the adhesion of sperm to the device walls and optimize the selection process. This type of treatment has proven effective in preventing the adhesion of both sperm and other cells, as well as avoiding biofouling [123]. The process involves the electrostatic binding of the NH_3^+ groups of PLL to the negatively charged oxidized surface of PDMS. This oxidation occurs when the PDMS is treated with oxygen plasma, rendering the surface negatively charged when placed in an aqueous solution. By exposing the PEG side chains in the bulk of the liquid, this creates a more hydrophilic coating on the PDMS surface, thereby preventing sperm attachment [124,125] (Figure 20D). The coating procedure began by dissolving polymers in an aqueous buffer solution with a concentration of 0.1mg/ml. Subsequently, the O2-treated PDMS microfluidic device was filled with this solution and allowed to rest at room temperature for 1h in a humidified environment to prevent fluid evaporation. Following this, the device was flushed several times with PBS to eliminate excess polymer and was then dried using compressed air. To maintain the integrity of the PLL-g-PEG layer, the device was stored at 4°C and brought at room temperature prior to the experiments. At this point, a cylindrical tube was attached to the fluid inlet with biphasic glue (picodent twinsil, picodent®) and the device was ready for testing (Figure 20E).

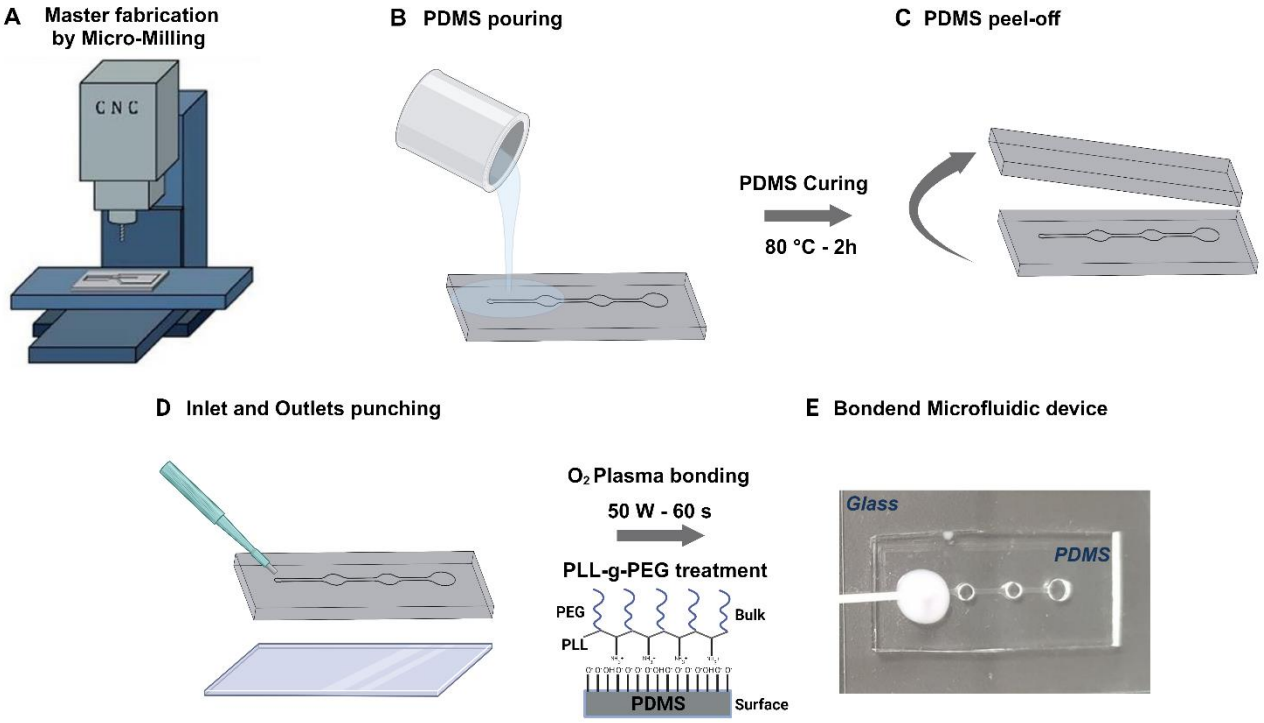

Figure 20. Microfluidic device fabrication process. A) Master microfabrication by means of micro-milling machine. **B)** PDMS poring for master replication. **C)** Peel-off of the cured PDMS replica. **D)** Inlet and Outlet opening by biopsy punches. **E)** Oxygen-bonded PDMS microfluidic device after surface coating by PLL-g-PEG and tubing attachment.

3.1.3. Computational Fluid Dynamics (CFD) simulations.

3D computational fluid dynamics (CFD) simulations were conducted by means of COMSOL Multiphysics® 5.3a (COMSOL INC.) to determine flow conditions within the microfluidic device. Applying laminar and steady state flow conditions, we solved with COMSOL the classical Navier-Stokes equations for an incompressible fluid with no-slip condition at the wall. The simulations were performed for a single volumetric flow rate (11.04µl/h) applied at the inlet of the device in the condition of low viscosity medium (PBS). Therefore, fluid properties were the one of water, so a viscosity of $0.001\ Pa \cdot s$ and a density of $1000\ Kg/m^3$. We applied fully developed flow condition at the fluid inlet, while the fluid outlet, designated as the waste chamber (Figure 19C), was set to atmospheric pressure. The decision to use the waste chamber as outlet was since it was open for all the experiment duration. In contrast, the collection and sperm inlet chambers were sealed with 3D-printed caps to prevent any fluid loss throughout the experiments. Some 3D cut lines and cut planes were defined in the device geometry to better observe specific features in the results.

3.1.4. Experimental approach.

The microfluidic device was connected to a pressure-controlled pump (Mitos P-Pumps, Dolomite Microfluidics) through a capillary tube. The applied pressure was adjusted to each examined flow condition and fluid viscosity, to obtain of the desired volumetric flow rate. To validate the functionality of the device before experimenting it with bovine sperm, a preliminary test was conducted using polystyrene (PS) microparticles (Polyscience Inc.). These particles, having a diameter of 3µm and a density of $1.05\ g/cm^3$, were introduced into the device along with low viscosity medium. The density of the PS microparticles is very close to fluid one reducing their sedimentation during the experiment. To ensuring a comparison, the flow rate used for microparticle validation was aligned with the one employed in the simulation. This approach aimed to establish a reliable baseline for experiments and analyses. With the aim to optimize PR of sperm, the volumetric flow rate was systematically adjusted. Specifically, the focus was initially on the low viscosity medium, determining the optimal flow rate for sperm PR and subsequent collection. It was varied from a minimum of 11.04µl/h to a maximum 16.6µl/h. After biological calibration of the device, the optimal flow rate (11.04µl/h) was applied for further investigations into different viscosities (intermediate and high viscosity). The biological experiments were conducted by filling the microfluidic device with one of the selected fluids, by keeping the collection and sperm inlet chambers sealed with 3D printed caps. Following filling, the sperm inlet was opened, and 4µl of sperm sample at a concentration of $3 \cdot 10^6$ sperm/ml was loaded inside the device, with consequent closure of the sperm inlet chamber (Figure 19C). To verify the proper flow within the device, an initial observation was conducted on the right side of the sperm inlet chamber, directed towards the waste chamber. Subsequently, sperm were visualized within the rheotaxis channel, demonstrating movement from the sperm inlet to the collection chamber. After about 15 min, sperm were then collected from the waste and collection chambers for further motility analyses.

3.2. Results and Discussion

3.2.1. Microfluidic validation

COMSOL® simulations were performed to evaluate the fluid dynamics of our microfluidic device as described in 3.1.3. The 3D geometry was imported from Fusion 360® and fluid inlet and outlet were selected (Figure 21A). The results, in terms of velocity magnitude, have been evaluated in a x-y cut-plane defined at the center of the device (z = 0.05mm) (Figure 21B). Here, we observe that the fluid velocity remains the same in the three channels connecting the chambers. This is attributed to the sealing of the two central chambers, as modeled in COMSOL® by imposing a wall condition and preventing any fluid loss. The waste chamber on the right was intentionally left open and designated as the flow output. The high AR of the device contributes to a plug-like velocity profile in the x-y plane, ensuring uniform velocity along the y direction. However, in this cut-plane, we visualize the maximum velocity since it is defined at the center in the z direction. This occurs because along the z-axis, a parabolic velocity profile is established due to the smaller dimension (Figure 21C). Examining

the velocity magnitude in the z-y plane, defined at the central x of the rheotaxis region, reveals that velocity is minimal at the walls, gradually increasing towards the center and reaching a maximum at z = 0.05mm. Additionally, the high aspect ratio minimizes the influence of lateral walls on the velocity profile. At a fixed z, the velocity remains constant along y, except for positions closer to the wall where the no-slip boundary condition induces a reduction in fluid velocity. We observe that the velocity magnitude within the three chambers remains low, primarily due to their larger dimensions compared to the channels. Notably, the channel on the right of the central sperm inlet chamber serves a dual purpose. Its design not only facilitates the removal of defective and low motile cells, directing them to the waste chamber, but also as an outlet for the fluid-flow originating from the sperm inlet chamber. Indeed, in previous produced devices, the absence of the waste chamber and its connecting channel limited the ability to induce sperm rheotaxis. In those cases, the sperm inlet, characterized by very low flow velocity, acted as a stagnant point where sperm were not influenced by fluid-flow and failed to exhibit their rheotactic behavior. The introduction of the connecting channel between the sperm inlet and waste chambers has resolved this limitation, promoting a continuous flow. Now, sperm can sense the flow and effectively reorient against it, showing their rheotactic behavior. A device validation was performed to verify that the simulated flow conditions are respected by microparticle experiments. In details, we flushed, within the microfluidic device, a suspension of PS microparticles in low viscosity medium by means of a pressure-controlled pump and evaluated their velocity. Here we performed acquisitions of particles in the portion of the channel that we denoted as rheotaxis region between the collection and the sperm inlet chambers. The acquisitions were performed by means of our optical set-up (Figure 19B) in phase contrast, 20x magnification and 45fps. Three recordings of 5s were performed to ensure a sufficiently high number of microparticles in the field of view.

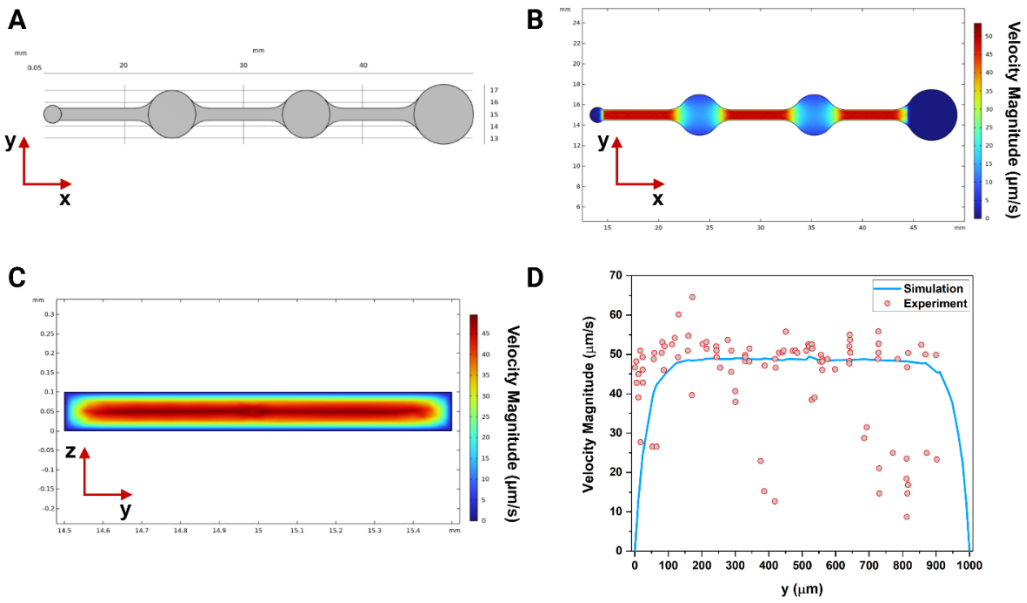

Figure 21. Computational fluid dynamics simulations. A) 3D geometry employed for the simulation showed in its top view (x-y plane). **B)** Fluid velocity magnitude evaluated at the central z (x-y plane) showing the maximum velocity and indicating a plug-like flow with constant magnitude along y direction. **C)** Fluid velocity magnitude evaluated at a y-z cut-plane showing a parabolic velocity profile along the z direction and a plug-like flow along the y direction. **D)** Comparison of the simulated velocity magnitude with the experimentally determined one. The azure line graph shows the simulated values along a y oriented cut-line at central z in cross-section. The red dots indicate the experimentally determined velocity values from 3µm polystyrene particles tracking ($N_{particles} = 101$).

Microparticles velocities were evaluated by means of a self-written MATLAB® routine which detects the particles along the recording and tracks them in the field of view, therefore determining their velocity. Particles here were not aligned along a specific streamline but were homogenously distributed throughout the width of the microfluidic device (x-y plane in Figure 21), owing to the Newtonian behavior of the fluid, lacking viscoelasticity and therefore not capable of aligning microparticles. Despite this, our attention was directed to the plane (in the z direction) where the particles were the fastest. This approach ensured the assessment of maximum fluid velocity, assuming that microparticle velocities were identical to those of the fluid. By adopting this strategy, we aimed to facilitate a comparison between experimental observations and simulated results (Figure 21D). By defining a 3D cut-line at the center of the y-z cut-plane (z = 0.05mm), we evaluated the maximum velocity along the y direction which shows a plug profile with decrease only near the walls (azure line plot in Figure 21D). Superimposed on the line plot, we added a scatter plot showing the velocity of the detected particles (red dot in Figure 21D). Indeed, a notable portion of microparticle velocities closely aligns with the line representing fluid velocity, indicating a good agreement between our simulations and experimental observations. However, a subset of microparticles exhibited lower velocities due to the

identification, by our MATLAB® routine, of particles flowing off-focus in a different z plane. These were detected based on their light intensity recognized by the software. Indeed, by calculating the average microparticles velocity we obtained a value of 44.5µm/s, while the average fluid velocity was 40.7µm/s, leading to an error of about 9.3%.

3.2.2. Sperm rheotaxis behavior

With the aim to validate our microfluidic approach, we first wanted to demonstrate the ability of our device to effectively induce bovine sperm PR. To do so, we performed a first experiment as outlined in 3.1.4 and after loading bovine sperm in the sperm inlet chamber, we observed their movement at the center of the rheotactic region.

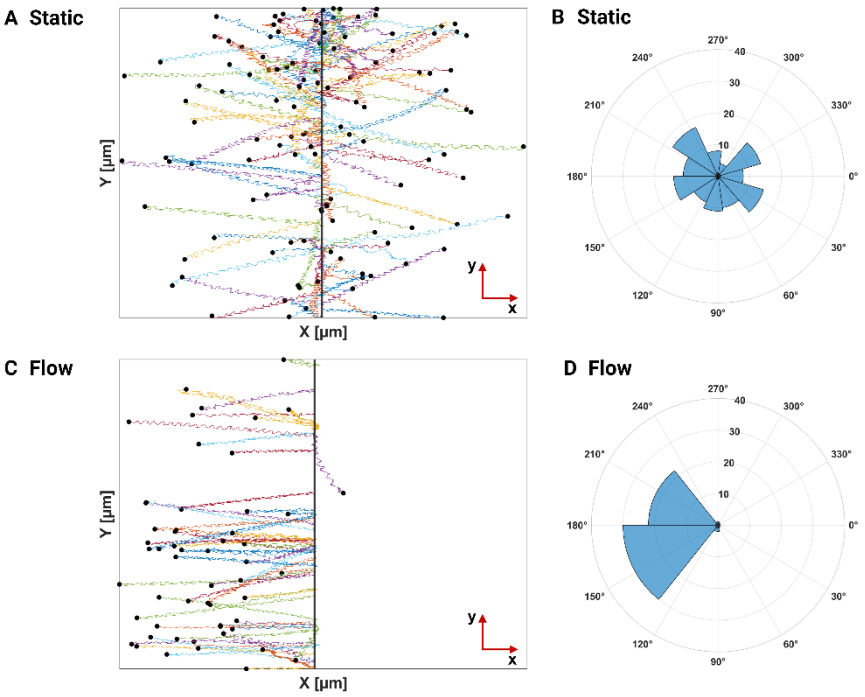

Figure 22. Bovine sperm positive rheotaxis. A-B) Sperm trajectories in static conditions with the relative polar histogram of angular displacement (AD). **C-D)** Sperm trajectories in flow conditions with the relative polar histogram of angular displacement. The flow direction is from left to right. In both figures the vertical line represents the initial point of each trajectory, while the black dot represents the final point. In the polar histogram the radial scale denotes the occurrence in a specific direction, while the circular scale represents the angles covered by sperm trajectories. The number of bins in the histograms were calculated as the root square of the sample numerosity in each experiment. $N_{NoFlow} = 122$, $N_{Flow} = 55$.

The fluid employed was PBS and the applied flow rate 11.04µl/h determining an average fluid velocity of about 41µm/s. A CTRL condition was performed in a 20µm counting chamber to compare the results. The resulting trajectories were plotted to have indications about the rheotactic ability of bovine sperm. For a better representation, all trajectories were shifted along the x-axis in the microscope x-y plane to enhance their directional visibility (Figure 22A and C). The positive x-direction in this set-up corresponds to the flow

direction, and the sperm trajectories start at the vertical black line, arriving to their endpoint denoted by a black dot. We can observe that there is clear difference between static conditions, at CTRL in the 20µm chamber, and flow conditions in the microfluidic device, for the same fluid viscosity. Indeed, in static conditions bovine sperm trajectories are randomly oriented without any preferential direction of motion (Figure 22A). Each cell moves independently from the others because no acting force is applied. However, when subjected to a flow, sperm exhibit a collective tendency to move in a unified direction, specifically opposite to the flow, along the negative x-direction (Figure 22C). This qualitative observation is reinforced by the quantitative analysis performed in terms of angular displacement (AD) (see 3.1 for definition), representing the trajectory angle relative to the horizontal direction, which corresponds to the one of the flow. The ADs are visualized in polar histograms, illustrating the overall orientation of sperm under both static and flow conditions (Figure 22B and D, respectively). In the histograms, the radial scale denotes the occurrence in a specific direction, while the circular scale represents the angles covered by sperm trajectories. The number of bins in the histograms were calculated as the root square of the sample numerosity in each experiment. Upon examination of the histograms, a notable distinction emerges. Under static conditions, ADs are randomly distributed across the entire 0° to 360° range. However, in the presence of flow, a polarization is evident, with sperm predominantly aligned along the counter-flow direction, falling within the 120° to 140° range. In this context, 180° corresponds to the counter-flow direction, while 0° is associated with the flow direction. Therefore, sperm exhibiting trajectories with ADs oriented to the left side of the histogram are considered rheotactic. This results clearly indicated the ability of our microfluidic approach to induce sperm rheotaxis.

We conceived our experiments to determine the optimal flow rate, aiming not only to enhance the rheotactic response of sperm but also to examine the impact of increased flow on their movement. In our microfluidic experiments, various volumetric flow rates of the low viscosity medium were applied, and we assessed the motility parameters (VSL, VCL and LIN) of bovine sperm under different flow conditions for a comprehensive analysis. The applied flow rate with the corresponding COMSOL® simulated fluid velocities are summarized in Table 6.

Table 6. Experimental determend volumetric flow rate with corresponding simulated fluid velocity.

Volumetric Flow Rate [$\mu l/h$]	Fluid Velocity [$\mu m/s$]
11.04	41 ± 14
12.42	46 ± 16
13.8	51 ± 18
15.2	56 ± 20
16.6	61 ± 22

The acquisitions under flow conditions were conducted in the central part of the rheotactic region, positioned between the sperm inlet and collection chambers (Figure 23A) so that only rheotactic sperm were imaged. In details, VSL appears to slightly increase from the static to the 11.04µl/h condition, remaining almost constant along the range of applied flow rates (Figure 23B). The same is observed for the VCL, whose average value

increases from static to flow condition, rising up to 12.42µl/h before experiencing a decrease due to the higher applied flow rate (Figure 23C). The flow is starting to become excessively high, causing bovine sperm to encounter increased resistance, hindering their ability to propel themselves effectively [114]. They continue to move counter-flow but with a lower velocity. Indeed, as specified in Table 6, moving from the minimum to the maximum flow rate, the velocity increases of 20µm/s shifting closer to the upper limit of the fluid velocity range observed to induce PR, found in literature. The relatively constant value of both velocities at different flow rates and with respect to the static condition finds accordance with literature results [57,114]. The relatively stable values of both velocities are also reflected in LIN, which remains quite constant across all analyzed conditions, lacking statistical significance (Figure 23D). However, a notable change is observed at 16.6µl/h, the highest applied flow rate, where a reduction in both VSL and VCL is evident. While VSL decreases by approximately 11% from the minimum to the maximum flow rate, VCL experiences only a 3% decrease. This could suggest that, as fluid velocity increases, sperm exert stronger efforts to proceed further. Consequently, their VCL, associated with vigorous motion, remains unchanged compared to the variation observed in VSL, inducing a reduction of LIN and therefore progressive motion.

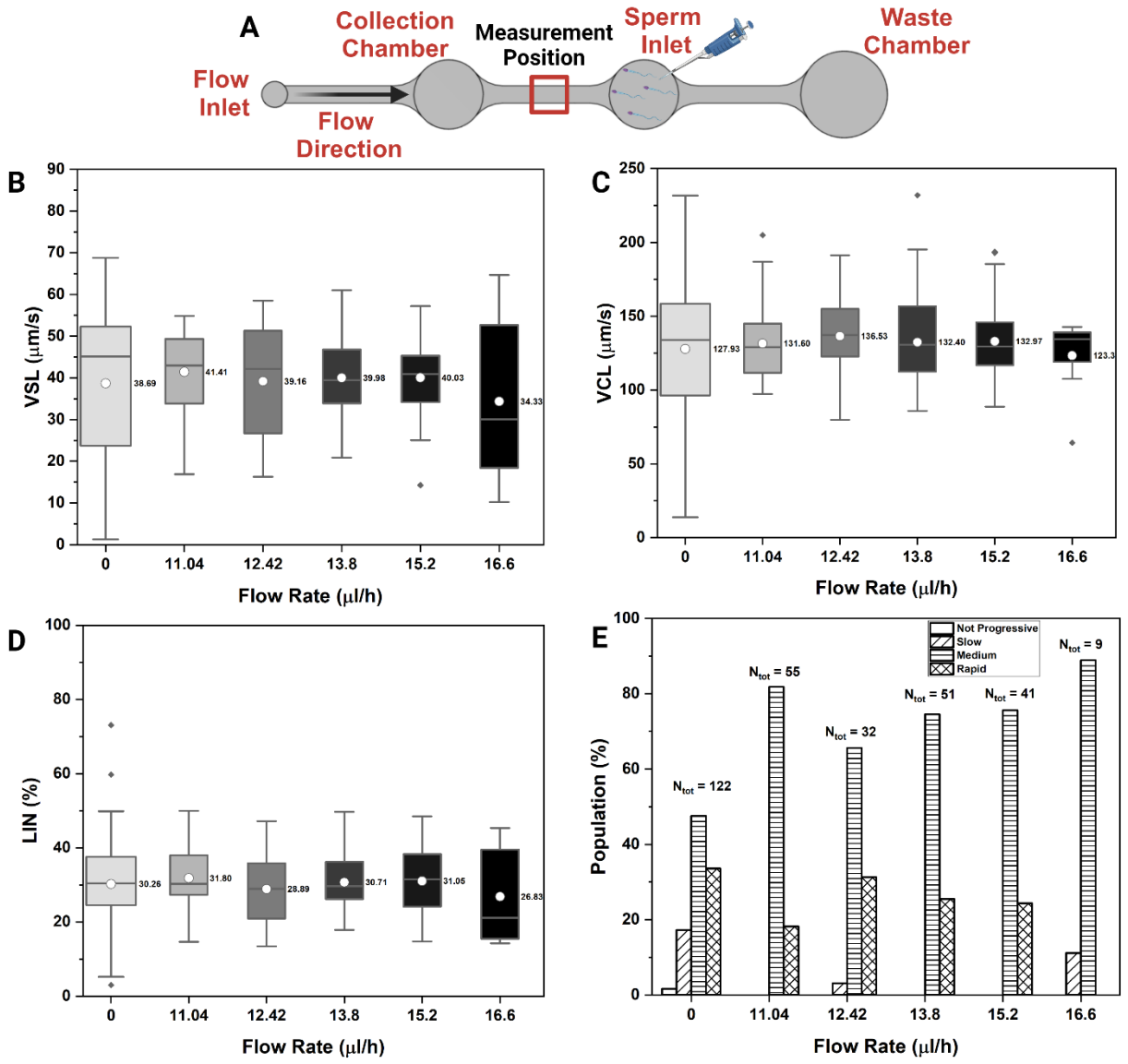

Figure 23. Biological validation of the microfluidic device. A) Schematic representation of the measuring procedure. Bovine sperm are loaded into the sperm inlet chamber, a flow is induced in the direction indicated by the black arrow (from left to right) and sperm were imaged at the center of the channel indicated as the measurement position by the red rectangle. **B)** VSL, **C)** VCL and **D)** LIN of the tracked sperm for different flow rate applied within the device. The values are shown as box charts displaying standard deviations, average values indicated by the white dots and specified by the number in bold, and median values represented by the horizontal lines inside the box. $N_0 = 122$, $N_{11.04} = 55$, $N_{12.42} = 32$, $N_{13.8} = 51$, $N_{15.2} = 41$, $N_{16.6} = 9$. p-value < 0.05 only for VSL between 11.04µl/h and 16.6µl/h. The statistical differences among all the other conditions for the three parameters are NS. **E)** Classification of motile bovine sperm based on VCL in: Not Progressive, Slow, Medium and Rapid according to the ranges in Table 3. The amount of sperm classified is the same of the other plots and are reported on top of the bar plots. The amount of sperm falling in each sub-class is represented here as percentages.

The results obtained for sperm velocity find accordance also in terms of sperm classification in motility sub-classes (Figure 23E). At CTRL (static condition), the sperm population is distributed across various motility classes, with a notable prevalence of Medium sperm. However, under flow conditions, strong evidence is a complete absence of Not Progressive and Slow sperm. Moving from 11.04µl/h to 15.2µl/h, the distribution remains relatively unchanged, showing a peak in the Medium sperm class, and a large amount of Rapid, except for a small proportion of Slow sperm observed at 12.42µl/h. This shift in distribution demonstrates the rheotactic ability of highly motile sperm, which navigate from the inlet towards the collection chamber. Additionally, it highlights the filtration capability of fluid-flow, effectively excluding Not Progressive and Slow sperm that fail to resist the flow and exhibit rheotaxis. Our findings reveal that fluid-flow serves to reorient sperm in the opposite direction for guidance, selectively allowing highly motile sperm progression without inducing strong changes in their velocities. This remains consistent across different volumetric flow rates and between static and flow conditions (Figure 23A and B). However, at the highest fluid flow rates (16.6µl/h) increased resistance of the flow slows down sperm, impacting their classification. Indeed, Rapid sperm completely disappear, while becoming slow having a reduced rheotactic ability.

Along this, we decided to classify the detected sperm into two main categories: “rheotactic” and “pushed back” [44]. Rheotactic cells demonstrate a clear progression against the flow, maintaining their ability to move further counter-flow. Pushed back, initially exhibiting rheotaxis, are subsequently pushed back as their motion becomes hindered by fluid-flow. Indeed, they either remain stationary, moving without significant progress, or, during the attempt to advance, they are dragged away by the flow (Figure 24). Additionally, there are some sperm which go back due to the pushing force exerted by the fluid.

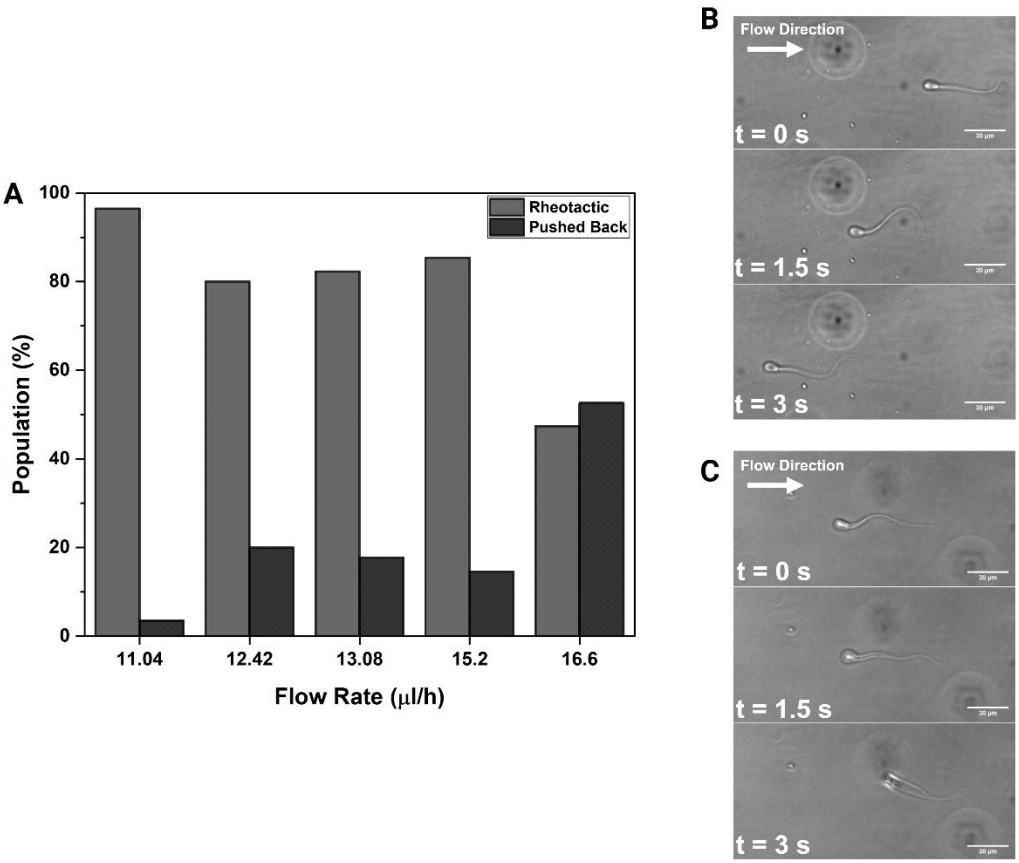

Figure 24. Evidence of the effect of increased flow on bovine sperm rheotaxis. A) Manual classification done on bovine sperm in: Rheotactic and Pushed Back sperm. The values here are presented as percentages and the total number of sperm onto which we performed the classification is the same of Figure 23. **B)** Actual images of rheotactic bovine sperm. As fluid flows in the direction of the white arrow on the top, sperm moves counterflow, advancing. **C)** Actual images of pushed back bovine sperm. The fluid direction is the same of B). Sperm is not able to progress further, and it is pushed back in the flow direction. Both images were realized by 3s brightfield acquisitions with 20x magnification.

At the lowest flow rate, most sperm exhibit rheotactic behavior, with only a small percentage of pushed back. However, when the flow rate becomes higher, there is a noticeable increase in the percentage of pushed back sperm, indicating that the fluid velocity has become too high for all sperm to progress along the microchannel. Despite variations in flow rates, the distinction between rheotactic and pushed back sperm remains consistent among the three intermediate flow rates. A more pronounced difference emerges at 16.6µl/h, where the percentage of pushed back cells surpasses that of rheotactic ones (Figure 24A). For further details, in Figure 24B, we reported a rheotactic sperm progressively moving against the flow, demonstrating sufficient motility to counteract it. On the other hand, a time-lapse sequence in Figure 24C depicts a pushed back sperm initially remaining stationary, with its head pointing opposite to the flow direction. Subsequently, it gets washed by the flow, undergoing a clockwise rotation, and turning its head in the same direction as the flow. This observation further demonstrates the filtering capability of fluid-flow and offers insights into potential scenarios within the

FRT. In this context, sperm are guided by the flow to swim in a specific direction. At the same time, the applied flow serves as an obstacle for those sperm that lack sufficient capability and motility, pushing them away. Consequently, these less competent sperm are separated from the more competent ones, which continue to advance. Examining the two cells in Figure 24B and C, their distinct behaviors suggest that the pushed-back one may not be as competent, healthy, or motile as the rheotactic one and, as a result, it gets filtered away. This filtration process could potentially favor the selection of healthier and more competent sperm, potentially enhancing the chances of successful fertilization. As a result, our device validation has provided us with valuable insights into the phenomenon of PR and has guided our selection of the optimal flow rate for subsequent experiments. Specifically, the lowest flow rate (11.02µl/h) appears to induce a robust rheotactic response in sperm. It enhances, even if not statistically significantly, their progressive motility, as evidenced by higher values of VSL. Importantly, this flow rate induced the lowest overall percentage of pushed-back sperm. Consequently, we have chosen to proceed with this flow rate for our experiments involving increased viscosity and sperm selection.

3.2.3. Sperm separation by microfluidics.

Once the effect of the optimal flow rate (11.04µl/h) on sperm rheotaxis was demonstrated, it was decided to apply it to separate a heterogeneous ample into two populations based on their motility. Specifically, the aim was to separate highly motile sperm, which exhibit rheotaxis in the collection chamber, from low motile or defective sperm, which move towards the right in the waste chamber (Figure 25B and C, respectively). Subsequently, their velocities were evaluated. Additionally, it is noteworthy that the population moving toward the waste chamber includes many sperm agglomerates and dead sperm.

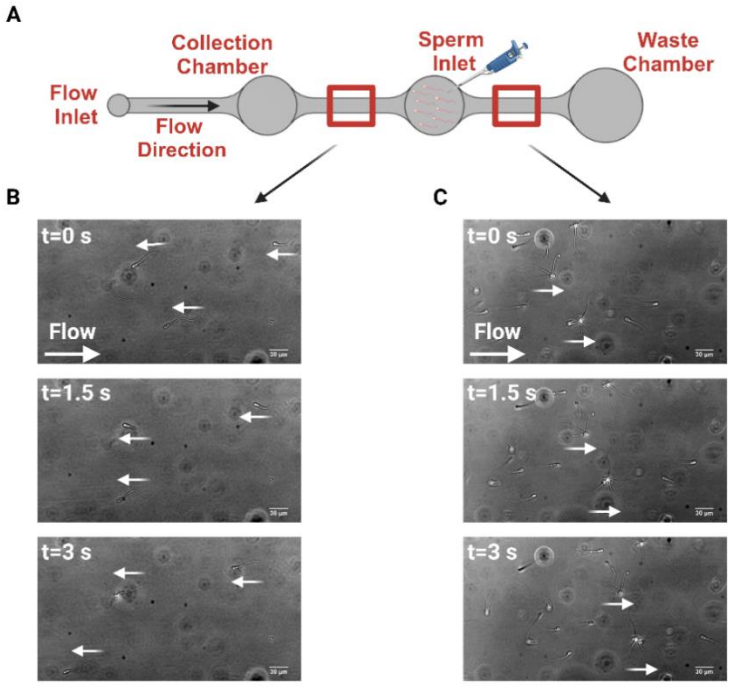

Figure 25. Bovine sperm separation principle. A) Schematic of the microfluidic device illustrating the flow direction and the two observation positions for both rheotactic (B) and washed away sperm (C), respectively. **B)** Rheotactic sperm,

imaged at three different time-steps, move in the opposite direction of the flow from the sperm inlet chamber towards the collection chamber. **C)** Washed away sperm (containing sperm aggregates and dead sperm) move in the flow direction from the sperm inlet towards the waste chamber. Both images were realized by 3s brightfield acquisitions with 20x magnification. The flow is indicated by the big white arrow, while the small white arrows indicate the direction of movement of sperm.

We allowed sperm to swim within the microfluidic device for approximately 15min. Subsequently, we proceeded to retrieve them from both the waste and collection chambers for further analysis. Initially, sperm were collected from the waste chamber, which was open and more accessible for retrieval using a pipette. The withdrawn sperm were then loaded into a 20µm deep chamber for motility assessment. The same procedure was followed for sperm in the collection chamber after removing the sealing cap.

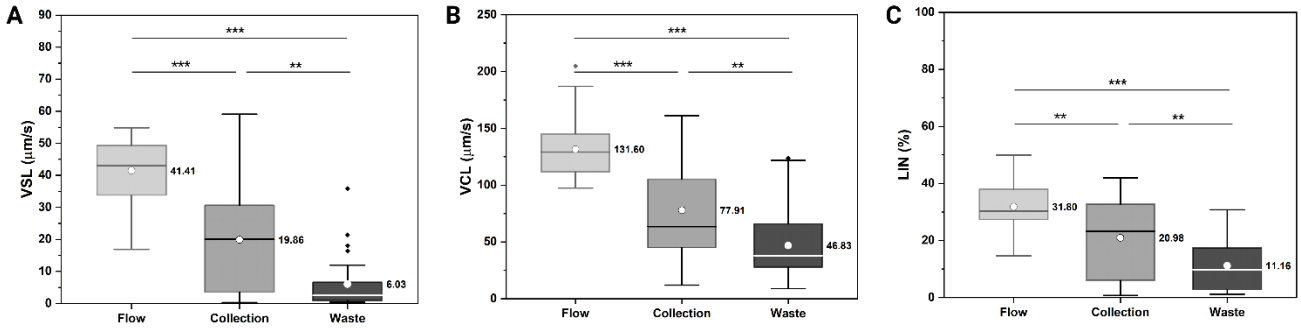

Figure 26. Bovine sperm separation. A) VSL, **B)** VCL and **C)** LIN of the sperm in flow conditions (inside the microfluidic device) and of the ones retrieved from collection and waste chamber, observed in a 20µm deep chamber. The values are shown as box charts displaying standard deviations, average values indicated by the white dots and specified by the number in bold, and median values represented by the horizontal lines inside the box. $N_{Flow} = 55$, $N_{Collection} = 29$ and $N_{Waste} = 27$. p-value < 0.001 for the three parameters compared between flow and waste and for VSL and VCL between flow and collection. p-value < 0.01 for the three parameters between collection and waste and for LIN between flow and collection.

Specifically, we compared the motility parameter values of the tracked sperm in flow conditions with the collected ones. The VSL of the collected sperm appears to be lower than that in flow condition but much higher than those of the sperm in the waste (Figure 26B). The same occurs also for the VCL and LIN (Figure 26C and D, respectively). The decrease in motility parameters in the collection chamber, compared to the flow condition, can be attributed to two main factors. Firstly, there is a geometric influence, as the microfluidic device has a depth five times greater than that of the chamber where collected sperm were analyzed. Secondly, this reduction could also be due to the presence of immotile sperm in the collection chamber, influencing the average velocity value. The presence of immotile sperm in the collection chamber does not necessarily indicate their death. Indeed, into an in-vivo context within the FRT, sperm adhere to the epithelium, after traversing the Fallopian tubes. They remain vital and deactivated, awaiting ovulation. During ovulation, chemical gradients

produced by the oocyte hyperactivate the sperm, allowing them to detach from the epithelial wall and move towards the oocyte for fertilization. The interaction with the epithelium provides essential molecules for sperm survival [126]. In our experimental setup, by collecting sperm after exposure to flow, we place them in a static chamber. Therefore, this condition could potentially induce their deactivation. However, an additional analysis would be required to assess their viability.

To partially address this point, we performed an additional experiment. Once we retrieved the sperm from the collection chamber, we reloaded them into the sperm inlet chamber for a second run. Essentially, after selecting them with the initial flow, we subjected them to flow again, and we observed their behavior.

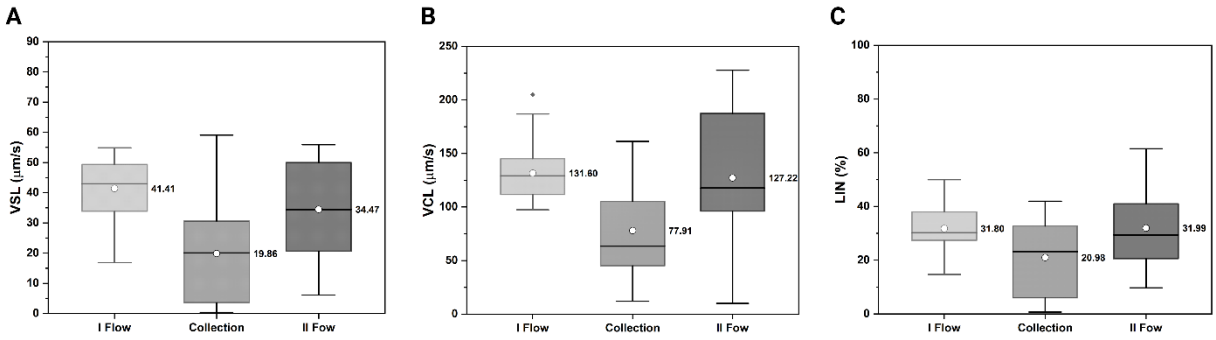

Figure 27. Application of a second flow on collected sperm. A) VSL, **B)** VCL and **C)** LIN of bovine sperm acquired in flow condition for the first time (I Flow - within the microfluidic device), of those retrieved from the collection chamber and observed in a 20µm deep chamber (Collection) and those reitroduced in the microfluidic device and subjected to a second fluid-flow (II Flow). The values are shown as box charts displaying standard deviations, average values indicated by the white dots and specified by the number in bold, and median values represented by the horizontal lines inside the box. $N_{I\ Flow} = 55$, $N_{Collection} = 29$ and $N_{II\ Flow} = 11$.

When comparing the velocity values of sperm tracked under these three different conditions (I Flow-20µm chamber-II Flow) we observe an initial decrease in both VSL and VCL into the chamber, while an increase, during the II Flow (Figure 27). This observation might suggest a potential reactivation of sperm, which could have experienced deactivation in the chamber post-collection, triggered by the reintroduction of flow conditions. The reduced number of sperm detected for the second time in flow can be attributed to challenges in precisely withdrawing the same quantity of sperm that initially reached the collection chamber. This difficulty arises from the collection process complexity and the larger dimensions of the chamber, resulting in some sperm loss during withdrawal.

Upon comparison of the sperm collected from the waste chamber with those retrieved from the collection chamber, a significant decrease in both VSL and VCL is evident (Figure 26A and B). Additionally, LIN is lower in the waste chamber, indicating a loss of progressive motility (Figure 26C). The observed reduction in velocity and progressivity in the sperm from the waste chamber can be attributed to the fact that these cells are washed away by the fluid, leading to a considerable presence of agglomerates and dead sperm. This suggests

that the immotile or defective sperm found in the waste chamber are indeed truly inactive, resulting in a pronounced reduction in motility parameters. Furthermore, the classification of sperm in both the collection and waste chambers supports this observation. Initially, we manually counted immotile, motile, and defective motile sperm in both conditions (Figure 28A). Therefore, we classified the motile ones into motility sub-classes based on their VCL, as previously described (Figure 28B).

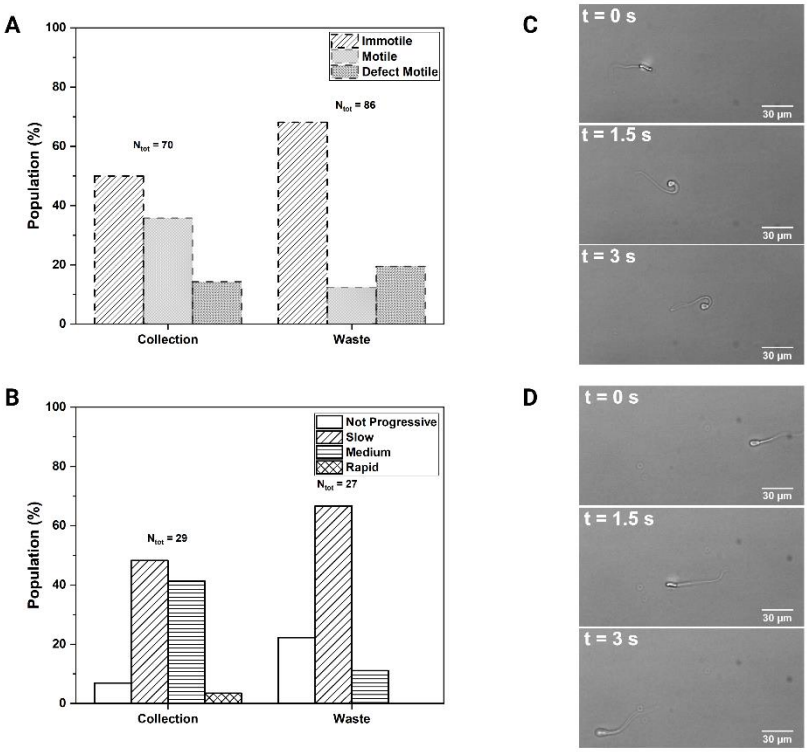

Figure 28. Classification of bovine sperm retrieved from collection and waste. A) Manual count and classification of acquired sperm in immotile, motile and defective motile sperm. **B)** Motile sperm were then classified based on their VCL as in Table 3. Numerosity is shown upon the bar plots. **C)** Actual images of a probably defective motile sperm which moves in a not progressive manner, found in the waste chamber. **D)** Actual images of a normal sperm moving progressively, found in the collection chamber. Both images were realized by 3s brightfield acquisitions with 20x magnification. The amount of sperm falling in each sub-class is represented here as percentages.

The key distinction arising from the waste and collection chambers lies in the distribution of sperm across different classes. Specifically, the waste chamber exhibits a higher percentage of immotile sperm compared to the collection chamber. Furthermore, there is a higher percentage of defective motile sperm in the waste chamber than in the collection chamber (Figure 28A). The defective sperm were classified manually by simply observing their structure at the microscope. Deeper morphological analysis should be performed to more certainly assess their abnormal morphology. As an illustrative example, we present real images of a defective sperm retrieved from the waste chamber and showing reduced progressive motility when compared to a normal

sperm found in the collection chamber (Figure 28C and D, respectively). These defective sperm, despite their motility, are still washed away by the fluid and accumulate in the waste chamber.

Also, in terms of classification, a clear distinction is noticed between the collection and waste chambers (Figure 28B). The collection chamber demonstrates an almost absent percentage of Not Progressive sperm, whereas the waste chamber has a higher proportion. This observation emphasizes that progressivity is higher in the collection chamber, as evidenced by LIN (Figure 26D). Additionally, the collection chamber is characterized by a larger percentage of Medium and a lower percentage of Slow sperm compared to the waste chamber. Notably, the waste chamber lacks entirely in rapid sperm, whereas the collection chamber, even if in a small percentage, contains them.

3.2.4. Combined influence of flow and fluid viscosity on bovine sperm motility parameters.

With the aim to more closely investigate the selection and guidance mechanisms within the FRT, we wanted to study how the combined influence of fluid-flow and rheology could impact sperm motility. In vivo, these two phenomena operate simultaneously in certain FRT regions, contributing to the natural selection of optimal sperm for successful fertilization. Through the microfluidic device, we conducted experiments introducing higher viscosity flows at the previously determined optimal flow rate. This provided additional insights into fluid rheotaxis under conditions of intermediate and high viscosity fluids. We replicated the experiments using three different viscosities corresponding to the fluids described in section 3: PBS (low viscosity), PVP 2wt% (intermediate viscosity), and PVP 5wt% (high viscosity).

Following the procedure described in 463.1.4, we performed experiments at varying fluid viscosities by keeping the same volumetric flow rate. The recording duration was set to 5s, given that, as explained earlier, bovine sperm exhibit slower motion in higher viscosity fluid. This extended duration was necessary to reconstruct reliable trajectories when observed under flow conditions. This approach differed from the one employed in static conditions, where sperm directionality was not so crucial. In flow conditions, 1s observations would be insufficient to comprehend their directionality within the device.

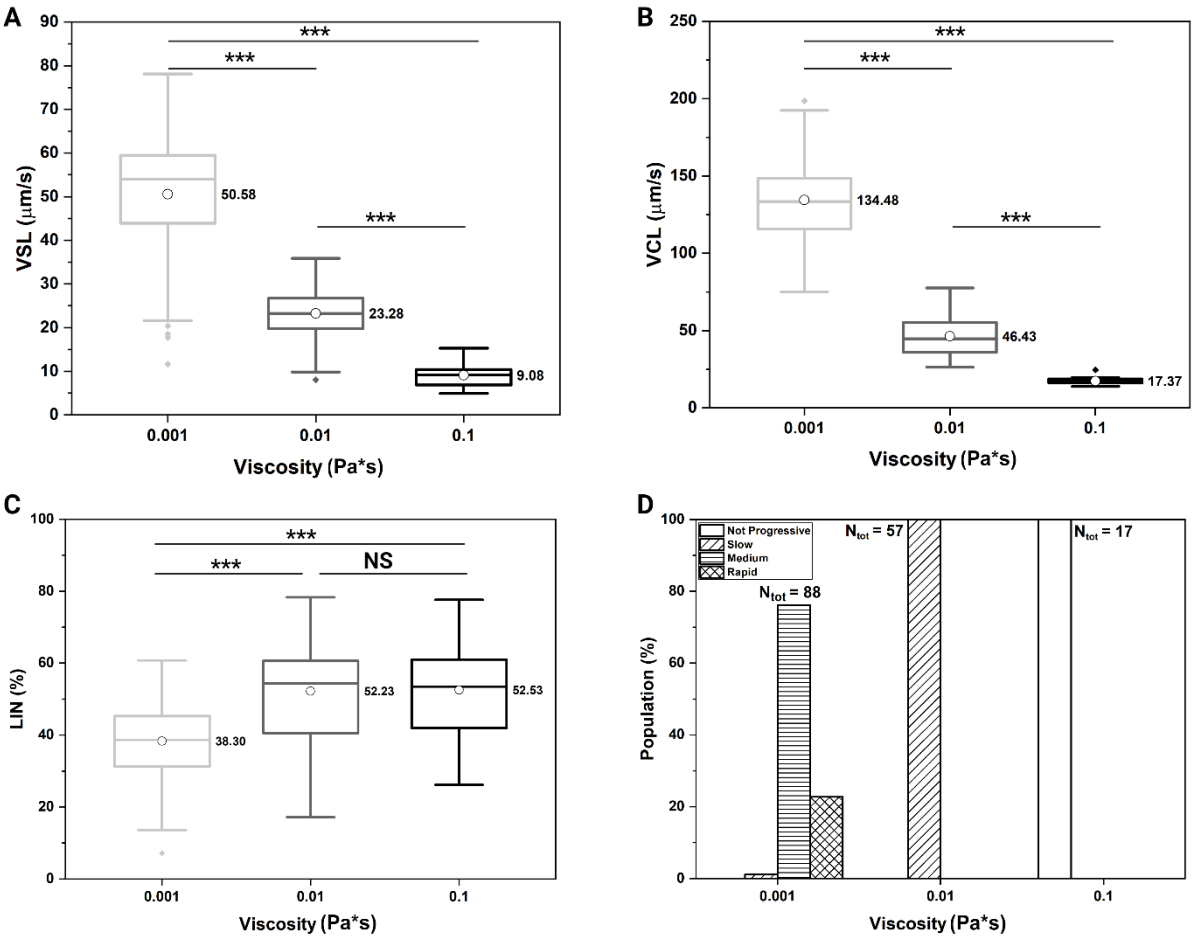

Figure 29. Combined effect of fluid-flow and viscosity on bovine sperm motility parameters. A) VSL, **B)** VCL and **C)** LIN of bovine sperm in different viscosities for the same applied volumetric flow rate imaged in the microfluidic device. The values are shown as box charts displaying standard deviations, average values indicated by the white dots and specified by the number in bold, and median values represented by the horizontal lines inside the box. $N_{0.001} = 88$, $N_{0.01} = 57$, $N_{0.1} = 17$. p-value < 0.001 for all the parameters among all the viscosities conditions, except for the LIN between intermediate and high viscosity. **D)** Classification of motile bovine sperm based on VCL in: Not Progressive, Slow, Medium and Rapid according to the ranges in Table 3. The amount of sperm classified is the same of the other plots and are reported on top of the bar plots. The amount of sperm falling in each sub-class is represented here as percentages.

What it is observed is that both VSL and VCL show a substantial decrease at intermediate and high viscosities when compared to low viscosity medium (Figure 29A and B). Indeed, the observed reduction in VSL is noteworthy, showing a decrease of approximately 54% and 82% at intermediate and high viscosity, respectively (Figure 29A). This reduction is more pronounced than static conditions (Figure 13 and Figure 14 in 2.2.3), although the decreasing trend aligns with previous observations. Notably, the VSL value at low viscosity appears higher than that observed in static conditions at the same viscosity. This difference could be attributed to the impact of fluid-flow, which selectively extracts the most progressive sperm in this case, while static conditions consider the entire sample for average velocity evaluation. However, the higher decrease

observed in VSL under flow conditions, can be attributed to the combined effects of fluid-flow and viscosity. This becomes more evident when comparing average values at high viscosity, where the VSL in flow conditions is lower than those observed in static.

Regarding VCL, its value is most significantly influenced than that of VSL, showing a decrease of about 65% and 87% when comparing intermediate and high viscosity conditions with lower viscosity, one (Figure 29C). This aligns with observations in static conditions, where VCL exhibited a more pronounced reduction (Figure 13 and Figure 14 in 2.2.3). In details, at low viscosity, VCL is higher in flow conditions than in static conditions. However, at intermediate viscosity, VCL shows a decrease when compared to static conditions with a more substantial difference observed at high viscosity.

This could suggest an indication that the combined effects of fluid-flow and increased viscosity lead to a reduction in the sperm net space gain within the device, and a probable increased drag on sperm motion. The combined effect of viscosity and flow results in a more pronounced slowing down of sperm, impacting both net space gain and vigorous motion. Consequently, only highly motile sperm can successfully advance in the microfluidic channel against the flow, while those with low motility or defects are unable to proceed and are filtered out from the overall sample. Moreover, in terms of LIN, its value is comparable to that in static conditions at low viscosity. Furthermore, the LIN value at intermediate viscosity exhibits an enhancement of sperm progressiveness, which, however, remains constant when transitioning to high viscosity in flow condition (Figure 29D). Of note, the LIN value at intermediate viscosity is higher than those observed in static conditions, highlighting that the flow is selectively favoring more progressive sperm, expressed as an increasing average LIN value (Figure 13 and Figure 14 in 2.2.3).

The distinctions in sub-classes are evident also in flow conditions (Figure 29E). At low viscosity, the population predominantly consists of a high percentage of Medium sperm along with a consistent percentage of Rapid sperm. In contrast, at intermediate viscosity, all rheotactic sperm are categorized as Slow, while at high viscosity, the overall population exhibits Not Progressive motility. Furthermore, there is a gradual reduction in the number of sperm capable of swimming further along the channel, reaching the measurement position (Figure 29A).

3.2.5. Combined influence of flow and fluid viscosity on bovine sperm motion pattern.

Similar to the approach used in static conditions (2.2.4), we performed phase-contrast acquisitions in flow conditions to assess how the combined influence of fluid viscosity and flow affects the rotational behavior of sperm. The results, both in terms of population and rolling parameters, closely replicate what we observed in static conditions (Figure 30).

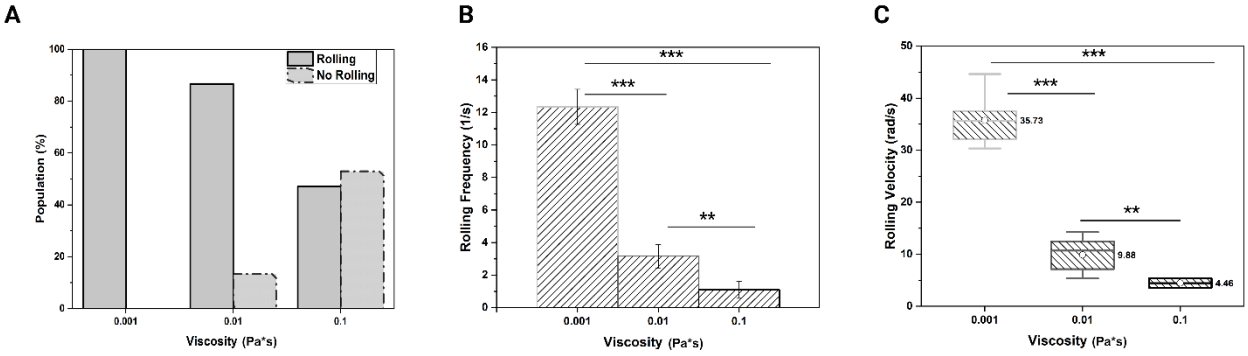

Figure 30. Combined effect of fluid-flow and viscosity on bovine sperm motion pattern. A) Percentage of rolling and no rolling sperm at varying viscosity expressed as percentages. $N_{0.001} = 100$, $N_{0.01} = 65$, $N_{0.1} = 8$. **B)** Rolling frequency (s^{-1}) of manually tracked rolling sperm at varying viscosity. Data are shown as bar plot indicating the average value and the relative standard deviation. $N_{0.001} = 15$, $N_{0.01} = 15$, $N_{0.1} = 4$. The differences are statistically significant among all the analyzed conditions (p-value < 0.001 comparing low viscosity with intermediate and high viscosity - p-value < 0.01 comparing intermediate with high viscosity). **C)** Angular rolling velocity (rad/s) of manually tracked rolling sperm at varying viscosity. The values are shown as box charts displaying standard deviations, average values indicated by the white dots and specified by the number in bold, and median values represented by the horizontal lines inside the box. The sample numerosity for each condition is the same as the rolling frequency. The statistical difference is the same as in the rolling frequency.

Notably, we observed that the percentage of rolling sperm is 100% at low viscosity (Figure 30A). However, this percentage gradually decreased with increasing fluid viscosity. Conversely, the percentage of no rolling sperm is 0% at low viscosity and progressively increases with viscosity (Figure 30A). Of interest, at intermediate viscosity, the percentage of no rolling sperm was lower than that observed in static conditions. This phenomenon occurs even at high viscosity, where the percentage of no rolling sperm is higher than that of rolling sperm, but it is lower than those observed in static conditions (Figure 16Ai and Bi). This discrepancy can be attributed to the fact that, we acquired sperm in the rheotactic region, resulting in a higher percentage of rolling, since only they are able to reach this position. However, under higher fluid viscosity, sperm exhibit continuous rolling behavior despite of a reduced frequency (Figure 30B). This aligns closely with static conditions (Figure 16Aii and Bii), as indicated by the average values, revealing that fluid-flow does not significantly influence the rolling behavior. Upon evaluating the oscillation of rolling angles, we computed the average angular rolling velocity for each specific viscosity condition at a constant flow rate (Figure 30C), as detailed in 2.2.4. We observed minimal differences between flow and static conditions at low viscosity, suggesting that, at this viscosity level, fluid-flow minimally affects the rotational motion, consistent with the observed frequency of rolling. However, at intermediate and high viscosity levels, we noted contrasting behaviors. The angular rolling velocity in flow conditions is smaller than that in the static at intermediate viscosity. Conversely, at high viscosity, the angular rolling velocity is higher than static (Figure 16Aiii and Biii). It is possible that, at intermediate viscosity, the combined effect of fluid-flow and increased viscosity

slows down sperm rolling velocity. This is attributed to fluid-flow acting as a guiding mechanism, inducing sperm rheotaxis in the opposite direction. At high viscosity, fluid-flow selectively extracts only highly motile and rapidly rotating sperm, in contrast to static conditions where all imaged sperm are considered without any selection performed. Based on the distinct motion behaviors of rolling and no rolling, we observed that only rolling sperm exhibit progressive counter-flow movement (Figure 31A-C), whereas no rolling ones lack rheotactic behavior and remain stationary, describing circular trajectories (Figure 31D-F).

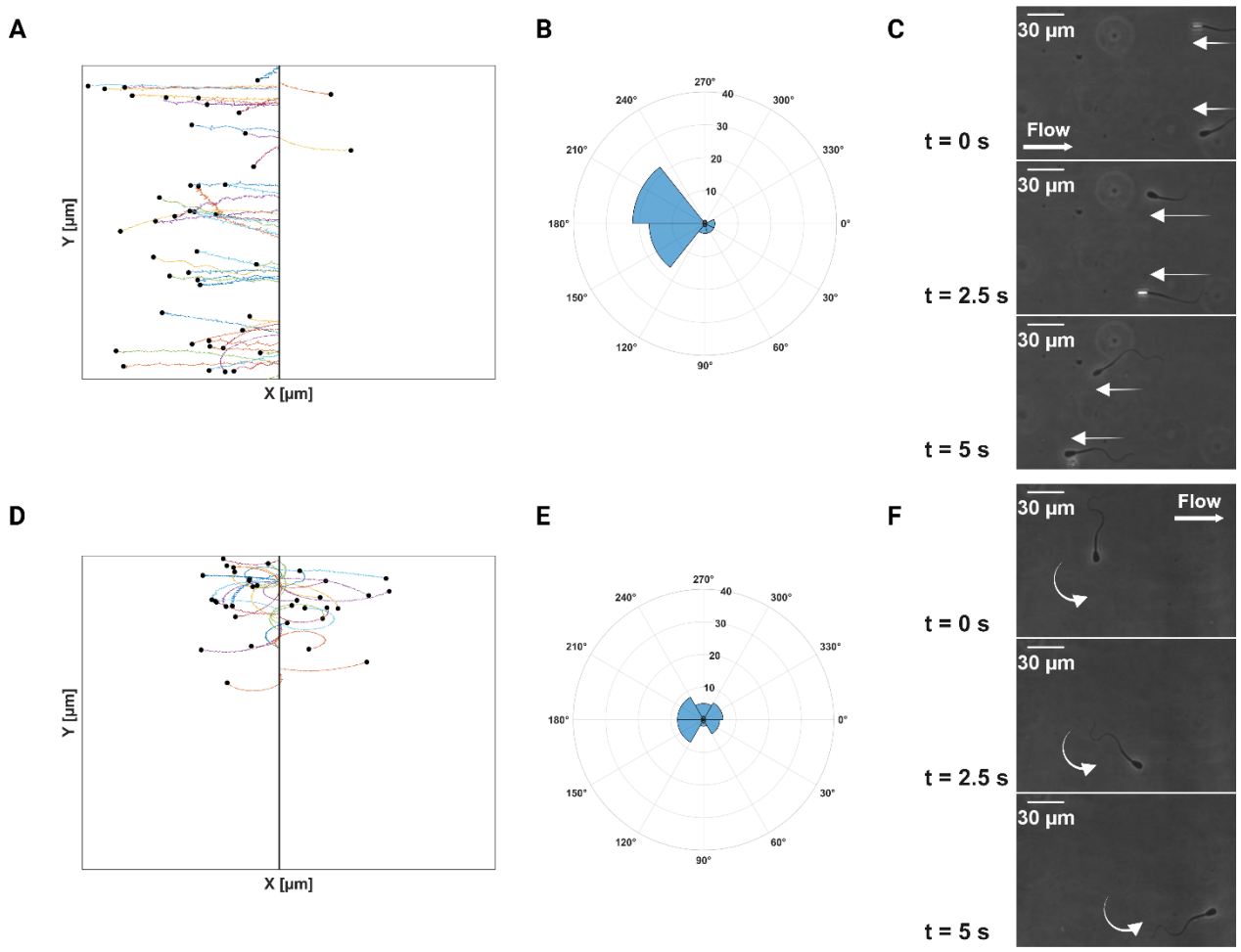

Figure 31. Rolling and no rolling sperm behavior with respect to fluid-flow. A-C) Rolling sperm trajectories in flow with the relative polar histogram of AD and time laps showing real images of rolling sperm advancing within the microfluidic device. **D-F)** No rolling sperm trajectories in flow with the relative polar histogram of AD and time laps showing real images of a no rolling sperm describing a circular trajectory independent of flow condition. The flow direction is from left to right. In both figures, the vertical line represents the initial point of each trajectory, while the black dot represents the final point. In the polar histogram the radial scale denotes the occurrence in a specific direction, while the circular scale represents the angles covered by sperm trajectories. The number of bins in the histograms was calculated as the root square of the sample numerosity in each experiment. $N_{Rolling} = 57$, $N_{Norolling} = 34$. C) and F) were realized by 5s phase contrast acquisitions with 20x magnification.

For rolling sperm, their trajectories are strongly aligned counterflow, showing a preferential orientation as indicated by the AD in the polar histogram. The AD illustrates that the overall sperm describe angles with the flow direction ranging between 120° and 240°, falling in the left quadrant, indicating a counterflow direction (Figure 31B). Some rolling sperm may not be strong enough to counteract the flow and move in the same direction, appearing in the polar histogram pointing in the right quadrant. Conversely, no rolling sperm do not experience rheotactic behavior, loosing progressive motility. They exhibit randomly oriented ADs with no preferred orientation (Figure 31E). This lack of response to the applied flow can be explained by their 2D motion. Therefore, the hydrodynamic interaction which develops between the fluid streamlines and the conical envelope described by the sperm tail beating pattern is not established for no rolling sperm, and therefore there is no production of reorienting torque which induced sperm reorientation counterflow [61]. We propose this as an innovative potential mechanism for separating highly motile sperm from low motile ones. Based on different motion dynamics, this method of sperm separation could potentially reflect their healthy state also in terms of morphology. Indeed, abnormal sperm are unable to move properly [67]. By observation, we demonstrated that, when a fluid-flow is applied, they move in circles without advancing through rheotaxis. An example is shown in Figure 31C and F. It illustrates rheotactic sperm moving progressively counter-flow, and a no rolling circular sperm that does not exhibit counter-flow movement, respectively. This is an example that mimics what occurs in the cervix of the FRT, where less motile or defective spermatozoa are not able to exhibit a rolling motion, resulting in a loss of progressiveness [68]. Unable to advance, they become trapped in the viscous matrix of cervical fluid and are subsequently filtered out from the rest of the progressively and highly moving sperm, which continue their journey [42,62].

4. Preliminary results for human sperm.

Here, we present preliminary results summarizing our approach with fresh human sperm, investigating how closely they behave compared to bovine sperm. We firstly conducted detailed morphological measurements of the head and tail, similar to what was done with bovine. Then, we confirmed, for different patients, the ability to modify sperm motility in rheological contexts characterized by increased viscosity, simulating conditions similar to cervical mucus. Furthermore, using our microfluidic approach, we observed their rheotactic behavior and how it allows the selection of motile sperm, effectively separating a heterogeneous sample into two populations. All of this was done with the aim of applying our approach more comprehensively to human cells, studying and selecting them to optimize ART procedures. It is important to note that what we have accomplished with humans is not as complete as what has been done with bovines, and this is a crucial step toward further refining our approach for human sperm.

4.1. Materials and Methods.

4.1.1. Media and Reagents.

Human Sperm were prepared by using pre-warmed Sydney IVF Gamete Buffer (Cook medical). Their motility was evaluated in three solutions having different viscosities: a low viscosity, consisting in the same buffer used for the preparation of the sample, and two polymeric solutions of Polyethylene-Oxide (PEO) (4MDa – Merck KGaA, Darmstadt, Germany). The polymeric solutions were obtained by dissolving the polymer powder in deionized water at a concentration of 0.5wt% and 0.9wt%, having increased viscosity and employed as a cervical mucus analogue. For human sperm, we chose to utilize PEO to mimic cervical mucus. This choice derives from observations in the literature indicating that prolonged exposure of human samples to PVP can have detrimental effects on their motility. Additionally, such exposure may cause cell damage, alter sperm function, and modify biological characteristics, leading to reduced success in ART procedures [127,128,129]. Indeed, PEO is a biocompatible and biodegradable polymer, often employed in many cellular and biological studies for several applications.

We assessed the viscosity of the three solutions used in our experiments using a stress-controlled rheometer (MCR 302, ANTON PAAR) with a cone-plate geometry (1deg - 50 mm). Specifically, we examined: a diluted solution containing the gamete buffer as a control (referred to as CTRL) with low viscosity, and two concentrations of PEO (4MDa) at 0.5wt% and 0.9wt%, representing intermediate and high viscosities, respectively. The zero-shear viscosity of these solutions was measured to be about $0.001\ Pa \cdot s$, $0.02\ Pa \cdot s$, and $0.08\ Pa \cdot s$, covering three orders of magnitude. The three solutions were tested across a broad range of shear rates, encompassing three orders of magnitude from $1\ s^{-1}$to $10^3\ s^{-1}$. The distinction between these fluids and the PVP solutions lies in their behavior, which exhibits a more pronounced shear-thinning tendency, particularly noticeable in the case of the 0.9wt% concentration. Nevertheless, it is important to note that our experiments consistently operate within shear rates where these fluids enter their Newtonian plateau,

maintaining a constant viscosity. From now on we will refer to these three conditions as CTRL, intermediate viscosity and high viscosity, respectively.

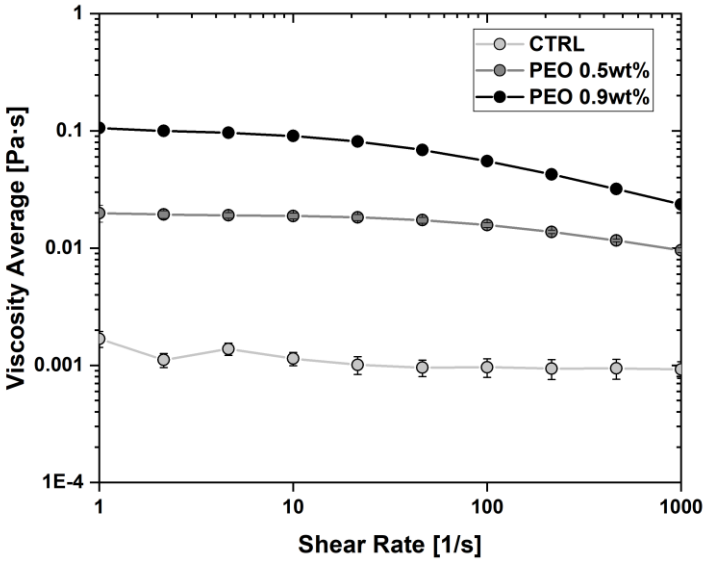

Figure 32. Viscosity measurements of PEO solutions. The viscosity ($Pa \cdot s$) is plotted against the shear rate (s^{-1}) for three conditions: CTRL (Gamete Buffer – light grey), which has water viscosity, PEO 0.5wt% (intermediate viscosity – dark grey) and PEO 0.9wt% (high viscosity - black). The curves show a shear thinning behavior at high shear rate, but a Newtonian one at low shear rates. The three curves represent the average value obtained from three measurements and the relative standard deviation.

4.1.2. Sample Preparation.

Fresh human sperm samples were donated by the Azienda Ospedaliera Universitaria (AOU) "Federico II" (Naples). The samples were simply diluted into the three solutions having different viscosities at a concentration of $3 \cdot 10^6$ sperm/ml (Figure 33A). The motility analysis was conducted across varying viscosities using sperm obtained from five patients. Notably, the initial concentration of each sample was not standardized, unlike in the case of bovine sperm. The initial sperm concentrations for the five patients, denotes as P_1-P_5, are reported in Table 7.

Table 7. Sperm concentrations of human patients.

Patient	Sperm Concentration (10^6 sperm/ml)
P_1	90
P_2	15
P_3	30
P_4	40
P_5	30

For humans, it was not necessary to perform centrifugation or sample washing as the samples were fresh and maintained in their native seminal fluid. This posed no issues when diluted in PEO solutions with respect to cryopreserved bovine sperm (see 2.1.2). Additionally, for human samples, we aimed to preserve conditions as physiological as possible, avoiding external actions that could potentially alter their motility. In addition, in contrast to bovine sperm, which we washed with centrifugation and then diluted in Gamete buffer before use, human sperm samples are diluted as they are, directly in the three viscosity conditions. Indeed, in the case of bovine sperm, the original solution viscosity is essentially the one of water. Consequently, when these cells are introduced into polymeric solutions, there is no modification of the final viscosity. On the other hand, for human samples, variations in the starting viscosity might occur due to certain pathologies or inflammatory conditions. Consequently, diluting such samples in polymeric solutions could potentially lead to changes in the final viscosity of the solution.

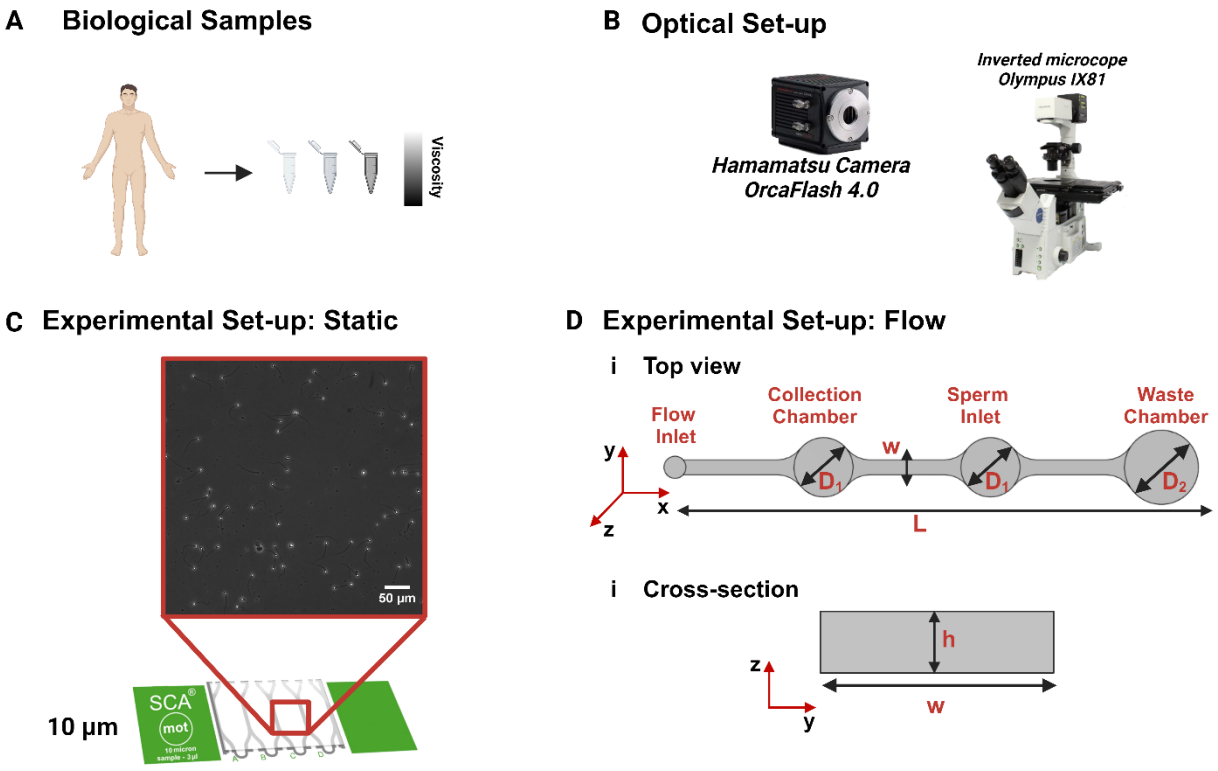

Figure 33. Human sperm analysis. A) Fresh human sperm were employed in the analysis, and they were simply diluted at the desired concentration in the three viscosity solutions. **B)** Optical set-up employed in the analysis. An inverted microscope and a rapid CMOS camera were employed for phase contrast acquisitions at 45fps. **C)** Experimental set-up in static conditions. SCA® motility chamber of 10µm in depth, usually employed for human sperm motility analysis. Real images of bovine sperm swimming in the chamber are shown in the image as a representative example of our phase contrast acquisitions. **D)** In-house produced microfluidic device. i) Schematic representation of the top view of our microfluidic device (as seen from the microscope) showing flow inlet, sperm inlet chamber for sperm loading, collection chamber for rheotactic sperm retrieval and waste chamber for the collection of dead and effective sperm. ii) Microfluidic

device rectangular cross-section indicating a large aspect ratio. The image shows the relative dimensions which are summarized in Table 5.

4.1.3. Acquisitions.

The optical set-up employed for the acquisitions of sperm was constituted by an inverted microscope (Olympus, IX81) equipped with a CMOS camera (ORCA FLASH 4.0, Hamamatsu Photonics K.K.) (Figure 33B). Only phase contrast acquisitions (1s for static and 5s for flow condition) were performed for human sperm owing to their oval-shaped head which allowed an optimal reconstruction of sperm trajectories by means of our MATLAB® routine. Acquisitions were performed with an objective magnification of 20x, a frame rate of about 45fps. The experimental set-up for static experiments was constituted by a standard counting chamber commonly employed by CASA systems for analyzing mammalian sperm. The counting chambers were purchased from MICROPTIC (MICROPTIC S.L., A Hamilton Thorn Company, Barcelona, Spain) and are specifically designed for human sperm motility analysis, featuring a 10µm depth (Figure 33C). Regarding the flow experiments, we employed our microfluidic device (Figure 33D), presented in 3.1.1, by following the experimental approach described in 3.1.4.

4.1.4. Data Analysis.

Single sperm heads were tracked with our MATLAB® routine, which calculated the motility parameters, discussed in 2.1.4. Motility classification was performed here by following a different rule. We employed the conventional classification in Not Progressive, Slow and Rapid sperm, defined by the WHO [70], following the ranges in Table 8. The ranges here are defined in terms of VSL.

Table 8. Motility sub-classes definitions according to WHO [70]**.**

Class	VSL $[\mu m/s]$
Non-Progressive	$0 < VSL < 5$
Slow progressive	$5 < VSL < 25$
Rapid progressive	$VSL > 25$

Additionally, using 40x, we also performed a manual analysis (by means of Imagej) to assess various morphological parameters of the sperm head, including its area, length, width, and thickness and the approximated length of the human sperm flagellum. This higher magnification was necessary due to the slender nature of the flagellum compared to the head, ensuring clearer visualization. Measurements of the flagellum length were taken when it was as straight as possible. Statistical analysis was performed as outlined in 2.1.5.

4.2. Results and Discussion.

4.2.1. Morphological Analysis.

Human sperm exhibit 3D movements consisting of translational and rotational motions, the latter being visible through the motion of the head. As for bovine sperm, two different configurations for the sperm head can be observed, referred to as Face on and Rim on. However, in the case of humans, the difference is less pronounced compared to bovine sperm due to their more oval shape as opposed to the paddle-like shape observed in bovine sperm [130] (Figure 34).

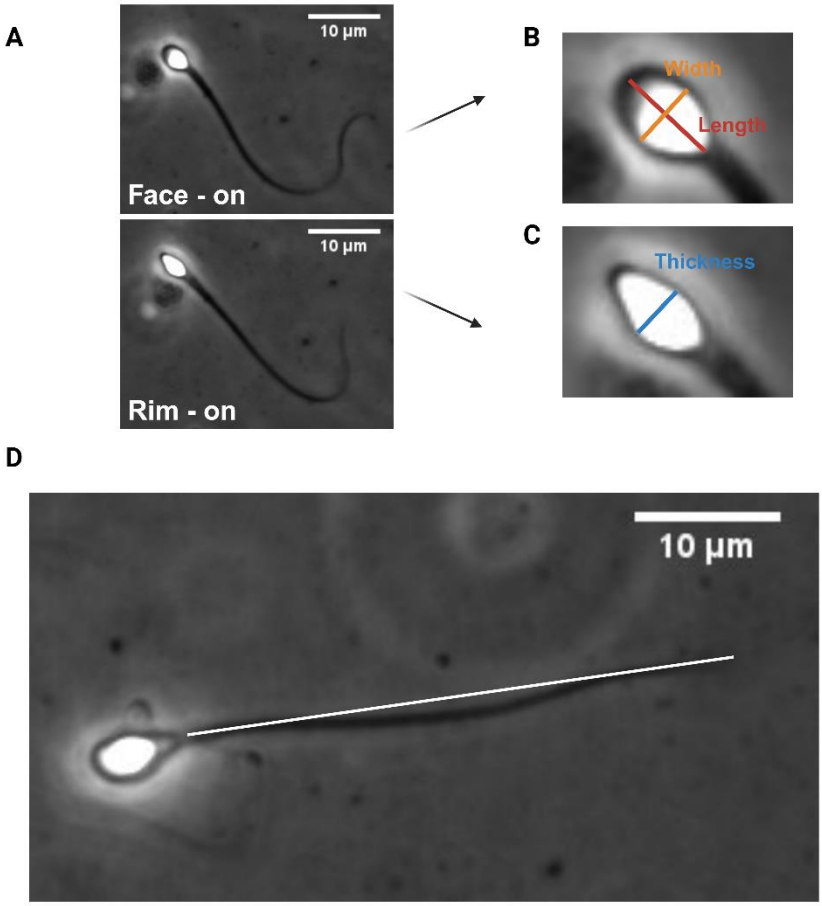

Figure 34. Representation of human sperm morphological analysis. A) Real images of a human sperm in free swimming exhibiting head rolling (40x - Phase contrast). The two configurations assumed by the sperm are shown and named "Facen-on" and "Rim-on". **B)** Zoom-in of the sperm head in the Face-on configuration showing its two main dimensions: the width (in orange) and the length (in red). **C)** Zoom-in of the sperm head in the Rim-on configuration showing its thickness (in blue). **D)** Real image of a human sperm. The tail length measured is shown in white, superimposed on the real image. It is determined when the sperm tail was as straight as possible.

When compared to bovine sperm, the differences between the two configurations of Face-on and Rim-on is not so obvious Figure 34B and C. Indeed, by observing the head in the two configurations, the width and the thickness are similar each other (Table 9).

Table 9. Measured morphological parameters of human sperm head and tail. For the head and tail N=16 and N=24 cells were analyzed, respectively.

Dimension	
Head Area [μm^2]	11.02 ± 2.38
Head Length [μm]	5.19 ± 0.70
Head Width (Face-on) [μm]	3.23 ± 0.27
Head Thickness (Rim-on) [μm]	2.05 ± 0.14
Tail Length [μm]	38.09 ± 3.50

The measured parameters of the sperm head are consistent with the existing literature ranges on the morphometric evaluation of human sperm head [10,41]. Morphological analysis was extended to include the tail length. The tail length was assessed by measuring it in its straightest configuration during recording (Figure 34D and Table 9), as reported in the literature [10].

4.2.2. Fluid viscosity influence on human sperm motility parameters.

Here, we focus on data from P1 whose sperm initial concentration is reported in Table 7, as determined visually by the trained operator, and exhibited a normal viscosity of seminal fluid. This helped minimize the impact of sample viscosity during the dilution process within the polymeric solution. By observing sperm motion within the 10µm chamber, VSL and VCL are considerably lower than those observed in bovine sperm. This discrepancy is attributed to the inherent differences in species, including distinct morphology and structure that influence their propulsion mechanisms[10]. However, when comparing the VSL and VCL values for human sperm at CTRL, we find them to be in line with the ranges found in literature [131] (Figure 35A and B). The impact of viscosity on human sperm motility is less pronounced compared to bovine sperm but remains notable, particularly for VCL. As for bovine, the effect is more significant for VCL than for VSL. Specifically, while VSL decreases by approximately 45% from CTRL to intermediate viscosity, VCL experiences a more substantial reduction of about 75%. This suggests that viscosity has a stronger effect on vigorous motion, particularly in diminishing the curvilinear motility component. However, we do not observe a distinct pattern where the VSL is higher at high viscosity compared to intermediate viscosity (Figure 35A), while the VCL remains relatively constant between them (Figure 35B). In general, human sperm samples exhibit greater heterogeneity, displaying a wide range of velocities among individual sperm. This variability could be attributed to the fact that the human samples are obtained from patients whose health status was unknown. There is a possibility that these samples include individuals with health issues, contributing to the less linear and ordered trend observed compared to bovine sperm. A consistent observation in both human and bovine

sperm is the increase in LIN with the rise in viscosity, showing statistically significant differences (Figure 35C). This results in more straight trajectories, primarily driven by a more substantial decrease in VCL than in VSL as viscosity increases. The increase in LIN reflects the flattening of the lateral head oscillations (related to the VCL reduction) already observed in literature by comparing low and high viscous solutions [40].

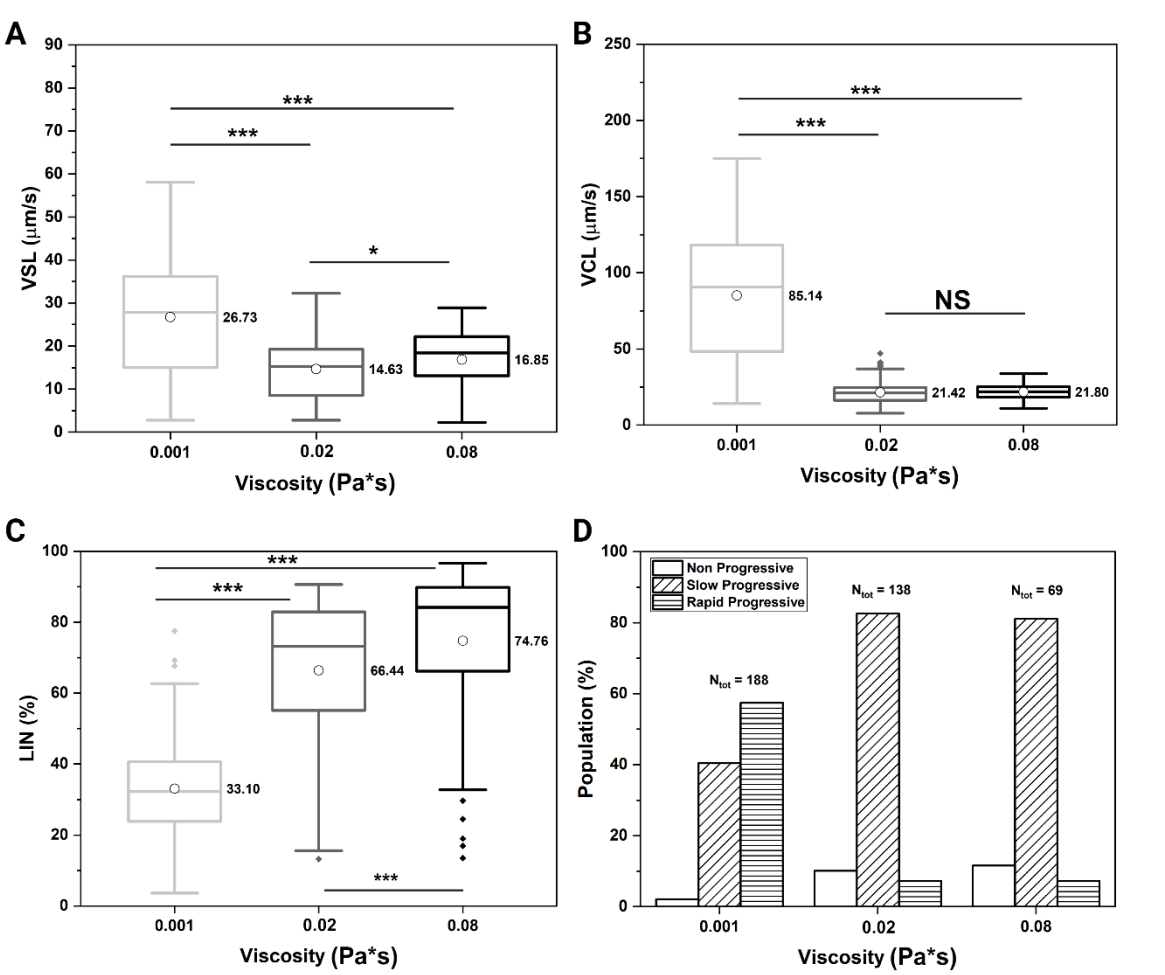

Figure 35. Influence of increased viscosity on human sperm motility. A) VSL. **B)** VCL. **C)** LIN. The values are shown as box charts displaying standard deviations, average values indicated by the white dots and specified by the number in bold, and median values represented by the horizontal lines inside the box. $N_{0.001} = 188$, $N_{0.02} = 138$, $N_{0.08} = 69$. p-value < 0.001 for almost all the conditions compared among them. The exception is the VSL between intermediate and high viscosity, where p-value < 0.05, and the VCL between intermediate and high viscosity, where p-value > 0.05, indicating NS. **D)** Classification of motile human sperm based on VSL in: Non-Progressive, Slow progressive and Rapid progressive according to the ranges in Table 8. The amount of sperm classified is the same of the other plots and are reported on top of the bar plots. The amount of sperm falling in each sub-class is represented here as percentages.

In terms of motility classification, based on VSL, the results align consistently with prior observations. Initially, at CTRL, the sperm population is more concentrated within the Rapid class. However, this distribution changes when considering intermediate and high viscosities. The tracked sperm shift from the Rapid class towards the Slow class, resulting in a distinct peak that reflects the reduction in VSL (Figure 35D). Additionally, the percentage of Non-Progressive sperm increases under these rheological conditions, while the Rapid class significantly decreases. The shift towards the slower classes is less pronounced in human sperm than observed in bovine sperm. This difference is attributed to the fact that viscosity more strongly influences VCL for both species. Of note, we observed the gradual decrease in the number of tracked sperm as viscosity increases. This suggests a selection mechanism offered by viscosity, potentially trapping defective and less motile sperm. This may replicate physiological processes within the FRT, where viscosity acts as a selective force.

The other patients were analyzed in the same experimental conditions, and the results are summarized in the following tables.

Table 10. Motility parameters and classification of other patients examined at CTRL.

	VSL ($\mu m/s$)	VCL ($\mu m/s$)	LIN (%)	Numerosity	Non-Progressive (%)	Slow (%)	Rapid (%)
P2	22.3 ± 12.7	57.3 ± 26.9	37.9 ± 17.8	85	15.29	37.65	47.06
P3	21.5 ± 13.5	49.0 ± 24.5	41.5 ± 16.3	485	16.29	42.06	41.65
P4	32.5 ± 10.8	77.4 ± 25.5	43.5 ± 13.6	245	0.41	24.90	74.69
P5	13.8 ± 11.1	55.1 ± 22.4	24.3 ± 13.3	88	25	57.95	17.05

Table 11. Motility parameters and classification of other patients examined at intermediate viscosity.

	VSL ($\mu m/s$)	VCL ($\mu m/s$)	LIN (%)	Numerosity	Non-Progressive (%)	Slow (%)	Rapid (%)
P2	20.3 ± 12.3	31.1 ± 12.7	59.4 ± 24.1	52	19.23	42.31	38.46
P3	20.9 ± 8.5	29.7 ± 7.3	68.4 ± 18.6	32	3.13	65.62	31.25
P4	27.9 ± 8.7	38.1 ± 9.7	72.6 ± 15.1	187	0.53	25.67	73.80
P5	9.2 ± 5.7	30.3 ± 15.8	33.3 ± 14.8	33	21.21	75.76	3.03

Table 12. Motility parameters and classification of other patients examined at high viscosity.

	VSL ($\mu m/s$)	VCL ($\mu m/s$)	LIN (%)	Numerosity	Non-Progressive (%)	Slow (%)	Rapid (%)
P2	19.9 ± 8.4	25.1 ± 7.2	77.2 ± 17.8	95	3.16	70.53	26.31
P3	18.2 ± 8.6	25.7 ± 8.4	69.3 ± 23.1	59	8.48	62.71	28.81
P4	22.7 ± 7.5	28.6 ± 6.5	78.1 ± 16.2	223	0.90	51.57	47.53
P5	5.6 ± 4.3	14.6 ± 7.4	38.1 ± 16.6	79	62.03	37.97	0

In summary, the trends observed in VSL, VCL and LIN are consistently regular across all analyzed patients. Both velocities exhibit a decrease as viscosity increases, while LIN experiences an incremental rise. This pattern is further reflected in the classification results, revealing a gradual decrease in the Rapid class and an increase in the Slow class percentages (Table 10, Table 11 and Table 12). These findings provide additional confirmation of the impact of cervical mucus on sperm motility.

4.2.3. Microfluidic human sperm selection by rheotaxis

Here, we proceeded to investigate the effects the optimal flow rate of 11.04µl/h on human sperm. As for bovine sperm (see 3.1.4), we observed the movement of sperm within the rheotaxis channel, demonstrating their migration from the sperm inlet to the collection chamber. After approximately 15min, sperm were collected from both the waste and collection chambers for further analysis of motility. The fluid velocity within the device of about 41µm/s since it still falls within the ranges of fluid velocity observed to determine PR of human sperm [65].

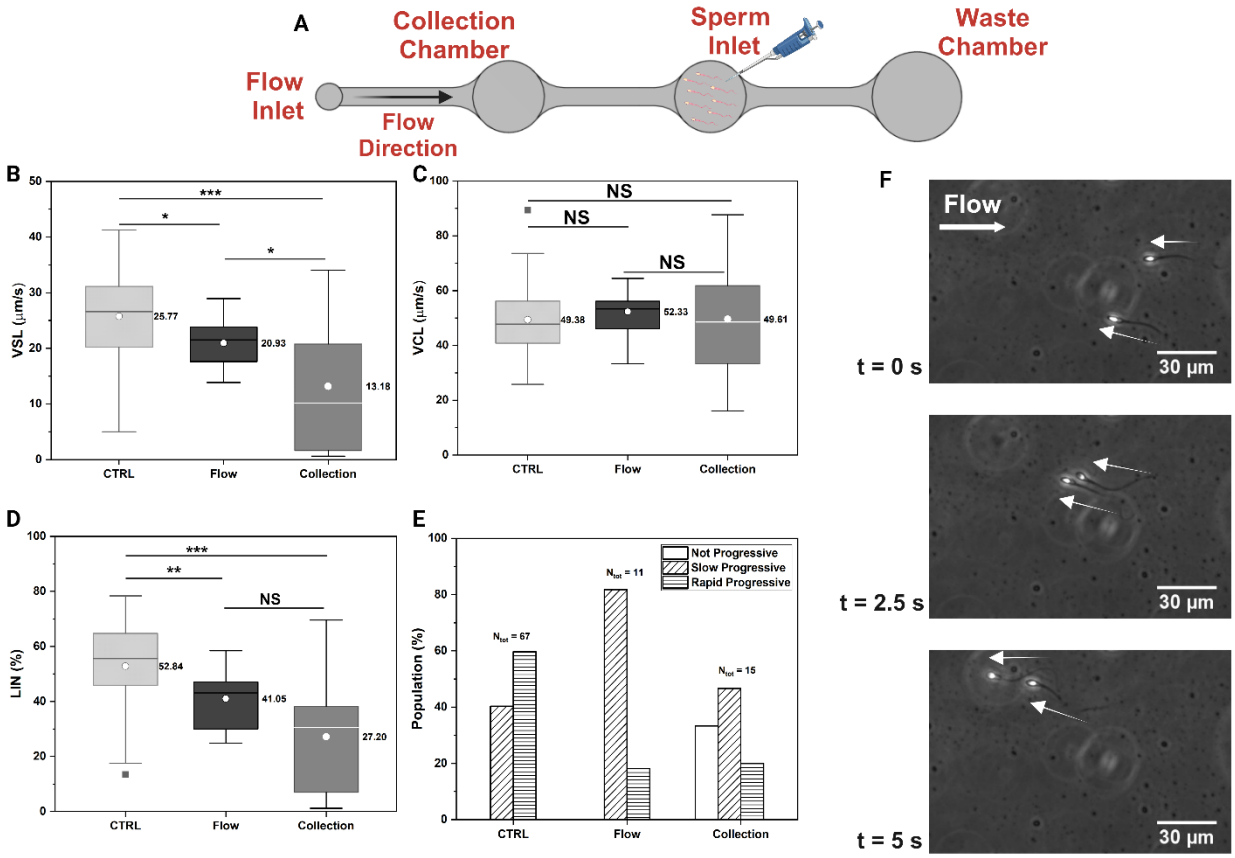

Figure 36. Human sperm collection by microfluidics. A) Schematic representation of the measuring procedure. Human sperm are loaded into the sperm inlet chamber and a flow is induced in the direction indicated by the black arrow (from left to right). **B)** VSL, **C)** VCL and **D)** LIN of human sperm at CTRL, flow conditions compared to the one of the sperm retrieved from the collection chamber and images into the 10 µm chamber. The values are shown as box charts displaying standard deviations, average values indicated by the white dots and specified by the number in bold, and median values represented by the horizontal lines inside the box. $N_{CTRL} = 67$, $N_{Flow} = 11$, $N_{Collection} = 15$. p-value < 0.001 for both VSL and LIN between CTRL and Collection. p-value < 0.01 for LIN between CTRL and Flow. p-value < 0.05 for VSL between CTRL and Flow and between Flow and Collection. As for the VCL p-value > 0.05 among all conditions (NS). **D)** Classification of motile human sperm based on VSL in: Non-Progressive, Slow and Rapid according to the ranges in Table 8. The amount of sperm classified is the same of the other plots and are reported on top of the bar plots. The amount of sperm falling in each sub-class is represented here as percentages.

Motility parameters obtained under flow conditions were compared with both the CTRL, representing raw semen before exposure to fluid-flow, and the collection, consisting of sperm retrieved from the collection chamber after fluid-flow (Figure 36). Analysis reveals that VSL appears to be higher at CTRL than under flow conditions (Figure 36B). In contrast, regarding VCL, there is a slight increase in flow conditions (Figure 36C). This limited significance for human sperm swimming against fluid-flow, compared to the CTRL, aligns with previous observations for human sperm [57]. This behavior suggests that human sperm, when subjected to fluid-flow, experience a slowdown in terms of net space gain. However, they respond by exerting stronger propulsion efforts, leading to an increase in the curvilinear motility component. This discrepancy results in the observed reduction in LIN, contributing to less progressive sperm (Figure 36D). It is noteworthy that the effect of fluid-flow alone differs from the influence of fluid viscosity, which induces an increase in progressivity and straighter trajectories with reduced head oscillation. Concerning the collected sperm, the trend observed for bovine sperm (Figure 26) is also evident here, characterized by smaller velocities compared to flow and CTRL conditions. However, only VSL shows significant differences among conditions, while VCL seems to remain constant across all conditions. Overall, VCL exhibits an increase in flow conditions, reverting to the initial value observed at CTRL when collected (Figure 36C). The distinctive aspect, compared to what was observed in bovine sperm, is that while VSL is lower for the collected human sperm, aligning with the bovine trend, VCL remains relatively constant, possibly maintaining their motility as observed at CTRL. This could be attributed to an intrinsic heterogeneity of samples.

Here, a single human sample with an initial concentration of $5 \cdot 10^7$ sperm/ml and normal viscosity was tested. Nevertheless, the results of our selection mechanism show a decrease in terms of progressivity. This slowdown is attributed to the presence of some Non-Progressive spermatozoa in the collection chamber (Figure 36E). In terms of motility classification, it reflects the lower values of VSL between CTRL and both flow and collection conditions. The CTRL condition is characterized by the complete absence of Non-Progressive sperm, indicating that the sample is, in principle, healthy, at least from a motility standpoint. In flow conditions, the rheotactic sperm exhibit slower but still progressive motility, successfully advancing towards the collection chamber. However, upon retrieval from the collection chamber and analysis in the 10µm chamber, a certain percentage of Non-Progressive sperm becomes apparent, evidenced by the reduction in VSL. It is crucial to note that the number of progressive (slow plus rapid) collected sperm is still higher than the count of Non progressive sperm (Figure 36E). Moreover, sperm progressivity is often associated with a higher probability of success in ART procedures [90].

5. Conclusions and Future Perspectives

Male infertility is considered nowadays as a global health issue which affects many couples worldwide leading to increasing interest from the scientific community. It is typically diagnosed by evaluating three main aspects of male reproductive cells: sperm motility, morphology, and count. Conventional analysis methods rely on manual examination of semen samples, which is subjective and can vary between operators and laboratories. However, the WHO standards are difficult to be reached, leading to inconsistencies among different laboratories and there is no universally accepted definition of infertility. CASA systems offer a more objective alternative but are influenced by operational settings and are characterize by a high cost and limited accessibility to the used algorithms, leading to a reduced employment in clinical practice. Furthermore, both types of analysis overlook the morpho-physical interactions sperm have within the FRT and the native 3D motion of sperm, since they analyze them in shallow chambers, hindering their motion. Additionally, conventional techniques used to select the best sperm for ART procedures often damage cells due to invasive processes, and they only select sperm based on motility under non-physiological conditions. Therefore, the investigation of the interplay between applied fluid-flow, viscosity and geometrical confinement is of fundamental importance to improve analysis and selection of sperm within a physiological-like context.

Here, we propose a straightforward approach for analyzing and selecting sperm by replicating the conditions of the FRT using both static and dynamic approaches. We aimed to enhance conventional techniques and provide additional tools for diagnosis and treatment. Bovine sperm were used as a model to explore the effects of geometric confinement and viscosity under static conditions, and to investigate the interplay between fluid-flow and viscosity under dynamic conditions, key barriers faced by sperm in the FRT. We demonstrated how geometric confinement influences sperm motility by limiting their 3D movement, flattening trajectories, and slowing them down. In addition, viscosity has a significant impact on motility, proposing an alternative analysis technique that comprehensively investigates sperm motion in high-viscosity conditions similar to those found in the cervical canal of the FRT. This lays the foundation for a groundbreaking analysis to distinguish between highly and low motile sperm, as those maintaining progressivity are clearly distinct from the ones which have impaired motility, due to fluid viscosity effects. Additionally, we examined the 3D motion of sperm, a commonly overlooked aspect in conventional analysis, uncovering intriguing insights into rotational motion and introducing additional parameters for defining sperm quality. By observing 3D rolling motion, we proposed an additional parameter for diagnosing motility, showing that sperm with higher rolling frequency and velocity are more motile and progressive, potentially having greater chance of success in ART. Furthermore, our approach enabled the effective separation of heterogeneous sperm samples into highly and low motile subpopulations. By combining the effects of viscosity and applied flow, we proposed a selection procedure based on different motion dynamics, demonstrating that only 3D motion-capable sperm (i.e. rolling) can perform rheotaxis and successfully advance through the fluid, while those hindered by increased viscosity due to flattened 2D trajectories (i.e. no rolling) are excluded from the sample. This illustrates what occurs

within the FRT, where only properly motile sperm can overcome its barriers while sperm with altered motion patterns are instead impeded.

Our multidimensional approach aims to deepen our understanding of male fertility, offering our findings as an additional tool to enhance ART. This presents a promising way for optimizing sperm selection and analysis, particularly considering the escalating global prevalence of male infertility. This not only enhances our comprehension of bovine sperm dynamics but also holds significant implications for refining techniques in both veterinary and human reproductive medicine. In conclusion, the proposed microfluidic selection mechanism is versatile and allows, in a cost-effective way and within a single device, the observation of several aspects of sperm motility and their physiological interactions, addressing critical aspects of fertility diagnostics and treatment strategies, for individuals facing reproductive challenges.

To further enhance the robustness and applicability of our approach, we propose a series of future experiments and analyses, primarily focusing on bovine models and extending insights to human sperm. We propose to conduct more extensive experiments to validate and refine our microfluidic selection mechanism. This includes a comprehensive analysis of sperm vitality, DNA integrity, and a detailed morphological examination, contributing to a deeper understanding of sperm health and functionality. In addition, we want to enhance the automation of our analysis to increase the throughput of the approach. This could be feasible by creating a dataset consisting of all the possible sperm motion configurations to detect them within the acquisition, going behind the intrinsic heterogeneity of sperm samples. Moreover, we also propose to experiment the effect of biocompatible and optically transparent solutions having even higher viscosity to mimic the cervical mucus more closely. Extensive experimentation with human sperm is crucial for validating and refining our approach. Both static and dynamic conditions should be further explored, and our methodology tested on a larger and more diverse set of human samples. The flagellum plays a pivotal role in the 3D motion of sperm. Future studies should focus on analyses of flagellar dynamics under varying experimental conditions, aiming to reveal intricate details of physiological processes within the FRT and providing a broader perspective on sperm selection and analysis.

Appendix A

The MATLAB routine has been developed by our research group specifically to detect the brightest spot on the head of a sperm cell and to track its movement along the brightfield acquisitions, thereby reconstructing the sperm trajectory. The routine can detect and track multiple cells within a single acquisition.

Although the analysis process is not entirely automatic in its current state, it has been standardized for practical use. Initially, the tracking parameters were fine-tuned using a sample acquisition. Subsequently, by ensuring consistency across all acquisitions, we were able to track sperm in each of them simply by employing the same set of tracking parameters established at the beginning. Here are the key parameters which were adjusted:

1. Sensitivity (S): This parameter, ranging between 0 and 1, manages the detection of the apparent head centroid (AC) coordinates, which represent the brightest point within the sperm head. A higher sensitivity value makes the MATLAB function more responsive to detecting circular objects. In this case, it was set at 0.6.

2. Maximum Linking Distance (D): This parameter defines the maximum distance within which two points in two consecutive frames are connected. We set it to approximately 9 μm, which aligns with the typical length of a bovine sperm head.

3. Gap Closing Distance ($D_{gap\text{-}closing}$): This parameter defines the maximum distance within which two points in frames not immediately consecutive (with a maximum gap of 5 frames) are linked. Like the maximum linking distance, it was set to approximately 9 μm, corresponding approximatively to the length of a bovine sperm head.

These parameters collectively facilitate robust sperm tracking and trajectory reconstruction within our experimental setup.

After trajectory reconstruction, sperm motility parameters, such as VSL, VCL and LIN were evaluated according to the mathematical definition found in [98]. The definitions are reported in the following equations:

$$VSL = d(P_1, P_N) * \frac{FR}{N-1} * \gamma \tag{6}$$

$$VCL = \left[\sum_{i=1}^{N-1} d(P_i, P_{i+1})\right] * \frac{FR}{N-1} * \gamma \tag{7}$$

$$LIN = \frac{VSL}{VCL} * 100 \tag{8}$$

Where P_i is the $i-th$ point of a trajectory of length N, $d(P,Q)$ is the Euclidean distance between point P and Q, FR is the frame rate, γ is the conversion factor from pixel to microns which in this analysis was 0.325.

6. References

[1] R. Nosrati *et al.*, "Microfluidics for sperm analysis and selection," *Nat Rev Urol*, vol. 14, no. 12, pp. 707–730, 2017, doi: 10.1038/nrurol.2017.175.

[2] M. L. Eisenberg *et al.*, "Male infertility," *Nature Reviews Disease Primers*, vol. 9, no. 1. Nature Research, Dec. 01, 2023. doi: 10.1038/s41572-023-00459-w.

[3] A. Agarwal, A. Mulgund, A. Hamada, and M. R. Chyatte, "A unique view on male infertility around the globe," *Reproductive Biology and Endocrinology*, vol. 13, no. 1, Dec. 2015, doi: 10.1186/s12958-015-0032-1.

[4] H. Jafari, K. Mirzaiinajmabadi, R. L. Roudsari, and M. Rakhshkhorshid, "The factors affecting male infertility: A systematic review," *International Journal of Reproductive BioMedicine*, vol. 19, no. 8. Research and Clinical Center for Infertitlity, pp. 681–688, Aug. 01, 2021. doi: 10.18502/ijrm.v19i8.9615.

[5] U. Mann, B. Shiff, and P. Patel, "Reasons for worldwide decline in male fertility," *Current Opinion in Urology*, vol. 30, no. 3. Lippincott Williams and Wilkins, pp. 296–301, May 01, 2020. doi: 10.1097/MOU.0000000000000745.

[6] E. Babakhanzadeh, M. Nazari, S. Ghasemifar, and A. Khodadadian, "Some of the factors involved in male infertility: A prospective review," *International Journal of General Medicine*, vol. 13. Dove Medical Press Ltd., pp. 29–41, 2020. doi: 10.2147/IJGM.S241099.

[7] A. Tsoumanis, N. Hens, and C. R. Kenyon, "Is Screening for Chlamydia and Gonorrhea in Men Who Have Sex with Men Associated with Reduction of the Prevalence of these Infections? A Systematic Review of Observational Studies," *Sexually Transmitted Diseases*, vol. 45, no. 9. Lippincott Williams and Wilkins, pp. 615–622, Sep. 01, 2018. doi: 10.1097/OLQ.0000000000000824.

[8] M. N. Mascarenhas, S. R. Flaxman, T. Boerma, S. Vanderpoel, and G. A. Stevens, "National, Regional, and Global Trends in Infertility Prevalence Since 1990: A Systematic Analysis of 277 Health Surveys," *PLoS Med*, vol. 9, no. 12, Dec. 2012, doi: 10.1371/journal.pmed.1001356.

[9] R. Nosrati, A. Driouchi, C. M. Yip, and D. Sinton, "Two-dimensional slither swimming of sperm within a micrometre of a surface," *Nat Commun*, vol. 6, no. November, pp. 1–9, 2015, doi: 10.1038/ncomms9703.

[10] S. Pesch and M. Bergmann, "Structure of mammalian spermatozoa in respect to viability, fertility and cryopreservation," *Micron*, vol. 37, no. 7, pp. 597–612, Oct. 2006, doi: 10.1016/J.MICRON.2006.02.006.

[11] A. Touré, "Importance of slc26 transmembrane anion exchangers in sperm post-testicular maturation and fertilization potential," *Frontiers in Cell and Developmental Biology*, vol. 7, no. OCT. Frontiers Media S.A., pp. 1–22, 2019. doi: 10.3389/fcell.2019.00230.

[12] J. A. Foster and G. L. Gerton, "The acrosomal matrix," in *Advances in Anatomy Embryology and Cell Biology*, vol. 220, Springer Verlag, 2016, pp. 15–33. doi: 10.1007/978-3-319-30567-7_2.

[13] D. W. Fawcett, "The Structure of the Mammalian Spermatozoon," *Int Rev Cytol*, vol. 7, no. C, pp. 195–234, Jan. 1958, doi: 10.1016/S0074-7696(08)62688-1.

[14] M. R. Leung *et al.*, "Structural specializations of the sperm tail," *Cell*, vol. 186, no. 13, pp. 2880-2896.e17, Jun. 2023, doi: 10.1016/j.cell.2023.05.026.

[15] L. Zhou *et al.*, “Structures of sperm flagellar doublet microtubules expand the genetic spectrum of male infertility,” *Cell*, vol. 186, no. 13, pp. 2897-2910.e19, Jun. 2023, doi: 10.1016/j.cell.2023.05.009.

[16] A. Gong *et al.*, “The steering gaits of sperm,” *Philosophical Transactions of the Royal Society B: Biological Sciences*, vol. 375, no. 1792. Royal Society Publishing, Feb. 17, 2020. doi: 10.1098/rstb.2019.0149.

[17] J. Elgeti, R. G. Winkler, and G. Gompper, “Physics of microswimmers - Single particle motion and collective behavior: A review,” *Reports on Progress in Physics*, vol. 78, no. 5, May 2015, doi: 10.1088/0034-4885/78/5/056601.

[18] E. Lauga and T. R. Powers, “The hydrodynamics of swimming microorganisms,” *Reports on Progress in Physics*, vol. 72, no. 9, 2009, doi: 10.1088/0034-4885/72/9/096601.

[19] E. M. Purcell, “Life at low Reynolds number,” *Am J Phys*, vol. 45, no. 1, pp. 3–11, Jan. 1977, doi: 10.1119/1.10903.

[20] T.-W. Su, L. Xue, and A. Ozcan, “High-throughput lensfree 3D tracking of human sperms reveals rare statistics of helical trajectories,” *PNAS*, vol. 109, no. 40, pp. 16018–16022, 2012, doi: 10.1073/pnas.1212506109/-/DCSupplemental.

[21] M. U. Daloglu and A. Ozcan, “Computational imaging of sperm locomotion,” *Biol Reprod*, vol. 97, no. 2, pp. 182–188, 2017, doi: 10.1093/biolre/iox086.

[22] E. Lauga and T. R. Powers, “The hydrodynamics of swimming microorganisms,” *Reports on Progress in Physics*, vol. 72, no. 9, 2009, doi: 10.1088/0034-4885/72/9/096601.

[23] H. C. Berg, *Random walks in biology (Howard C Berg) (z-lib.org)*. Princeton University Press, 1993.

[24] A. Gong *et al.*, “Reconstruction of the three-dimensional beat pattern underlying swimming behaviors of sperm,” *European Physical Journal E*, vol. 44, no. 7, Jul. 2021, doi: 10.1140/epje/s10189-021-00076-z.

[25] S. Ishijima, M. S. Hamaguchi, M. Naruse, S. A. Ishijima, and Y. Hamaguchi, “Rotational movement of a spermatozoon around its long axis,” 1992. doi: 10.1242/jeb.163.1.15.

[26] G. Corkidi *et al.*, “Human sperm rotates with a conserved direction during free-swimming in 3D,” *J Cell Sci*, Nov. 2023, doi: 10.1242/jcs.261306.

[27] A. Dean Drake, “Observations on Bull Sperm Rotation,” *Biol Reprod*, vol. 10, pp. 78–84, 1974, doi: https://doi.org/10.1095/biolreprod10.1.78.

[28] M. R. Miller *et al.*, “Asymmetrically Positioned Flagellar Control Units Regulate Human Sperm Rotation,” *Cell Rep*, vol. 24, no. 10, pp. 2606–2613, Sep. 2018, doi: 10.1016/j.celrep.2018.08.016.

[29] Z. Zhong *et al.*, “Chirality and frequency measurement of longitudinal rolling of human sperm using optical trap,” *Front Bioeng Biotechnol*, vol. 10, Dec. 2022, doi: 10.3389/fbioe.2022.1028857.

[30] E. T. Y. Leung *et al.*, “Simulating nature in sperm selection for assisted reproduction,” *Nat Rev Urol*, vol. 19, no. 1, pp. 16–36, 2022, doi: 10.1038/s41585-021-00530-9.

[31] S. S. Suarez and A. A. Pacey, “Sperm transport in the female reproductive tract,” *Human Reproduction Update*, vol. 12, no. 1. pp. 23–37, Jan. 2006. doi: 10.1093/humupd/dmi047.

[32] J. P. Rickard, K. R. Pool, X. Druart, and S. P. de Graaf, “The fate of spermatozoa in the female reproductive tract: A comparative review,” *Theriogenology*, vol. 137. Elsevier Inc., pp. 104–112, Oct. 01, 2019. doi: 10.1016/j.theriogenology.2019.05.044.

[33] A. K. Mishra, A. Kumar, D. K. Swain, S. Yadav, and R. Nigam, “Insights into pH regulatory mechanisms in mediating spermatozoa functions,” *Vet World*, vol. 11, no. 6, pp. 852–858, 2018, doi: 10.14202/vetworld.2018.852-858.

[34] Acott TS and Carr DW, “Inhibition of Bovine Spermatozoa by Caudal Epididymal Fluid: II. Interaction of pH and a Quiescence Factor,” *Biology of Reproduction* , vol. 30, no. 4, pp. 926–935, 1984, doi: https://doi.org/10.1095/biolreprod30.4.926.

[35] D. P. Wolf, L. Blasco, M. A. Khan, and M. Litt, “Human Cervical Mucus. I. Rheologic Characteristics,” *Fertil Steril*, vol. 28, no. 1, pp. 41–46, Jan. 1977, doi: 10.1016/S0015-0282(16)42315-0.

[36] D. P. Wolf, L. Blasco, M. A. Khan, and M. Litt, “Human Cervical Mucus. II. Changes in Viscoelasticity During the Ovulatory Menstrual Cycle,” *Fertil Steril*, vol. 28, no. 1, pp. 47–52, Jan. 1977, doi: 10.1016/S0015-0282(16)42316-2.

[37] D. P. Wolf, J. Sokoloski, M. A. Khan, and M. Litt, “Human Cervical Mucus. III. Isolation and Characterization of Rheologically Active Mucin,” *Fertil Steril*, vol. 28, no. 1, pp. 53–58, Jan. 1977, doi: 10.1016/S0015-0282(16)42317-4.

[38] S. K. Lai *et al.*, “Rapid transport of large polymeric nanoparticles in fresh undiluted human mucus,” 2007. [Online]. Available: www.pnas.orgcgidoi10.1073pnas.0608611104

[39] S. X. Yu *et al.*, “Cervix chip mimicking cervical microenvironment for quantifying sperm locomotion,” *Biosens Bioelectron*, vol. 204, no. January, 2022, doi: 10.1016/j.bios.2022.114040.

[40] D. J. Smith, E. A. Gaffney, H. Gadelha, N. Kapur, and J. C. Kirkman-Brown, “Bend propagation in the flagella of migrating human sperm, and Its modulation by viscosity,” *Cell Motil Cytoskeleton*, vol. 66, no. 4, pp. 220–236, Apr. 2009, doi: 10.1002/cm.20345.

[41] C. K. Tung *et al.*, “Fluid viscoelasticity promotes collective swimming of sperm,” *Sci Rep*, vol. 7, no. 1, pp. 1–9, 2017, doi: 10.1038/s41598-017-03341-4.

[42] T. Hyakutake, H. Suzuki, and S. Yamamoto, “Effect of viscosity on motion characteristics of bovine sperm,” *Journal of Aero Aqua Bio-mechanisms*, vol. 4, no. 1, pp. 63–70, 2015, doi: 10.5226/jabmech.4.63.

[43] T. Hyakutake, R. Orihara, and Y. Mezaki, “Experimental study on the effect of a surrounding fluid on bovine sperm motility in three dimensions,” *Journal of Biomechanical Science and Engineering*, vol. 12, no. 1, 2017, doi: 10.1299/jbse.16-00580.

[44] S. Phuyal, S. S. Suarez, and C. K. Tung, “Biological benefits of collective swimming of sperm in a viscoelastic fluid,” *Front Cell Dev Biol*, vol. 10, Sep. 2022, doi: 10.3389/fcell.2022.961623.

[45] T. Hyakutake, K. Sato, and K. Sugita, “Study of bovine sperm motility in shear-thinning viscoelastic fluids,” *J Biomech*, vol. 88, pp. 130–137, 2019, doi: 10.1016/j.jbiomech.2019.03.035.

[46] C. K. Tung *et al.*, “Microgrooves and fluid flows provide preferential passageways for sperm over pathogen Tritrichomonas foetus,” *Proc Natl Acad Sci U S A*, vol. 112, no. 17, pp. 5431–5436, 2015, doi: 10.1073/pnas.1500541112.

[47] M. Fukuda and K. Fukuda, “Uterine endometrial cavity movement and cervical mucus,” 1994.

[48] G. Kunz, D. Beil, H. Deininger, L. Wudt, and G. Leyendecker, “The dynamics of rapid sperm transport through the female genital tract: evidence from vaginal sonography of uterine peristalsis and hysterosalpingoscintigraphy,” *Human Reproduction*, vol. 11, no. 3, pp. 627–632, 1996, doi: 10.1093/humrep/11.3.627.

[49] N. Ahmadkhani, M. Hosseini, M. Saadatmand, and A. Abbaspourrad, “The influence of the female reproductive tract and sperm features on the design of microfluidic sperm-sorting devices,” *J Assist Reprod Genet*, vol. 39, no. 1, pp. 19–36, 2022, doi: 10.1007/s10815-021-02377-w.

[50] M. R. Raveshi, M. S. Abdul Halim, S. N. Agnihotri, M. K. O’Bryan, A. Neild, and R. Nosrati, “Curvature in the reproductive tract alters sperm–surface interactions,” *Nat Commun*, vol. 12, no. 1, 2021, doi: 10.1038/s41467-021-23773-x.

[51] G. Munroe, M. Campbell, Z. Munroe, and M. Hanks, “Female reproductive tract,” in *Equine Clinical Medicine, Surgery and Reproduction*, CRC Press, 2011, pp. 242–325. doi: 10.1016/b978-0-12-811837-5.00019-8.

[52] M. Khodamoradi, S. R. Tafti, S. A. M. Shaegh, B. Aflatoonian, M. Azimzadeh, and P. Khashayar, “Recent microfluidic innovations for sperm sorting,” *Chemosensors*, vol. 9, no. 6, pp. 1–18, 2021, doi: 10.3390/chemosensors9060126.

[53] K. Miki and D. E. Clapham, “Rheotaxis guides mammalian sperm,” *Current Biology*, vol. 23, no. 6, pp. 443–452, 2013, doi: 10.1016/j.cub.2013.02.007.

[54] M. Kumar and A. M. Ardekani, “Effect of external shear flow on sperm motility,” *Soft Matter*, vol. 15, no. 31, pp. 6269–6277, 2019, doi: 10.1039/c9sm00717b.

[55] M. Zaferani, S. H. Cheong, and A. Abbaspourrad, “Rheotaxis-based separation of sperm with progressive motility using a microfluidic corral system,” *Proc Natl Acad Sci U S A*, vol. 115, no. 33, pp. 8272–8277, Aug. 2018, doi: 10.1073/pnas.1800819115.

[56] T. Omori and T. Ishikawa, “Upward swimming of a sperm cell in shear flow,” *Phys Rev E*, vol. 93, no. 3, pp. 1–9, 2016, doi: 10.1103/PhysRevE.93.032402.

[57] K. Rappa, J. Samargia, M. Sher, J. S. Pino, H. F. Rodriguez, and W. Asghar, “Quantitative analysis of sperm rheotaxis using a microfluidic device,” *Microfluid Nanofluidics*, vol. 22, no. 9, Sep. 2018, doi: 10.1007/s10404-018-2117-6.

[58] T. M. El-Sherry, M. Elsayed, H. K. Abdelhafez, and M. Abdelgawad, “Characterization of rheotaxis of bull sperm using microfluidics,” *Integrative Biology (United Kingdom)*, vol. 6, no. 12, pp. 1111–1121, 2014, doi: 10.1039/c4ib00196f.

[59] S. Kölle, “Sperm-oviduct interactions: Key factors for sperm survival and maintenance of sperm fertilizing capacity,” *Andrology*, vol. 10, no. 5, pp. 837–843, 2022, doi: 10.1111/andr.13179.

[60] L. C. P. Molina, G. M. Luque, P. A. Balestrini, C. I. Marín-Briggiler, A. Romarowski, and M. G. Buffone, “Molecular basis of human sperm capacitation,” *Front Cell Dev Biol*, vol. 6, no. July, pp. 1–23, 2018, doi: 10.3389/fcell.2018.00072.

[61] Z. Zhang *et al.*, “Human sperm rheotaxis: A passive physical process,” *Sci Rep*, vol. 6, pp. 1–8, 2016, doi: 10.1038/srep23553.

[62] M. Zaferani, F. Javi, A. Mokhtare, P. Li, and A. Abbaspourrad, “Rolling controls sperm navigation in response to the dynamic rheological properties of the environment,” *Elife*, vol. 10, 2021, doi: 10.7554/ELIFE.68693.

[63] P. Denissenko, V. Kantsler, D. J. Smith, and J. Kirkman-Brown, “Human spermatozoa migration in microchannels reveals boundary-following navigation,” *Proc Natl Acad Sci U S A*, vol. 109, no. 21, pp. 8007–8010, 2012, doi: 10.1073/pnas.1202934109.

[64] J. Elgeti, U. B. Kaupp, and G. Gompper, “Hydrodynamics of sperm cells near surfaces,” *Biophys J*, vol. 99, no. 4, pp. 1018–1026, Aug. 2010, doi: 10.1016/j.bpj.2010.05.015.

[65] I. R. Sarbandi, A. Lesani, M. Moghimi Zand, and R. Nosrati, “Rheotaxis-based sperm separation using a biomimicry microfluidic device,” *Sci Rep*, vol. 11, no. 1, pp. 1–8, 2021, doi: 10.1038/s41598-021-97602-y.

[66] C. Schiffer *et al.*, “ Rotational motion and rheotaxis of human sperm do not require functional CatSper channels and transmembrane Ca 2+ signaling ,” *EMBO J*, vol. 39, no. 4, Feb. 2020, doi: 10.15252/embj.2019102363.

[67] R. Rikmenspoel;, G. V. Herpens, and P. Eijrhout, “Cinematographic Observations of the Movements of Bull Sperm Cellst,” *Phys Med Biol*, vol. 5, no. 167, 1960, doi: 10.1088/0031-9155/5/2/306.

[68] R. Rikmenspoel, “The tail movement of bull spermatozoa. Observations and model calculation,” *Biophys J.*, vol. 5, no. 4, pp. 365–92, 1965, doi: 10.1016/S0006-3495(65)86723-6.

[69] S. Baskaran, R. Finelli, A. Agarwal, and R. Henkel, “Diagnostic value of routine semen analysis in clinical andrology,” *Andrologia*, vol. 53, no. 2. Blackwell Publishing Ltd, Mar. 01, 2021. doi: 10.1111/and.13614.

[70] World Health Organization, *WHO laboratory manual for the examination and processing of human semen Sixth Edition*, vol. Edition, V. 2021. [Online]. Available: http://whqlibdoc.who.int/publications/2010/9789241547789_eng.pdf

[71] R. Finelli, K. Leisegang, S. Tumallapalli, R. Henkel, and A. Agarwal, “The validity and reliability of computer-aided semen analyzers in performing semen analysis: a systematic review,” *Translational Andrology and Urology*, vol. 10, no. 7. AME Publishing Company, pp. 3069–3079, Jul. 01, 2021. doi: 10.21037/tau-21-276.

[72] L. Maree, “Standard Semen Analysis: Computer-Assisted Semen Analysis,” in *Manual of Sperm Function Testing in Human Assisted Reproduction*, A. Agarwal, R. Henke, and A. Majzoub, Eds., Cambridge University Press, 2021, pp. 11–22. doi: 10.1017/9781108878715.

[73] A. B. Harchegani, H. Rahmani, E. Tahmasbpour, and A. Shahriary, “Hyperviscous Semen Causes Poor Sperm Quality and Male Infertility through Induction of Oxidative Stress,” *Current Urology*, vol. 13, no. 1. S. Karger AG, pp. 1–6, Sep. 01, 2019. doi: 10.1159/000499302.

[74] J. Elia *et al.*, “Human semen hyperviscosity: Prevalence, pathogenesis and therapeutic aspects,” *Asian J Androl*, vol. 11, no. 5, pp. 609–615, 2009, doi: 10.1038/aja.2009.46.

[75] A. Ferlin *et al.*, “Sperm Count and Hypogonadism as Markers of General Male Health,” *Eur Urol Focus*, vol. 7, no. 1, pp. 205–213, Jan. 2021, doi: 10.1016/j.euf.2019.08.001.

[76] E. Zuvela and P. Matson, “Performance of four chambers to measure sperm concentration: results from an external quality assurance programme,” *Reprod Biomed Online*, vol. 41, no. 4, pp. 671–678, Oct. 2020, doi: 10.1016/j.rbmo.2020.07.008.

[77] P. JOUANNET, B. DUCOT, D. FENEUX, and A. SPIRA, “Male factors and the likelihood of pregnancy in infertile couples. I. Study of sperm characteristics,” *Int J Androl*, vol. 11, no. 5, pp. 379–394, 1988, doi: 10.1111/j.1365-2605.1988.tb01011.x.

[78] M. J. Zinaman, C. C. Brown, S. G. Selevan, and E. D. Clegg, “Semen quality and human fertility: A prospective study with healthy couples,” *J Androl*, vol. 21, no. 1, pp. 145–153, Jan. 2000, doi: 10.1002/j.1939-4640.2000.tb03284.x.

[79] F. Boitrelle *et al.*, “The Sixth Edition of the WHO Manual for Human Semen Analysis: A Critical Review and SWOT Analysis,” *Life*, vol. 11, no. 12. MDPI, Dec. 01, 2021. doi: 10.3390/life11121368.

[80] C. Douglas, N. Parekh, L. G. Kahn, R. Henkel, and A. Agarwal, “A novel approach to improving the reliability of manual semen analysis: A paradigm shift in the workup of infertile men,” *World Journal of Men’s Health*, vol. 37, 2019, doi: 10.5534/WJMH.190088.

[81] E. Filimberti *et al.*, “High variability in results of semen analysis in andrology laboratories in Tuscany (Italy): the experience of an external quality control (EQC) programme.,” *Andrology*, vol. 1, no. 3, pp. 401–407, 2013, doi: 10.1111/j.2047-2927.2012.00042.x.

[82] C. Wang and R. S. Swerdloff, “Limitations of semen analysis as a test of male fertility and anticipated needs from newer tests,” *Fertility and Sterility*, vol. 102, no. 6. Elsevier Inc., pp. 1502–1507, Dec. 01, 2014. doi: 10.1016/j.fertnstert.2014.10.021.

[83] G. Van Der Horst, L. Maree, and S. S. Du Plessis, “Current perspectives of CASA applications in diverse mammalian spermatozoa,” *Reprod Fertil Dev*, vol. 30, no. 6, pp. 875–888, 2018, doi: 10.1071/RD17468.

[84] A. Agarwal *et al.*, “Standardized Laboratory Procedures, Quality Control and Quality Assurance Are Key Requirements for Accurate Semen Analysis in the Evaluation of Infertile Male,” *World Journal of Men’s Health*, vol. 40, no. 1. Korean Society for Sexual Medicine and Andrology, pp. 52–65, Jan. 01, 2022. doi: 10.5534/wjmh.210022.

[85] B. Schubert, M. Badiou, and A. Force, “Computer-aided sperm analysis, the new key player in routine sperm assessment,” *Andrologia*, vol. 51, no. 10, Nov. 2019, doi: 10.1111/and.13417.

[86] ESHRE Andrology Special Interest Group, “Guidelines on the application of CASA technology in the analysis of spermatozoa ESHRE Andrology Special Interest Group*,” *Human Reproduction*, vol. 13, no. 1, pp. 142–145, 1998, doi: https://doi.org/10.1093/humrep/13.1.142.

[87] D. Mortimer, RJ. Aitken, ST. Mortimer, and AA. Pacey, “Workshop Report: Clinical CASA-the Quest for Consensus,” *Reproduction, Fertility and Development* , vol. 7, no. 4, pp. 951–959, 1995, doi: https://doi.org/10.1071/RD9950951.

[88] D. Mortimer, C. Serres, S. T. Mortimer, and P. Jouannet, “Influence of Image Sampling Frequency on the Perceived Movement Characteristics of Progressively Motile Human Spermatozoa,” 1988.

[89] S. T. Mortimer, “A critical review of the physiological importance and analysis of sperm movement in mammals*,” 1997. doi: https://doi.org/10.1093/humupd/3.5.403.

[90] P. Vogiatzi *et al.*, “Male Age and Progressive Sperm Motility Are Critical Factors Affecting Embryological and Clinical Outcomes in Oocyte Donor ICSI Cycles,” *Reproductive Sciences*, vol. 29, no. 3, pp. 883–895, Mar. 2022, doi: 10.1007/s43032-021-00801-1.

[91] M. T. Gallagher, D. J. Smith, and J. C. Kirkman-Brown, “CASA: Tracking the past and plotting the future,” *Reproduction, Fertility and Development*, vol. 30, no. 6. CSIRO, pp. 867–874, 2018. doi: 10.1071/RD17420.

[92] A. Valverde, V. Barquero, and C. Soler, “The application of computer-assisted semen analysis (CASA) technology to optimise semen evaluation. A review,” *J Anim Feed Sci*, vol. 29, no. 3, pp. 189–198, Sep. 2020, doi: 10.22358/JAFS/127691/2020.

[93] J. Yániz *et al.*, “Expanding the limits of computer-assisted sperm analysis through the development of open software,” *Biology (Basel)*, vol. 9, no. 8, pp. 1–16, Aug. 2020, doi: 10.3390/biology9080207.

[94] D. Bompart *et al.*, “Combined effects of type and depth of counting chamber, and rate of image frame capture, on bull sperm motility and kinematics,” *Anim Reprod Sci*, vol. 209, Oct. 2019, doi: 10.1016/j.anireprosci.2019.106169.

[95] C. Castellini, A. Dal Bosco, S. Ruggeri, and G. Collodel, “What is the best frame rate for evaluation of sperm motility in different species by computer-assisted sperm analysis?,” *Fertil Steril*, vol. 96, no. 1, pp. 24–27, Jul. 2011, doi: 10.1016/j.fertnstert.2011.04.096.

[96] C. Bai, Z. Jiang, J. Zhao, S. Wu, and Q. Zhang, “3D dynamic observation of human sperm by parallel phase-shifting digital holographic microscopy based on pixelated polarization,” *APL Photonics*, vol. 8, no. 7, Jul. 2023, doi: 10.1063/5.0150582.

[97] F. Buchelly Imbachí *et al.*, “Objective evaluation of ram and buck sperm motility by using a novel sperm tracker software,” 2018, doi: 10.1530/REP.

[98] C. Alquézar-Baeta *et al.*, “OpenCASA: A new open-source and scalable tool for sperm quality analysis,” *PLoS Comput Biol*, vol. 15, no. 1, pp. 1–18, 2019, doi: 10.1371/journal.pcbi.1006691.

[99] J. G. Wilson-Leedy and R. L. Ingermann, “Development of a novel CASA system based on open source software for characterization of zebrafish sperm motility parameters,” *Theriogenology*, vol. 67, no. 3, pp. 661–672, Feb. 2007, doi: 10.1016/j.theriogenology.2006.10.003.

[100] S. G. Goodson *et al.*, “CASAnova: A multiclass support vector machine model for the classification of human sperm motility patterns,” *Biol Reprod*, vol. 97, no. 5, pp. 698–708, 2017, doi: 10.1093/biolre/iox120.

[101] M. T. Gallagher, G. Cupples, E. H. Ooi, J. C. Kirkman-Brown, and D. J. Smith, “Rapid sperm capture: High-throughput flagellar waveform analysis,” *Human Reproduction*, vol. 34, no. 7, pp. 1173–1185, 2019, doi: 10.1093/humrep/dez056.

[102] F. Zegers-Hochschild *et al.*, “The international glossary on infertility and fertility care, 2017,” *Human Reproduction*, vol. 32, no. 9, pp. 1786–1801, Sep. 2017, doi: 10.1093/humrep/dex234.

[103] J. Y. J. Huang and Z. Rosenwaks, “Assisted Reproductive Techniques,” in *Human Fertility Methods and Protocols*, Z. Rosenwaks and P. M. Wassarman, Eds., New York: Springer, 2014, pp. 171–231. doi: 10.1007/978-1-4939-0659-8.

[104] R. R. Henkel and W.-B. Schill, “Sperm preparation for ART,” 2003. [Online]. Available: http://www.rbej.com/content/1/1/108http://www.rbej.com/content/1/1/108

[105] A. Agarwal, R. K. Sharma, and T. Beydola, “Sperm Preparation and Selection Techniques,” in *Medical & Surgical Management of Male Infertility*, A. Agarwal, B. R. Rizk, N. Aziz, and S. Jr Edmund, Eds., Jaypee Brothers Medical Publishers, 2014, pp. 244–251. doi: 10.5005/jp/books/11840_29.

[106] S. C. Esteves, M. Roque, G. Bedoschi, T. Haahr, and P. Humaidan, “Intracytoplasmic sperm injection for male infertility and consequences for offspring,” *Nature Reviews Urology*, vol. 15, no. 9. Nature Publishing Group, pp. 535–562, Sep. 01, 2018. doi: 10.1038/s41585-018-0051-8.

[107] R. J. Aitken and G. N. De Iuliis, “Origins and consequences of DNA damage in male germ cells,” *Reproductive BioMedicine Online*, vol. 14, no. 6. Reproductive Healthcare Ltd, pp. 727–733, 2007. doi: 10.1016/S1472-6483(10)60676-1.

[108] S. Sharma, M. A. Kabir, and W. Asghar, “Selection of healthy sperm based on positive rheotaxis using a microfluidic device,” *Analyst*, vol. 147, no. 8, pp. 1589–1597, 2022, doi: 10.1039/d1an02311j.

[109] T. Chinnasamy *et al.*, “Guidance and Self-Sorting of Active Swimmers: 3D Periodic Arrays Increase Persistence Length of Human Sperm Selecting for the Fittest,” *Advanced Science*, vol. 5, no. 2, Feb. 2018, doi: 10.1002/advs.201700531.

[110] M. Lee *et al.*, “Viscous cervical environment-on-a-chip for selecting high-quality sperm from human semen,” *Biomedicines*, vol. 9, no. 10, Oct. 2021, doi: 10.3390/biomedicines9101439.

[111] W. Asghar *et al.*, “Selection of Functional Human Sperm with Higher DNA Integrity and Fewer Reactive Oxygen Species,” *Adv Healthc Mater*, vol. 3, no. 10, pp. 1671–1679, Oct. 2014, doi: 10.1002/adhm.201400058.

[112] A. Ataei, A. W. C. Lau, and W. Asghar, “A microfluidic sperm-sorting device based on rheotaxis effect,” *Microfluid Nanofluidics*, vol. 25, no. 6, pp. 1–10, 2021, doi: 10.1007/s10404-021-02453-8.

[113] J. Huang, H. Chen, N. Li, and Y. Zhao, “Emerging microfluidic technologies for sperm sorting,” *Engineered Regeneration*, vol. 4, no. 2. KeAi Communications Co., pp. 161–169, Jun. 01, 2023. doi: 10.1016/j.engreg.2023.02.001.

[114] C. K. Tung, F. Ardon, A. G. Fiore, S. S. Suarez, and M. Wu, “Cooperative roles of biological flow and surface topography in guiding sperm migration revealed by a microfluidic model,” *Lab Chip*, vol. 14, no. 7, pp. 1348–1356, 2014, doi: 10.1039/c3lc51297e.

[115] M. Yaghoobi, M. Azizi, A. Mokhtare, F. Javi, and A. Abbaspourrad, “Rheotaxis quality index: a new parameter that reveals male mammalian in vivo fertility and low sperm DNA fragmentation,” *Lab Chip*, vol. 22, no. 8, pp. 1486–1497, 2022, doi: 10.1039/d2lc00150k.

[116] B. Panigrahi and C. Y. Chen, “Microfluidic retention of progressively motile zebrafish sperms,” *Lab Chip*, vol. 19, no. 24, pp. 4033–4042, 2019, doi: 10.1039/c9lc00534j.

[117] M. M. Quinn *et al.*, “Microfluidic sorting selects sperm for clinical use with reduced DNA damage compared to density gradient centrifugation with swim-up in split semen samples,” *Human Reproduction*, vol. 33, no. 8, pp. 1388–1393, Aug. 2018, doi: 10.1093/humrep/dey239.

[118] G. Dardikman-Yoffe, S. K. Mirsky, I. Barnea, and N. T. Shaked, “High-resolution 4-D acquisition of freely swimming human sperm cells without staining,” *Sci Adv*, vol. 6, no. 15, 2020, doi: 10.1126/sciadv.aay7619.

[119] R. Rikmenspoel and G. Van Herpen, “Photoelectric and Cinematographic Measurements of the Motility of Bull Sperm Cells,” *Phys Med Biol*, vol. 2, no. 54, 1957, doi: 10.1088/0031-9155/2/1/306.

[120] R. Nosrati, “Lab on a chip devices for fertility: from proof-of-concept to clinical impact,” *Lab Chip*, vol. 22, no. 9, pp. 1680–1689, 2022, doi: 10.1039/d1lc01144h.

[121] V. Kantsler, J. Dunkel, M. Blayney, and R. E. Goldstein, “Rheotaxis facilitates upstream navigation of mammalian sperm cells,” *Elife*, vol. 3, pp. 1–12, 2014, doi: 10.7554/elife.02403.

[122] B. Soumyabrata *et al.*, “The revolution of PDMS microfluidics in cellular biology.” Critical Reviews in Biotechnology, 2022.

[123] B. De Wagenaar, J. T. W. Berendsen, J. G. Bomer, W. Olthuis, A. Van Den Berg, and L. I. Segerink, “Microfluidic single sperm entrapment and analysis,” *Lab Chip*, vol. 15, no. 5, pp. 1294–1301, Mar. 2015, doi: 10.1039/c4lc01425a.

[124] S. Lee and N. D. Spencer, “Adsorption properties of poly(L-lysine)-graft-poly(ethylene glycol) (PLL-g-PEG) at a hydrophobic interface: Influence of tribological stress, pH, salt concentration, and polymer molecular weight,” *Langmuir*, vol. 24, no. 17, pp. 9479–9488, Sep. 2008, doi: 10.1021/la801200h.

[125] S. Lee and J. Vörös, “An aqueous-based surface modification of poly(dimethylsiloxane) with poly(ethylene glycol) to prevent biofouling,” *Langmuir*, vol. 21, no. 25, pp. 11957–11962, Dec. 2005, doi: 10.1021/la051932p.

[126] S. Kölle, “Sperm-oviduct interactions: Key factors for sperm survival and maintenance of sperm fertilizing capacity,” *Andrology*, vol. 10, no. 5, pp. 837–843, 2022, doi: 10.1111/andr.13179.

[127] M. Sabour, A. Agha-Rahimi, M. Dehghani Ashkezari, S. M. Seifati, F. Anbari, and A. Nabi, “Prolonged exposure of human spermatozoa in polyvinylpyrrolidone has detrimental effects on sperm biological characteristics,” *Andrologia*, vol. 54, no. 6, Jul. 2022, doi: 10.1111/and.14402.

[128] Y. Kato and Y. Nagao, “Effect of polyvinylpyrrolidone on sperm function and early embryonic development following intracytoplasmic sperm injection in human assisted reproduction,” *Reproductive Medicine and Biology*, vol. 11, no. 4. John Wiley and Sons Ltd, pp. 165–176, 2012. doi: 10.1007/s12522-012-0126-9.

[129] T. Irez, P. Ocal, O. Guralp, S. Kaleli, F. Ocer, and S. Sahmay, “Sperm selection based on motility in polyvinylpyrrolidone is associated with successful pregnancy and embryo development,” *Andrologia*, vol. 45, no. 4, pp. 240–247, Aug. 2013, doi: 10.1111/j.1439-0272.2012.01337.x.

[130] P. Sunanda, B. Panda, C. Dash, R. N. Padhy, and P. Routray, “An illustration of human sperm morphology and their functional ability among different group of subfertile males,” *Andrology*, vol. 6, no. 5, pp. 680–689, Sep. 2018, doi: 10.1111/andr.12500.

[131] Y. Hirano *et al.*, “Accuracy of sperm velocity assessment using the Sperm Quality Analyzer V,” 2003.

List of figures